UNIVERSITA' DI PADOVA  FACOLTA' DI INGEGNERIA

Dipartimento di Ingegneria dell'Informazione

Scuola di Dottorato di Ricerca in Ingegneria dell'Informazione
Indirizzo: Bioingegneria

CICLO XXII

PROGETTAZIONE, REALIZZAZIONE E VALUTAZIONE CLINICA DI UNO STRUMENTO AD OTTICA ADATTIVA PER L'ANALISI AUTOMATICA DELLA RETINA

Direttore della Scuola: Ch.mo Prof. Matteo Bertocco

Supervisore: Ch.ma Prof. Maria Pia Saccomani

Dottorando: Enea Poletti

Contents

Contents ..... **i**

List of Figures ..... **vi**

List of Tables ..... **xii**

Sommario ..... **xiv**

Summary ..... **xvii**

Chapter 1 Introduction **20**

1.1 Aims and Objectives 21

1.2 Outline 22

Chapter 2 Fundus Imaging and its Findings **23**

2.1 Fundus Oculi Examination 23
2.1.1 Fundus Oculi Appearance 24

2.2 Main Vascular Abnormalities 25
2.2.1 Tortuosity 25
2.2.2 Generalized Arteriolar Narrowing 25
2.2.3 Focal Arteriolar Narrowing 26
2.2.4 Bifurcation Abnormalities 26
2.2.5 Crossing Abnormalities 27

2.3 Major Non-Vascular Findings 28
2.3.1 Microaneurysms and Red Dots 28
2.3.2 Hemorrhages 28
2.3.3 Hard Exudates 29
2.3.4 Cotton Wool Spots 30
2.3.5 Drusen 30

2.4 Hypertensive Retinopathy Grading 31

2.5 Diabetic Retinopathy 32

Chapter 3 Image Acquisition Protocols and Clinical Evaluation **34**

3.1 Diabetic Retinopathy 34
3.1.1 ETDRS Protocol 35

3.1.2 EURODIAB Protocol 35
3.1.3 Joslin Clinic Protocol 37
3.1.4 Single Field Monochromatic 38
3.1.5 Fields Protocol 38
3.1.6 Single-Field Colour Protocol 39

3.2 Hypertensive Retinopathy 39
3.2.1 ARIC Protocol 39

3.3 Protocol for Hypertensive Retinopathy 40

3.4 Conclusions 40

Chapter 4 The Adaptive Optics System: Compensation of Aberrations 43

4.1 Software Analysis for the Compensation of the Primary Aberration ... 43
4.1.1 The Zernike Polynomials 44
4.1.2 Aberration Hierarchy 45
4.1.3 Aberration Correction 46

4.2 Simulation Setup 51

4.3 Results 52

4.4 Conclusions 57

Chapter 5 The Adaptive Optic System: Fundus Camera Prototype59

5.1 Introduction 59

5.2 Software Concepts and Aberration Correction Strategy 62

5.3 Experimental Setup for the Test of the AO System 65

5.4 Wavefront Aberration Correction Results 66

5.5 Experimental Setup for the Retinal Fundus Acquisition 70

5.6 Artificial Retinal Fundus Acquisition Results 72

5.7 Conclusions 73

Chapter 6 Collected Datasets 75

6.1 The DRIVE Dataset 75

6.2 The STARE Dataset 76

6.3 University of Wisconsin Dataset 76

6.4 Moorfields Eye Hospital Dataset 77

6.5 DB60, Yet Another Homemade Dataset 77
6.5.1 Image Collection 77

Chapter 7 Vessel Tracking 80

7.1 Brief Overview of Available Methods 81
7.1.1 Local Vascular Segmentation 81
7.1.2 Matched Filters 82
7.1.3 Morphological processing and curvature estimation 83
7.1.4 Pixel-based classification 83
7.1.5 Vessel Tracking 84

7.2 Methods 85
7.2.1 Preprocessing 86
7.2.2 Seed-Finding Procedure 90
7.2.3 Multi-directional Shortest Path Search Idea 95
7.2.4 The Algorithm 95
7.2.5 Post-Processing 101

7.3 False Vessel Detection 101

7.4 Results 105

7.5 Conclusion 110

Chapter 8 Vessel Diameter Estimation 112

8.1 Introduction 113

8.2 Materials 114

8.3 Methods 114
8.3.1 Preprocessing and Profile Extraction 115
8.3.2 Edge Point Detection 116
8.3.3 Adaptive Correction 119
8.3.4 Border Refinement 120

8.4 Results 122
8.4.1 Caliber Correlation 122
8.4.2 Mask Comparison 123

8.5 Conclusions 127

Chapter 9 Vessel Tortuosity 129

9.1 Tortuosity Properties 129
9.1.1 Affine Transformations 129
9.1.2 Composition 130
9.1.3 Modulation 131

9.2 Available Tortuosity Measures 131
9.2.1 Arc Length over Length Ratio 131
9.2.2 Measure Involving Curvature 132
9.2.3 Mean Direction Angle Change 133

9.3 Available Data 133

9.4 Vessel Representation 134

9.5 Tortuosity Calculation 134
9.5.1 Tortuosity: First Proposal 136
9.5.2 Tortuosity: Second Proposal 136

9.6 Results on Manually Tracked Vessels 137

9.7 Results on Automatically Tracked Vessels 138

Chapter 10 Clinical Usability of the Proposed Software for the AVR Estimation 142

10.1 Introduction 142

10.2 Methods 143
10.2.1 Artery/Vein Discrimination 144
10.2.2 AVR Estimation 145

10.3 Results 145
10.3.1 Limited Intervention Setup 146
10.3.2 Full Intervention Setup 149

10.4 Conclusion 151

Chapter 11 Conclusions 153

11.1 Achievement of the Objectives 153
11.1.1 AO Fundus Camera Prototyping 154
11.1.2 Retinal Vessel Network Extraction 154
11.1.3 Tools for Clinical Use 155

11.2 Final Summary 156

References **160**

List of Figures

Figure 2.1 An image of a normal fundus oculi. Papilla (a), fovea (b) and vessel networks are clearly visible 24

Figure 2.2. Normal vessel course (a) and tortuous vessels (b)..... 25

Figure 2.3. A definite focal narrowing..... 26

Figure 2.4. Gunn's sign - vein compression (a) and Salus' sign – vein deflection (b).... 27

Figure 2.5. Large microaneurysm with central reflex (a) and microaneurysm (b)..... 28

Figure 2.6. Small hemorrhage (a), barely visible hemorrhage (b), flame hemorrhage (d), large hemorrhage (d), and bright hemorrhage (e). 29

Figure 2.7. Different hard exudates..... 30

Figure 2.8. Cotton wool spots. 30

Figure 3.1 Standard ETDRS 7 fields..... 36

Figure 3.2 Joslin Vision Network Non Mydriatic Fields (black circles), and standard ETDRS 7 fields (dotted blue) 37

Figure 3.3 Non Mydriatic Monochromatic Field proposed in [16] (black circle), and standard ETDRS 7 fields (dotted blue) 38

Figure 4.1 Typical image of a point source image affected by coma. 46

Figure 4.2 Point source image affected by astigmatism at different focal plane positions. The position (b) corresponds to the so-called "circle of least confusion."..... 46

Figure 4.3 Flow chart of the proposed algorithm. Zernike coefficients related to each aberration are hierarchically and separately estimated. 47

Figure 4.4 Coma detection: the white star is c_2 and the white circle is c_1, as defined in the text. 49

Figure 4.5 Equivalent model of the simple optical system simulated for testing the aberration correction algorithm..... 51

Figure 4.6 Comparison plots of the Zernike coefficients of the fixed surface Σ_1 versus the estimated coefficient describing the surface Σ_2. In Figure 4.7(a) the plot for

the z_9 coefficient is represented, Figure 4.7(b) for the z_7 coefficient, Figure 4.7(c) for the z_8 coefficient, Figure 4.7(d) for the z_4 coefficient, Figure 4.7(e) for the z_6 coefficient, and finally Figure 4.7(f) for the z_5 coefficient. 53

Figure 4.7 Progressive aberration estimation and correction. The *xy* plot scale is the same for all the images, however the color map is different, so that each image is normalized to its maximum intensity to visualize the point source shape. (a) Original aberrated point image. Maximum intensity is 2×10^{-4}, and the function f(c) described in [30] is 0.19. (b) Aberrated point image after spherical correction. Maximum intensity is 5×10^{-4}, and the function f(c) described in [30] is 0.99. (c) Aberrated point image after coma correction. Maximum intensity is 6×10^{-4}, and the function f(c) described in [30] is 0.98. (d) Aberrated point image after defocus correction. Maximum intensity is 16×10^{-4}, and the function f(c) described in [30] is 0.90. (e) Aberrated point image after astigmatism correction. Maximum intensity is 16×10^{-4}, and the function f(c) described in [30] is 0.90. 54

Figure 4.8 Error distribution in the estimation of the Zernike coefficients. Each box has lines at the lower quartile, median, and upper quartile values. The whiskers are lines extending to the most extreme value of the data inside 1.5 times the interquartile range. Outliers are data with values beyond the ends of the whiskers, and are plotted with a single cross. 55

Figure 4.9 Error distribution in the estimation of the Zernike coefficients obtained with the direct maximization proposed in [30]. Each box has lines at the lower quartile, median, and upper quartile values. The whiskers are lines extending to the most extreme value of the data inside 1.5 times the interquartile range. Outliers are data with values beyond the ends of the whiskers, and are plotted with a single cross. 56

Figure 4.10 Number of iterations needed for the proposed algorithm to converge for each single type of aberration to be estimated. Each box has lines at the lower quartile, median, and upper quartile values. The whiskers are lines extending to the most extreme value of the data inside 1.5 times the interquartile range. Outliers are data with values beyond the ends of the whiskers, and are plotted with a single cross. 56

Figure 5.1 Block diagram of the software iterative procedure to minimize the aberrations in the optical system. 62

Figure 5.2 Schematic of the optical setup used in the tests of the AO system. 64

Figure 5.3 Picture of the optical setup used in the tests of the AO system. 64

Figure 5.4 Another picture of the optical setup used in the tests of the AO system. 65

Figure 5.5 Wavefront surfaces (obtained with the WFA) before and after the DM correction for the three considered cases. The blue dashed lines overplotted to the *z* axis represent the total w-f excursion. 67

Figure 5.6 Zernike coefficient values before and after the correction for the three considered cases. Dark points represent the aberrations before the correction; the gray ones are representative of the corrected w-f. In addition, the surface P-t-V and RMS values are reported (with the same color meaning). A gray line joins the three main aberrations (defocus, astigmatism, coma); this line, in case of ideal correction, would coincide with the dark continuous one. 68

Figure 5.7 Picture of the AO fundus camera system built for the experimental setup; yellow - illumination path; red - path for the projection of the reference pattern; green - imaging path leading to the DM; pale blue - path of the split beam sent to the aberration detector; blue - path of the split beam sent to the imaging system. 71

Figure 5.8 Example of picture acquired from the artificial fundi with the AO fundus camera prototype. 72

Figure 5.9 Another example of picture acquired from the artificial fundi with the AO fundus camera prototype 72

Figure 6.1 Standard report form (front page). 79

Figure 6.2 Standard report form (rear page) 79

Figure 7.1 (a) original image and the image results of the erosion with a disk of radii 1, 2, 3, and 4 (left column), and a subsequently dilation with the same structuring element (right column). 88

Figure 7.2 (a) An example image from the UoW dataset; (b) after opening with a disk of 4 disk radius. While the central reflexes become quite attenuated, some vessels are erroneously merged. 89

Figure 7.3 (a) regular grid of equally spaced rows and columns and (b) the corresponding seeds found. 91

Figure 7.4 (a) regular grid of equally spaced perpendicular lines, at an angle of 45° with the image coordinates; (b) the corresponding seeds found. 92

Figure 7.5 The total set of seeds found by employing both the horizontal and the inclined grids. 93

Figure 7.6 (a) seeds found in the image by analyzing the profile (b); (c) the profile resulting from the matched filtering is compared with a threshold. 94

Figure 7.7 (a) seeds found in the image by analyzing the profile (b); (c) the profile resulting from the matched filtering is compared with a threshold. 94

Figure 7.8 Example of exploration of four manually deployed seeds. On the left column the original image with the superimposed seeds and the identified paths. On the right column, the images of the matrix where for each pixel i the distance value di is stored. 99

Figure 7.9 Starting from i, the weight wi,j has the role of penalizing the exploration of the d-adjacent pixel as their distance is $\sqrt{2}$ times the distance of the 4-adjacent pixels. 99

Figure 7.10 Simple scheme that highlights the usefulness of the second derivative of the kernel G and the three obtained components. 103

Figure 7.11 (a) Detail of a vessel and (b) the $v-$ corresponding to each pixel. 103

Figure 7.12 (a) Partially false tracked vessel: the second half has been detected because of false seeds laying in the fovea; (b) image of the vessel composed by taking into consideration the longitudinal profiles of the axis (displayed to provide a straightforward view); (c) difference between the angles (in radians) of the vessel axis directions and the directions of $v-$, along the estimated axis. 104

Figure 7.13 (a) vessel axis manually drawn on the background; (b) difference between the angles (in radians) of the vessel axis directions and the directions of $v-$, along the estimated axis. 105

Figure 7.14 Example of vessel axis tracking results (DB60 dataset). 107

Figure 7.15 Example of vessel axis tracking results (DB60 dataset). 107

Figure 7.16 Example of vessel axis tracking results on an image containing pathology (DB60 dataset). 108

Figure 7.17 Example of vessel axis tracking results (DRIVE dataset). 108

Figure 7.18 Example of vessel axis tracking results (STARE dataset) 109

Figure 8.1 (a) Starting network of vessel axes; (b) estimated calibers. 112

Figure 8.2 (a) Detail of an original image with the given vessel axis (green dots), the profile pis of the current axis point Csi (yellow line), the two adjacent profiles $pi-1s$ and $pi+1s$ (blue lines); (b) mean Pis of the three profiles $pi-1s$, pis and $pi+1s$; (c) The shift invariant Gaussian filtered profile $PFis$. 116

Figure 8.3 A profile $PFis$ processed for the diameter estimation. (a) The red dot indicates the maximum peak related to the center; (b) the two dots indicates

where the slope markedly decreases by descending toward right and left valleys; (c) the rightmost point is moved to a deeper valley, whose height is comparable to the leftmost one. 117

Figure 8.4 Given a certain mono-dimensional data set, suppose to represent it as distributed on an axis. Two clusters (A and B) may be identified in proximity of the two data concentrations. The datum shown as a red marked spot belongs more to the B cluster rather than the A cluster. The value 0.2 of u indicates the degree of membership to A for such datum. 118

Figure 8.5 (a) The starting $PFis$ profile, (b) the kernel function $kECks(x)$ centered in x=0 and with $ECks = 15$ as estimated scale, and (c) the output of the matched filter, with the threshold (dashed black) chosen by using a fuzzy 2-mean clustering. The red stars represent the estimated caliber edges (c)..... 119

Figure 8.6 Border points evaluated before (top) and after (middle) diameter correction, along with the final vessel segmentation (bottom). In the middle image rhombus points were successfully corrected, while crosses were forced to the median caliber of the analyzed vessel segment. 121

Figure 8.7 Average caliber: scatter plot of manual vs. automatic estimations 122

Figure 8.8 Example of segmentation result (DB60 dataset). 124

Figure 8.9 Example of segmentation result (DRIVE dataset). 125

Figure 8.10 Example of segmentation result (STARE dataset)..... 126

Figure 9.1 The first two curves (top and middle panel) have very different tortuosity but the same Length L and Chord Length χ. The second and last curves (middle and bottom panel) have the same average angular difference despite their different tortuosity. The curve in the bottom panel has a curvature integral of $\pi/2$ whereas the one in the middle panel has curvature integral π, even if that in the bottom panel is clearly perceived as more tortuous. 132

Figure 9.2 Curvature value along a vessel. The dashed lines indicate the hysteretic threshold for the convexity change..... 135

Figure 9.3 Global tortuosity value computed by the algorithm by employing the T' formulation vs. the human assigned tortuosity degree. For a better interpretability of the results, a regression line is superimposed (r=0.861) together with ideal horizontal lines corresponding to margins that could provide a classification by using the estimated tortuosity..... 139

Figure 9.4 Global tortuosity value computed by the algorithm by employing the T formulation vs. the human assigned tortuosity degree. For a better

interpretability of the results, a regression line is superimposed (r=0.876) together with the ideal horizontal lines corresponding to margins that could provide a classification by using the estimated tortuosity..... 140

Figure 10.1 The image shows the estimated vessel diameters for all the tracked vessels in the area of interest. The 6+6 vessels used for the actual computation of parameters are labeled with small circles (green or yellow to identify arteries or veins). The underlying retinal image is the green component of the original color image..... 144

Figure 10.2 Scatter plot of the reference and estimated AVR values..... 147

Figure 10.3 Scatter plot of the reference and estimated CRVE values. 147

Figure 10.4 Scatter plot of the reference and estimated CRAE values. 148

Figure 10.5 Scatter plot of the reference and estimated AVR values..... 149

List of Tables

Table 2.1. Classification of hypertensive retinopathy as proposed in [8] and [9] 31

Table 2.2. Classification of diabetic retinopathy as proposed in [13].....32

Table 2.3. Classification of diabetic macular oedema proposed in [13]. Hard exudates are sign of current or previous macular oedema. Diabetic macular oedema is defined as retinal thickening and requires a three-dimensional assessment 33

Table 3.1 Early Treatment Diabetic Retinopathy Study Seven Standard Field Definitions, from [15], [12], and [7].....41

Table 3.2 Joslin Vision Network Non-mydriatic Retinal Fields.....42

Table 3.3 Results obtained in [1] for four screening protocols.....42

Table 4.1 Absolute error on the estimates of the Zernike coefficients of the aberrating surface.....55

Table 4.2 Absolute error on the estimates of the Zernike coefficients of the aberrating surface obtained with the Direct Maximization method proposed in [30].....55

Table 7.1 Results of the vessel estimation in the 60 images of the DB60 dataset (%). 106

Table 7.2 Results of the vessel estimation in the 20 test images of the DRIVE dataset (%).....106

Table 7.3 Results of the vessel estimation in the 20 images of the STARE dataset (%).....106

Table 8.1 Performance results of the proposed method on our dataset.....123

Table 8.2 Performance results on the DRIVE dataset 123

Table 8.3 Performance results on the STARE dataset.....123

Table 9.1 Correlation of the tortuosity measures ordered with the ophthalmologist tortuosity order.....137

Table 9.2 To each image of the MEH dataset corresponds the tortuosity level assigned by the expert, accompanied with the severity degree as far as the class “2” is concerned). In the rightmost column, the global tortuosity computed by the algorithm.....141

Table 10.1 For each of the 20 DCCT images, both the reference and the estimated CRAE, CRVE, and AVR values are listed. 146

Table 10.2 For each of the 18 ETDRS images, both the reference and the estimated AVR value are listed..... 148

Table 10.3 CRAE, CRVE and AVR values assessed by the UoW, A, B, and C, graders for the DCCT dataset. At the bottom, the correlations among the four graders are provided. 150

Sommario

Questa tesi tratta l'analisi automatica di immagini a colori del fondo dell'occhio. In particolare, essa si focalizza sul progetto di una fundus camera ad ottica adattiva per l'aquisizione di fundus retinici e sull'implementazione di software per l'analisi e la valutazione quantitativa delle retinopatie, prevalentemente ipertensiva e diabetica come naturale ricaduta dei metodi sviluppati.

Sia l'ipertensione che il diabete colpiscono, anche se con modalità e decorso temporale differente, il microcircolo sanguigno. La retinopatia è una delle conseguenze di tale danno circolatorio. La retina ed i vasi retinici sono assai sensibili a cambiamenti nella microcircolazione: è stato dimostrato che i singoli segni della retinopatia hanno una alto valore prognostico per infarto, sclerosi carotidea e danno coronarico. Inoltre, la retinopatia è una malattia sociale, con una ricaduta economica (diretta ed indiretta) elevata: la perdita o la diminuzione della capacità visiva porta infatti ad una ridotta capacità lavorativa e all'impossibilità di condurre una vita indipendente.

Nonostante anche altri organi siano sensibili ad alterazioni del microcircolo sanguigno, la retina ha il grande vantaggio di essere facilmente disponibile ad un controllo non invasivo. Tale caratteristica suggerisce un modo efficiente ed efficace per seguire il decorso di malattie sistemiche associate alla retinopatia. Inoltre, con riguardo alla prevenzione della perdita della vista, il riconoscimento della retinopatia al suo insorgere è il punto più critico per evitare che degeneri in cecità. Ciò è particolarmente importante nella retinopatia diabetica in cui, allo stato attuale della farmacologia, i danni alla retina non recedono con il trattamento farmacologico o col controllo del diabete.

Sfortunatamente, le fasi iniziali della retinopatia sono quasi asintomatiche. Un programma di *screening* potrebbe evitare alla maggior parte della popolazione a rischio lo sviluppo di retinopatie che minaccino la vista. Allo stesso tempo, nel mondo occidentale non ci sono abbastanza risorse, sia in termine di tempo che soprattutto in termine di disponibiltà di oftalmologi esperti, per organizzare uno *screening* di tal genere. E' dunque forte il bisogno di uno strumento che valuti automaticamente la retina, per diagnosticare la presenza e la severità dell'eventuale retinopatia.

Le attuali fundus camera sono in grado di compensare l'aberrazione di fuori fuoco introdotta dall'occhio tramite sistemi mobili di ottiche interne, ma non possono correggere l'astigmatismo oppure le aberrazioni di ordine superiore. Nei primi capitoli della presente tesi si descriverà la realizzazione del prototipo di un sistema di acquisizione che consenta di compensare anche quel tipo di aberrazioni, permettendo così in linea teorica di ottenere immagini di elevata qualità del fondo retinico, anche in pazienti soggetti ad aberrazioni elevate. Le immagini digitalizzate ad alta risoluzione del fondo retinico saranno poi elaborate da algoritmi d'analisi, descritti

nella seconda parte della tesi, dedicati alla diagnosi automatica di alcune patologie dell'occhio.

Il concetto di base dello strumento d'acquisizione sviluppato nei nostri laboratori è quello di inserire lungo il cammino ottico di una fundus camera un'ottica adattiva DM (Deformable Mirror). Il principale problema delle fundus camera convenzionali è che l'informazione per adattare la forma del DM per compensare le aberrazioni presenti è fornita da un complesso e costoso analizzatore di fronte d'onda. La soluzione proposta consiste nel proiettare un pattern noto sul fondo della retina e di acquisirne l'immagine con un sensore dedicato. Analizzando in tempo reale quest'immagine con opportuni algoritmi, sarà possibile ottenere le indicazioni su come l'ottica adattiva debba essere opportunamente deformata per ridurre l'aberrazione introdotta dall'occhio e permettere di acquisire immagini ad alta definizione e senza distorsioni anche in pazienti affetti da aberrazioni non compensabili con le fundus camera ora disponibili. Nonostante test di simulazione su banco ottico abbiano fornito risultati preliminari incoraggianti, la realizzazione di una fundus camera adatta all'utilizzo clinico/diagnostico ha incontrato limitazioni di carattere tecnico relative alla prototipazione dello strumento in ambienti non controllati. L'incidenza dei riflessi spuri, introdotti nel sistema ottico dall'ambiente circostante, sul rapporto segnale-rumore del segnale acquisito sarà materia di ricerca del prossimo futuro.

Le immagini del fondo oculare, ricavate da dataset da noi collezionati e da altri già utilizzati per indagini scientifiche da altri gruppi di ricerca, saranno analizzate con algoritmi sviluppati ad-hoc, in grado di ricavare importanti parametri clinici per la diagnosi delle retinopatie, con particolare attenzione a quelle ipertensiva e diabetica. Nell'ambito di questa tesi saranno prese in esame le *features* dell'apparato vascolare: l'identificazione del reticolo dei vasi (arterie e vene), consentirà la misurazione i suoi principali descrittori geometrici (lunghezza, direzione, calibro, presenza di biforcazioni, etc.); da questi saranno calcolati specifici indici di rilievo diagnostico, che forniranno ai clinici informazioni sul grado complessivo di retinopatia del paziente, la cui significatività è molto importante per la diagnosi delle patologie retiniche. Gli algoritmi presentati in questa tesi rendono possibile pensare ad uno strumento utilizzato sia in ampi programmi di screening delle retinopatia ipertensiva e diabetica, sia per il controllo nel tempo del progredire della malattia. La loro utilià è triplice. In primo luogo, potrebbero essere uno strumento diagnostico di aiuto alla pratica clinica. In secondo luogo, i dettagli quantitativi sulle struttura vascolare della retina potrebbero essere utili nella ricerca medica e per meglio caratterizzare gli sviluppi della retinopatia. Infine, nell'ambito della ricerca farmaceutica, si renderebbe disponibile l'utilizzo di una misura quantitativa e riproducibile dell'evoluzione della retinopatia durante un trattamento farmacologico.

Il software riguardante l'identificazione delle strutture vascolari retiniche è al momento oggetto di valutazione clinica presso il Department of Ophthalmology and Visual Sciences, University of Wisconsin, USA, il cui Fundus Photograph Reading Center ha espressamente dichiarato la sua volontà nell'acquisire il programma come

standard per la determinazione di features diagnostiche, quali gli indici CRAE, CRAE e AVR, come indicatiori del "generalized arteriolar narrowing".

Sempre per quanto riguarda i metodi di identificazione della struttura vascolare della retina, la corrente collaborazione con il Department of Twin Research & Genetic Epidemiology, del King's College London Division of Genetics and Molecular Medicine, St Thomas' Hospital, UK, si è recentemente concretizzata nell'accordo che prevede che un numero superiore a 3500 immagini di fundus retinico (più 10 nuove immagini a settimana) vengano analizzate per scopi clinici con il software da noi sviluppato.

I risultati conseguiti nelle sperimentazioni effettuate e le collaborazioni internazionali in atto con gruppi clinici e di ricerca di rilievo ci rendono abbastanza confidenti riguardo la qualità delle metodologie sviluppate e i potenziali successi del suo impiego, con l'auspicio che futuri miglioramenti possano ampliarne l'utilizzabilità.

Summary

This thesis deals with the automatic analysis of colour fundus images and with the applications of such analysis in the evaluation of hypertensive and diabetic retinopathy. In particular, it aims at developing the project of an adaptive optics fundus camera for retinal fundus acquisition and focuses on the software implementation for the analysis and the quantitative evaluation of retinopathies.

Microcirculation is affected, although with different time courses, by both hypertension and diabetes, and retinopathy is one of the consequences of such circulation damage. The retina and the retinal vessels are very sensitive to changes in microvascular circulation, and it has been demonstrated that single features of hypertensive retinopathy have a strong prognostic value for stroke, carotid stiffness, and coronary disease. Moreover, it must be considered that retinopathy is a social burden, with heavy direct and indirect costs: visual loss in fact reduces the capacity of working and carrying on with an independent life.

Although the retina is not the only organ affected by microcirculation damage, its clinical examination has the undoubted advantage of being non invasive, therefore enabling a cost-effective monitoring of the progression of the systemic diseases associated with retinopathy. The early detection of retinopathy at its onset is central in order to avoid blindness. This is particularly true in the case of diabetic retinopathy, which at the present state of pharmacology does not recede with treatment.

Unfortunately, the first stages of retinopathy are almost asymptomatic. It has been demonstrated that a screening program could save most of the population at risk from developing sight-threatening retinopathy. In the Western world, there are not enough resources, in terms of time and available expert ophthalmologists, for carrying out an extensive screening program. Thus, a reliable automatic tool for evaluating retinopathies is strongly needed.

Current fundus cameras are able to compensate the defocus aberration introduced by the eye by means of a mobile system of internal optics, but they cannot correct for astigmatism or higher order aberrations. The first chapters of this thesis will describe the attempted realization of an acquisition system prototype able to compensate for the second category of aberrations, thus allowing the obtainment of high-quality retinal fundus images, even for patients with high aberration. The second part of this work will propose a software for the automatic processing of retinal fundus images. The algorithms composing this software are designed for geometrically characterizing the vessel structures of the retina, aiming at an automatic diagnosis of the pathologies.

The concept at the basis of the acquisition instrument developed in our laboratories consists in introducing, along the optical path of a fundus camera, a Deformable Mirror (DM) adaptive optics. The main problem of the conventional fundus camera is that the information through which the DM shape is adapted is provided by a com-

plex and expensive wave-front analyzer. The proposed solution consists in projecting a known pattern on the retinal fundus, acquiring the resulting image with a dedicated sensor. Through a real-time analysis of the obtained image with custom algorithms, it will be possible to obtain information about how the DM has to be appropriately deformed in order to reduce the aberration introduced by the eye. This method will allow the acquisition of high-resolution images without distortions even in the case of patients affected by aberrations that are not compensable by the currently available fundus cameras. Although the simulation tests on the optic bench have provided encouraging preliminary results, the development of a fundus camera suitable for a clinic/diagnostic employment has encountered technical limitations, mostly regarding the prototyping of the instrument in an unproofed environment. Indeed, the spurious reflexes introduced in the optical system by the environment excessively reduce the signal-to-noise ratio – a problem which will have to be further investigated in the future.

A number of retinal fundus images, collected by gathering datasets built by us and datasets already used by other teams for research purposes, will be analyzed with custom algorithms able to extract important clinical parameters for the diagnosis of retinopathies. In this context, particular attention will be devoted to the hypertensive and the diabetic pathologies. This thesis concentrates on the extraction and the analysis of the features of the vascular apparatus: the vessel network identification (veins and arteries) will allow the assessment of its main geometrical characteristics (length, direction, caliber, bifurcation, etc.). From these findings, specific indexes of diagnostic relevance will be computed, providing the clinicians with information regarding the patient's retinopathy degree, whose significance is crucial for the diagnosis of retinal pathologies. The algorithms presented in this thesis allow conceiving a tool employable for the mass-screening of both hypertensive and diabetic retinopathies, and also for the monitoring of the progression of the diseases. Its usefulness will be threefold: first of all, it shall provide a diagnostic tool to aid clinical practice; secondly, it will provide quantitative details of the retinal vessel network, thus constituting a useful tool for clinical research; finally, it will enhance pharmaceutical research, providing a quantitative and reproducible assessment of the disease evolution during pharmacological treatment.

The proposed software for the identification of retinal vascular structures is currently the object of clinical evaluation at the Department of Ophthalmology and Visual Sciences, University of Wisconsin, USA, whose Fundus Photograph Reading Center has expressly declared its will to adopt the proposed system as the standard for the determination of diagnostic features.

The recent collaboration with the Department of Twin Research & Genetic Epidemiology, of the King's College London Division of Genetics and Molecular Medicine, St Thomas' Hospital, UK, has brought to the agreement that more than 3,500 retinal fundus images (plus 10 new images per week) will be provided by the Department, being consequently processed and analyzed with our software for the estimation of the clinical indexes.

The results achieved both in the experimentations and thanks to the fruitful international collaboration established with relevant clinical and research groups make us quite confident as regards the quality of the developed methodologies and the potential success of their employment, with the auspice that future improvements can broaden their usability.

Chapter 1

Introduction

Hypertensive retinopathy is associated with systemic arterial hypertension; retinal vascular changes can be seen in both chronic and acute stages. It is likely that an increasing number of patients in the future will suffer from hypertension, a pathology ranked as one of the top-10 risk factors for burden of diseases in developed countries by the World Health Organization. In this context, it must be noticed that ophthalmologists occupy a privileged, central position in the detection of the disease, and consequently in the prevention of the visual loss it causes: indeed, a patient with undiagnosed malignant hypertension will probably consult first an ophthalmologist with a complaint of visual loss.

An even more dramatic situation characterizes diabetes-related retinopathy. Diabetes is a growing epidemic in the world, due to population growth, aging, urbanization and increasing prevalence of obesity and physical inactivity: it is estimated that the population with diabetes will grow by 37% by 2030, and today it already counts around 200 million people worldwide. Following the trend of diabetes, diabetic retinopathy assumes an ever increasing importance as a cause of blindness: in the United States it constitutes the first cause of blindness in subjects in working age, with all the economic and social burdens this implies. The timely diagnosis and referral for management of diabetic retinopathy can prevent 98% of visual loss. It is estimated that the underlying cause of blindness in the majority of diabetic patients is not diabetic retinopathy *per se* but the misdiagnosis of diabetic retinopathy.

Currently, a periodic dilated direct ophthalmoscopic examination appears to be the best approach for a screening with near universal coverage of the population at risk, despite the proved low sensitivity of direct ophthalmoscopy [1], [2], [3]. However, the number of ophthalmologists available is a limiting factor in initiating an ophthalmological screening [4].

With the increasing availability of digital fundus cameras, there is a wide consensus of opinion that an automatic analysis of such digital images might, at least partially, relieve ophthalmologists of the burden of retinopathy screening.

1.1 Aims and Objectives

The aims of the work presented in this thesis are to develop an experimental prototype of adaptive optics fundus camera and a set of tools for the automatic analysis of retinal images.

Adaptive optics (AO) has been recently used for the development of ophthalmic devices. The main objectives of this discipline have been those of obtaining high-resolution images for diagnostic purposes and of estimating high-order eye aberrations. The core of every AO system is an optical device that modifies the wavefront (w-f) shape of the light entering the system: if you know the shape of the incoming w-f, it is possible to correct the aberrations introduced in the optical path from the source to the image. The w-f of the observed object is acquired and analyzed by a suitable w-f sensor – a device which is, though, very expensive. Our goal is to realize an instrument in which the w-f first order aberrations are estimated by a software code that analyzes the image produced by an *ad hoc* point-like source. The information obtained by this software would then be given as an input to a deformable mirror that changes its shape in order to reduce the aberrations. The obvious advantage of this instrument if compared to a classical AO system is that the w-f sensor would no longer be necessary; this would reduce the cost of the instrument, and would avoid the many problems related to the maintenance of the performance of such a device once installed and aligned.

While the first part of this thesis concentrates on the abovementioned hardware issues, the second part deals with the identification of the retinal vessel network, and with its description in terms of position and vessel diameters. The morphology of the vascular structure can be affected by different abnormalities caused by acute pathologies or by early signs of certain systemic disease, such as diabetes and hypertension. Ocular fundus images can provide important information about these signs and their accurate analysis is necessary to improve clinical diagnosis of diseases. An automatic and quantitative assessment of vessel morphological features, such as diameters and tortuosity, can reveal important information on the mentioned diseases. To this aim, the exact layout of all relevant vessels in the image must be extracted. A significant issue in fundus images is that the contrast between vessel and background is often very poor, especially for capillaries. Digital noise represents another critical aspect. In addition, wider vessels often present a bright reflex at the center (the central reflex), which causes their profile to be indistinguishable from the one belonging to two narrow parallel vessels. The approach proposed in this thesis consists in a sequence of independent modules: each of them has a different purpose, and provides the following modules of the framework with processed data and extracted features, so that at the final stage all the required information will be properly utilized. Although the extracted morphology of the vessel network would be a preliminary point to be considered for the recognition of the optic disc and for the elimination of the vascular structures in search of possible non-vascular lesions, in this thesis we will not address

these subjects. Instead, we concentrate on the exploitation of the geometric characterization of the vascular network in order to estimate tortuosity, CRAE, CRVE, and AVR indexes as parameters of clinical relevance for the diagnosis of retinal pathologies.

1.2 Outline

Chapters 2 and 3 are introductory and describe retinal imaging and image acquisition protocols. The fundus camera examination, the appearance of the retina in a fundus image, and the main findings of hypertensive and diabetic retinopathy will be described in Chapter 2. In Chapter 3, the available imaging protocols for retinopathy evaluation will be reviewed, and the one used in acquiring the images of one of the dataset used in this thesis will be described.

Chapters 4 and 5 describe the software employed for the aberration estimation, the scheme of the bench realization of the AO fundus camera prototype, and the experimental setup for the acquisition tests. Since we needed useful fundus images for the tuning and testing of the automatic analysis software, in the interim of the prototype realization we gathered a number of datasets.

In Chapter 6, the list of collected retinal image datasets is given, together with a description of their peculiarity. Most of them have been provided by research and clinical groups working in the field of ophthalmology.

In Chapters 7 and 8, a brief review of previously proposed methods will be followed by a description of the vessel tracking system proposed in this thesis, which is comprehensive of the modules of preprocessing, seed finding, vessel tracing by means of a graph search approach, false vessel detection, caliber extraction and refinement step.

Chapters 9 and 10 concentrate on the clinical usability of the proposed system, particularly as regards the global vessel tortuosity index estimation and the generalized arteriolar narrowing indicators (CRAE, CRVE, and AVR).

Chapter 2

Fundus Imaging and its Findings

In this chapter, a brief review will be presented regarding what is seen in an image from a fundus camera examination and all the most relevant lesions to be found in the hypertensive and diabetic retinopathy.

2.1 Fundus Oculi Examination

The first instrument that allowed the direct examination of the retina was the direct ophthalmoscope, which is still used today. It was first described by Helmholtz at the end of the 19th Century, and since then it has not changed much. In its basic form, it is composed by a light source and a set of lenses. The light is projected through the dilated pupil onto the retina, and the lenses focus on so that the observer can look at the retina. Its use is widespread in the clinical practice, but it has been proved to provide poor sensitivity and results highly dependent on the observer's experience.

In the middle of the 20th Century, the first instrument able to acquire photographs of the retina appeared, i.e. a photographic 35mm back connected to an optic system that focuses on the fundus oculi illuminated by a coaxial flash. This fundus camera enables the photography of different portions of the retina with different magnification ranges, from 10o to 60o. Around 1990, the first digital fundus camera appeared. The optic system is no longer connected to a traditional camera, but to a CCD, and the image is sent to a computer for visualization and storage.

2.1.1 Fundus Oculi Appearance

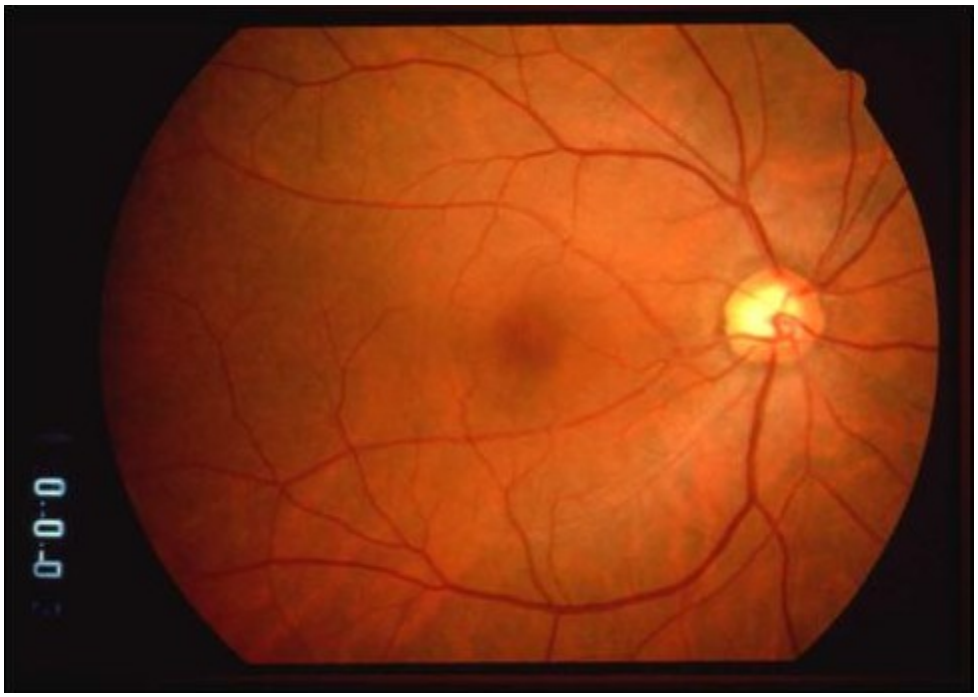


Figure 2.1 An image of a normal fundus oculi.
Papilla (a), fovea (b) and vessel networks are clearly visible

Using a fundus camera, an image of the fundus oculi is acquired. The visible part consists of the retina with its vascular network, the macula, and the optic nerve head. The choroid is the structure below the retina and is usually obscured by it.

The retina is a multilayered structure, transparent except for the deepest layer, the pigmented epithelium which gives to the retina its reddish colour. More superficial than the pigmented epithelium is the sensorial retina, composed by the photoreceptor cells and by the gangliar cells.

The axons of the gangliar cells run to the papilla, also called optic disc or optic nerve head, which is where the bundle of nervous fibers forms the optic nerve, and leaves the optic bulb. From the center of the optic disc, the ophthalmic artery enters into the optic bulb, and subsequently branches to provide vascularization to most of the retina. From the capillary network the venous vessels originate, which flow into the central retinal vein that exits the ocular bulb through the optic disc.

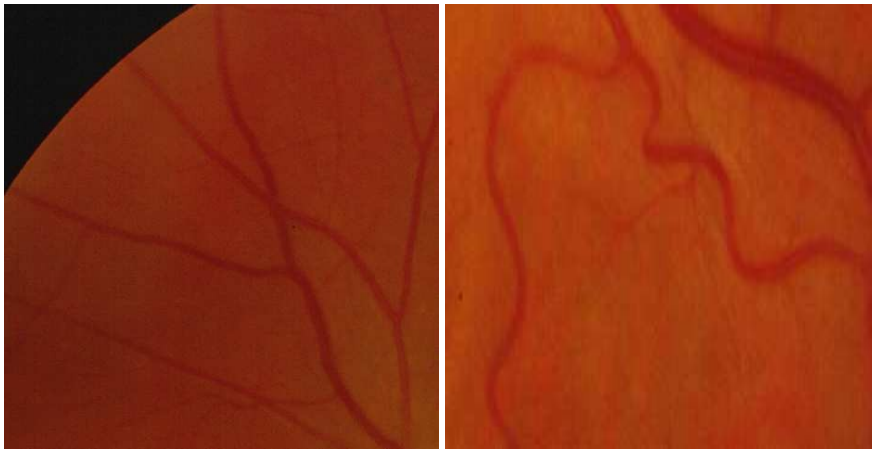
Topologically, the temporal vessel arcades delimit the posterior pole. At the center of the posterior pole, there is the macula: its center is occupied by a small depression, the fovea, that is the region most densely packed with photoreceptor of the retina and is normally the center of vision. The macula is not fed by retinal vessels, but takes its nutrients from the choroidal vessels below the retina.

Choroidal vessels are not usually visible in an image taken with a fundus camera, but if the pigmented epithelium is very lightly pigmented, or in case of pathological

depigmentation, the retina becomes almost transparent and the choroid becomes visible.

2.2 Main Vascular Abnormalities

2.2.1 Tortuosity



(a) (b)

Figure 2.2. Normal vessel course (a) and tortuous vessels (b).

In presence of high blood pressure, vessels may increase in length and vessel walls may thicken. As a result, they become increasingly tortuous. This is at first seen in arteries, while the veins are affected only in more severe stages of retinopathy.

2.2.2 Generalized Arteriolar Narrowing

The earliest fundus change due to hypertension is the thinning of the retinal arterioles. The narrowing of the arterioles is usually proportional to the degree of elevation of blood pressure. However, retinal arteriolar narrowing is imprecisely quantified from a clinical ophthalmoscopic examination, since the examiner should estimate the normal vessel width prior to the narrowing, in order to be capable of evaluating the severity of the latter.

2.2.3 Focal Arteriolar Narrowing

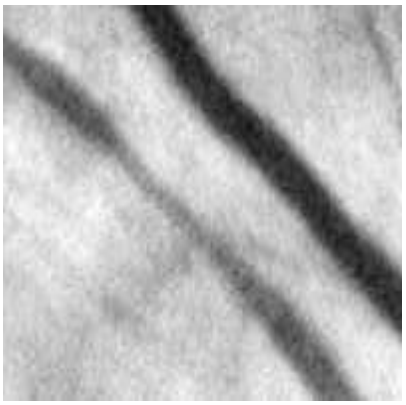


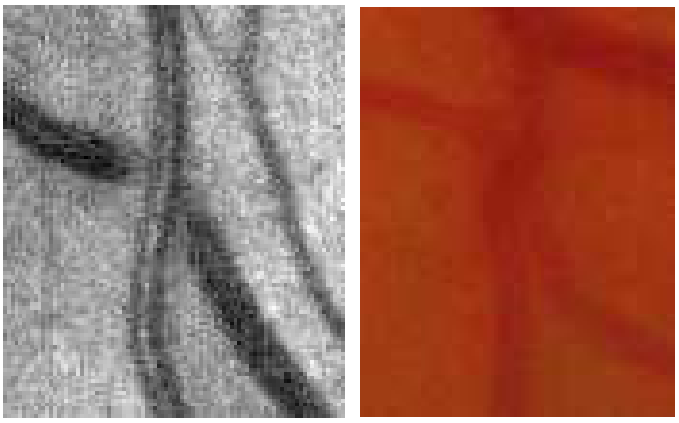
Figure 2.3. A definite focal narrowing

In severe hypertension states, irregularities in the caliber of blood vessels may appear. In arterioles, these are due to localized spasm and contractions of the wall. They appear as a focal thinning of the blood column: the narrowing may increase until the vessels become thread-like.

2.2.4 Bifurcation Abnormalities

Arterial diameters and topography at branch points are believed to conform to design principles that optimize circulatory efficiency and maintain constant shear stress across the network [5]. It has been suggested that arterial diameters at a bifurcation should conform to a power relationship, and arterial branches in various circulation have been shown to obey to this design. It has been shown that bifurcation angles are reduced with increasing hypertension, probably because the atheroma fibrosis of the central artery displaces by contraction the arteries toward the disk. Although the mechanisms of bifurcation changes are not clear, both the branching angles and the value of the junction exponent seem to deviate from its optimal values with age [6].

2.2.5 Crossing Abnormalities



(a) (b)

Figure 2.4. Gunn's sign - vein compression (a) and Salus' sign – vein deflection (b).

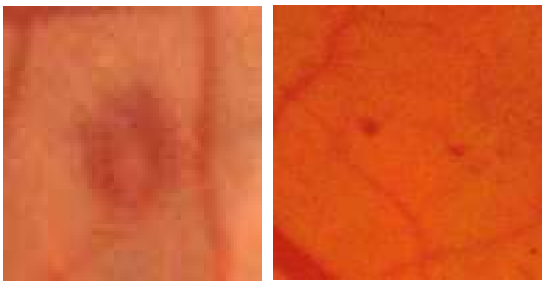
The abnormal changes in arterio-venous crossings result from the thickening of the wall of the arterioles due to hypertension and sclerosis, and associated changes in the veins at the crossings. The first appearance of crossing abnormalities is the compression of the vein by the artery, which may vary in severity from a slight indentation to the complete interruption of the vein where the artery crosses. When the sclerosis in the artery extends to the adventitia of the vein, the blood column in the vein will be partially obscured and appear tapered on each side of the crossing.

The constriction and compression of the veins may impede the blood return, so that the veins become distended for some distance peripheral to the crossing: this is the so-called 'Gunn's sign'.

Arterial sclerosis may cause the detection of the vein from its normal course at the point where the artery crosses. The vein may detect both vertically (dipping under the artery or humping over it), or laterally. In the latter case, instead of crossing the artery obliquely, the vein does so at right angles and appears S-shaped at the bend, – a characteristic which has been referred to as the 'Salus' sign'.

2.3 Major Non-Vascular Findings

2.3.1 Microaneurysms and Red Dots



(a) (b)

Figure 2.5. Large microaneurysm with central reflex (a) and microaneurysm (b)

Retinal microaneurysms constitute the most characteristic lesions caused by diabetic retinopathy, but are present also in other pathologies that affect the microvessels. Micoraneurysms are small dilations of capillary walls. It is not clear whether retinal microaneurysms are due to vessel wall damage or to the beginning of a neovascolarization. However, the visual consequence is the appearance of small saccular structures, of approximate dimension between 10 μm and 100 μm , which in the retinal fluorescein angiography appear as bright hyperfluorescent spots, whereas in colour fundus images appear as round, red spots. They are indistinguishable from small hemorrhages of the same dimension, since they both are small round regions, with a dark red colour. Therefore, both microaneurysms and hemorrhages smaller than the major vein caliber at the optic disc margin (usually 125 ^{1}m), are considered red dots, and evaluated as microaneurysms [7]. On the contrary, any red spot greater than that is considered an hemorrhage, unless features as round shape, smooth margins and a central light reflex suggest that it is probably a microaneurysm.

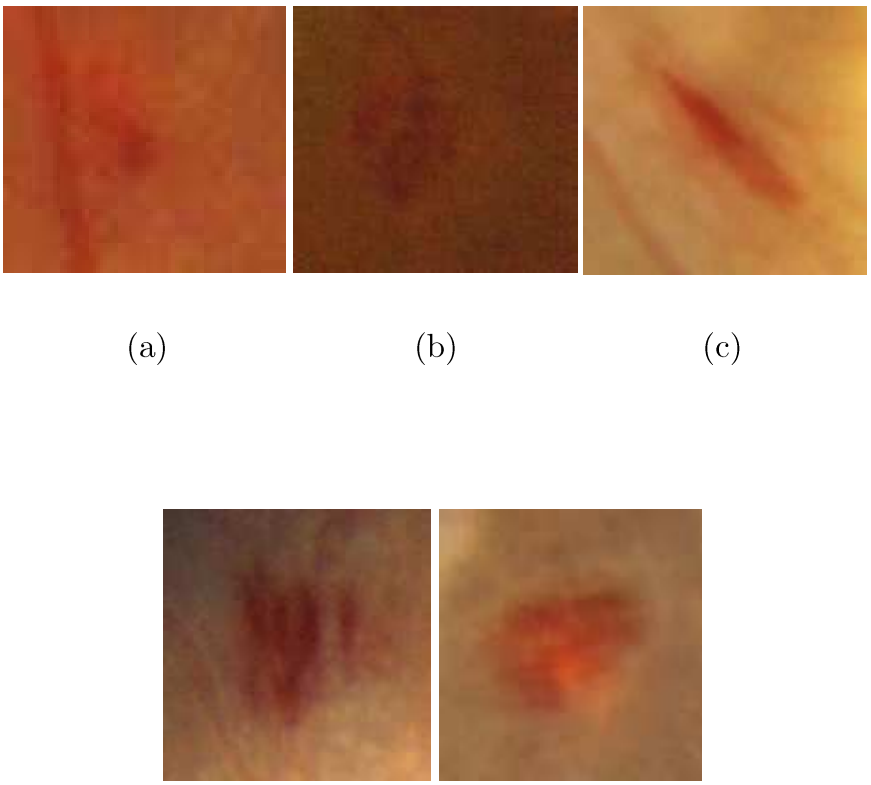
2.3.2 Hemorrhages

Retinal hemorrhages are blood deposits on the retina. Hemorrhages disappear as the blood is reabsorbed with time.

They are due to the breaking of a vessel wall or of a microaneurysm, and the increase in their presence is a clear sign of diffuse retinal damage. They have very different shapes, going from the round red spot with sharp margins, to the blot

hemorrhage. As the blood is reabsorbed, hemorrhage margins fade and the characteristic red colour turns to a faint grayish-red before disappearing completely.

2.3.3 Hard Exudates



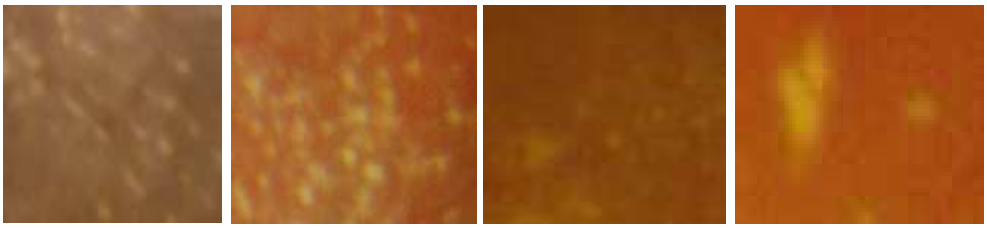
(a) (b) (c)

(d) (e)

Figure 2.6. Small hemorrhage (a), barely visible hemorrhage (b), flame hemorrhage (d), large hemorrhage (d), and bright hemorrhage (e).

Hard exudates are small lipidic and proteinic deposits, which appear as white or yellowish-white areas with sharp margins. They may be arranged as individual dots, confluent patches or in partial or complete rings surrounding microaneurysms or zones of retinal edema. In the more severe cases of hypertensive retinopathy, they appear as a confluent ring around the macula (the macular star).

2.3.4 Cotton Wool Spots



(a) (b) (c) (d)

Figure 2.7. Different hard exudates.



(a) (b) (c)

Figure 2.8. Cotton wool spots.

Cotton wool spots are the consequence of retinal ischemic events, due to precapillary arterioles stenosis. This causes a swelling of the nerve fiber layer, with local deposit of cytoplasmatic material. They are round or oval in shape, white, pale yellow-white or grayish-white, with soft and feathery edges, which give their characteristic aspect and their name. They usually appear along the major vessel arcades, parallel to the nerve fibers, and are sometimes accompanied by the presence of microaneurysms.

2.3.5 Drusen

Drusen are deposits associated with thinning or hypopigmentation of the retinal pigment epithelium. They appear as deep, yellowish-white dots. A stereoscopic view would help to distinguish drusen from hard exudates, since drusen appear very deep, while hard exudates are slightly more superficial. In the protocol used in this thesis the photographs are mono, therefore it is not easy to establish the difference between hard exudates and drusen. Several other features help to distinguish drusen from hard

exudates. Drusen are usually scattered diffusely or scattered near the center of the macula. They are usually round in shape, while hard exudates are usually irregular in shape. Finally, drusen often have a faint border of pigment.

2.4 Hypertensive Retinopathy Grading

The classification of hypertensive changes in the retina in a severity scale was first proposed by Keith [8], in what is now currently known as the Keith-Wegener-Barker grading system. It was subsequently modified by Scheie [9] so as to better separate hypertensive from atherosclerotic abnormalities. In Table 2.1 the two classifications for hypertensive retinopathy are shown. It is worth noting that recent literature challenges the prognostic significance of these classifications. The poor correlation with the severity of hypertension variation at the onset and progression of the clinical signs has suggested the use of a two-grade classification of retinopathies: non-malignant and malignant [10]. This is further confirmed by the fact that the density of perifoveal capillaries and the capillary blood tow velocity analyzed with an angiographic examination correlate more with a two-grade rather than with the classical four-grade classification system. Nevertheless, the Keith-Wegener-Barker is still the *de facto* standard in the evaluation of hypertensive retinopathy.

Keith-Wegener-Baker	
Grade	Features
I	Mild generalized retinal arteriolar narrowing. Increased arterial tortuosity
II	Definite focal narrowing and arterio-venous crossing abnormalities
III	The above and retinal hemorrhages, exudates and cotton wool spots
IV	Severe grade III plus papillar oedema

Scheie	
Grade	Features
1	Barely detectable arterial narrowing
2	Obvious arterial narrowing with focal irregularities and light reflex changes
3	The above plus copper wiring, and retinal hemorrhages and exudates
4	Grade 3 plus silver wire and papillar oedema

Table 2.1. Classification of hypertensive retinopathy as proposed in [8] and [9]

2.5 Diabetic Retinopathy

Two landmark clinical trials set the standard in grading diabetic retinopathy: the Diabetic Retinopathy Study (DRS) [11] and the Early Treatment Diabetic Retinopathy Study (ETDRS) [12]. The ETDRS severity scale was based on the Airlie House classification of diabetic retinopathy and is used to grade fundus photographs. It has been widely applied in research settings and publications, and it has shown satisfactory reproducibility and validity. Although it is recognized as the gold standard for grading the severity of diabetic retinopathy in clinical trials, its use in everyday clinical practice has not proven easy or practical. The first reason for this is that the photographic grading system has 90 levels, many more than what is necessary for clinical care. Given the number of levels to consider, the detailed specific definitions of the levels, and the necessary comparison with standard photographs, it is not surprising that the ETDRS grading procedure is difficult to remember and apply in a clinical setting.

Recently, simplified severity scales have been developed in an effort to improve both the screening of patients with diabetes and communication among caregivers. Yet, to overcome this proliferation of *ad hoc* grading scales, it has been proposed in [13] a Diabetic Retinopathy Disease Severity Scale, in which separate scales were proposed to grade diabetic retinopathy (4 levels) and macular edema (5 levels). The two scales are summarized in Table 2.2 and Table 2.3.

Disease Severity Level proposed in [13]	Disease Severity Level proposed in [13]
No Apparent Retinopathy	No abnormalities
Mild non-proliferative diabetic retinopathy	Microaneurysms only
Moderate non proliferative diabetic retinopathy	More than just microaneurysm but less than severe non proliferative diabetic retinopathy
Severe non proliferative diabetic retinopathy	Any of the following: more than 20 intraretinal hemorrhages in each of 4 quadrants; definite venous beading in 2 or more quadrants; prominent intraretinal microvascular abnormalities in one or more quadrant and no signs of proliferative diabetic retinopathy
Proliferative diabetic retinopathy	One or more of the following: neo vascularization, vitreous or preretinal hemorrhage

Table 2.2. Classification of diabetic retinopathy as proposed in [13].

Disease Severity Level proposed in [13]	Findings Observable on Dilated Ophthalmoscopy
Diabetic macular oedema apparently absent	No apparent retinal thickening or hard exudates in posterior pole
Mild diabetic macular oedema	Some retinal thickening or hard exudates in the posterior pole but distant from the center of the macula
Moderate diabetic macular oedema	Retinal thickening or hard exudates approaching the center of the macula but not involving the center
Severe diabetic macular oedema	Retinal thickening or hard exudates involving the center of the macula

Table 2.3. Classification of diabetic macular oedema proposed in [13]. Hard exudates are sign of current or previous macular oedema. Diabetic macular oedema is defined as retinal thickening and requires a three-dimensional assessment

Chapter 3

Image Acquisition Protocols and Clinical Evaluation

Since the development of the fundus camera, ophthalmoscopic examination has been the standard procedure for evaluating the state of the retina. In the last 15 years, as the fundus camera took ground in the ophthalmologic practice, issues have been raised about the sensitivity and specificity of fundus photographs, and about which acquisition protocols may assure the highest sensitivity and specificity for the early identification of sight-threatening diseases. The *gold standard* for fundus imaging is the ETDRS protocol. Its practical usefulness, however, is reduced because of a number of reasons: the complexity of the acquisition procedure for the camera technician; the complexity of the image evaluation for the ophthalmologist; the discomfort the patient involved in the procedure is subjected to.

The ETDRS, therefore, is not commonly used in the clinical practice, being instead predominantly limited to large research studies. As fundus camera quality increases, a number of protocols simpler than ETDRS have been proposed and validated against the abovementioned gold standard. Even if none has taken solid ground in the clinical practice, the future for the widespread utilization of fundus imaging will be wide angle, few fields photographs protocols The initial part of this Chapter consists of the presentation of a number of protocols which have historically been proposed in the literature, while the final part will be devoted to the protocol NOME, (for the acquisition of the photographs) which constitutes the protocol of one of the datasets employed in this thesis (see Sec. 6.5).

3.1 Diabetic Retinopathy

The grading of Early Treatment Diabetic Retinopathy Study (ETDRS) seven standard field 35-mm stereoscopic color fundus photographs (ETDRS photos) using the modified Airlie House classification is the current gold standard for determining severity of diabetic retinopathy. The Airlie House Classification of Diabetic Retinopathy provides the photographic basis for demonstrating the clinical characteristics and extent of clinically pertinent lesions of diabetic retinopathy. Early Treatment Diabetic Retinopathy Study 35-mm retinal photography and grading protocols provide an established and documented sensitivity for detecting and assessing severity of diabetic

retinopathy. Compared with other retinal imaging methods, such as Polaroid photography or digital-video imaging, 35-mm slide retinal color photographs have the advantages of a large existing database, lower equipment cost, better resolution, and higher color fidelity. Disadvantages associated with 35-mm photography include the requirements for skilled photographers, the need for pupil dilation, uncomfortable examination sessions for the patients, higher costs for film and film handling, delays in film processing, and inefficient archiving with potential for loss or damage of slides. These disadvantages can impact the efficiency, convenience, and cost effectiveness of the procedure and can reduce compliance of patients with annual eye examinations for retinopathy assessment. A number of investigators have evaluated alternatives to ETDRS photos for retinal imaging and assessment of diabetic retinopathy severity.

3.1.1 ETDRS Protocol

The Early Treatment Diabetic Retinopathy Study is built over the Diabetic Retinopathy Study and uses the same protocol of image acquisition. Seven fields, mydriatic, stereoscopic photographs are taken on 35-mm film and subsequently evaluated on light-box. For both for image acquisition and retinopathy grading certified personnel is required. The seven fields are sketched in Figure 3.1, and described in details in Table 3.1. The grading procedure is based on a large set of reference photographs (the standard photographs) for each lesion or abnormality considered. In [12], [7] the complex procedure for classifying the features identified in the set of 7 stereo photographs is reported, together with the grading to provide the level of retinopathy of the eye under examination.

3.1.2 EURODIAB Protocol

A wide-angle retinal photography protocol was developed within the framework of the EURODIAB IDDM Complications Study [14], part of a European Community funded Concerted Action Programme into the epidemiology and prevention of diabetes (EURODIAB). Two 45° colour photographs of each eye are taken. One is centered on the macula, so that the exact centre of the optic disc lay at the nasal end of the horizontal meridian of the field of view. The second is the nasal field, such that the optic disc was positioned one disc diameter from the temporal edge of the field, on the horizontal meridian of the field of view. Considering the partial overlap of the two fields, they provide a retinal view of approximately 80° horizontally by 45° vertically – a view that the authors considered as sufficient for detecting clinically significant or sight-threatening lesions of diabetic retinopathy. In order to test this, the protocol was compared with the recognized *gold standard* 7-field 30° stereo

photography (assessed using a modified Airlie House classification scheme). It was found that occasionally lesions occurred outside the field of view of either one or the other of the protocol [14]

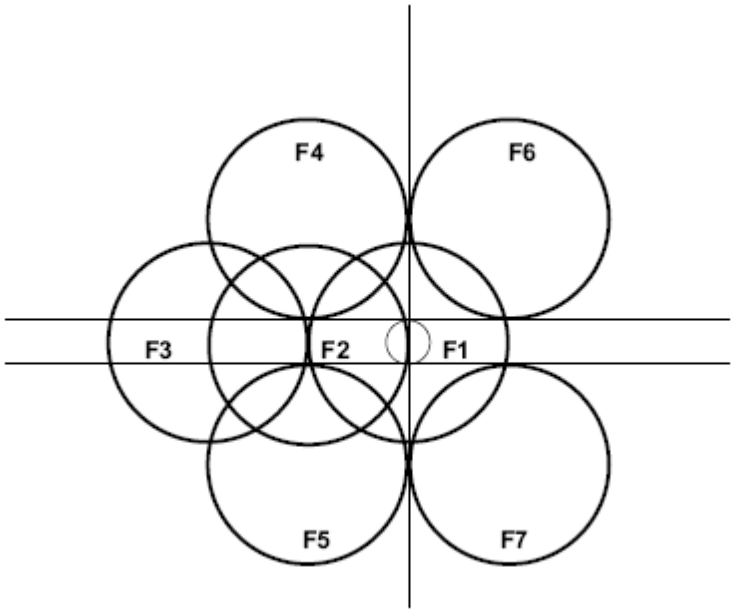


Figure 3.1 Standard ETDRS 7 fields

The simple presence of retinal lesions was correctly detected by both systems in 43 out of 48 eyes, giving 100% agreement on detection. Both systems correctly identified the two known cases of confounding vein occlusion. Using the new system in the case of In eyes with diabetic retinopathy (n = 41), when severity was expressed in three groups (mild background, moderate/severe background and proliferative/photocoagulated), at least one grader (out of five) using the new system matched the verified results in 38 out of 31 (93%) eyes and three or more graders matched in 31 (76%) eyes. The authors claim that the simplicity of application of the system compared to the ETDRS 7-field should prove useful. This would be particularly true especially in large clinical trials, when consistently high-quality ETDRS 7-field stereo images would be difficult to achieve.

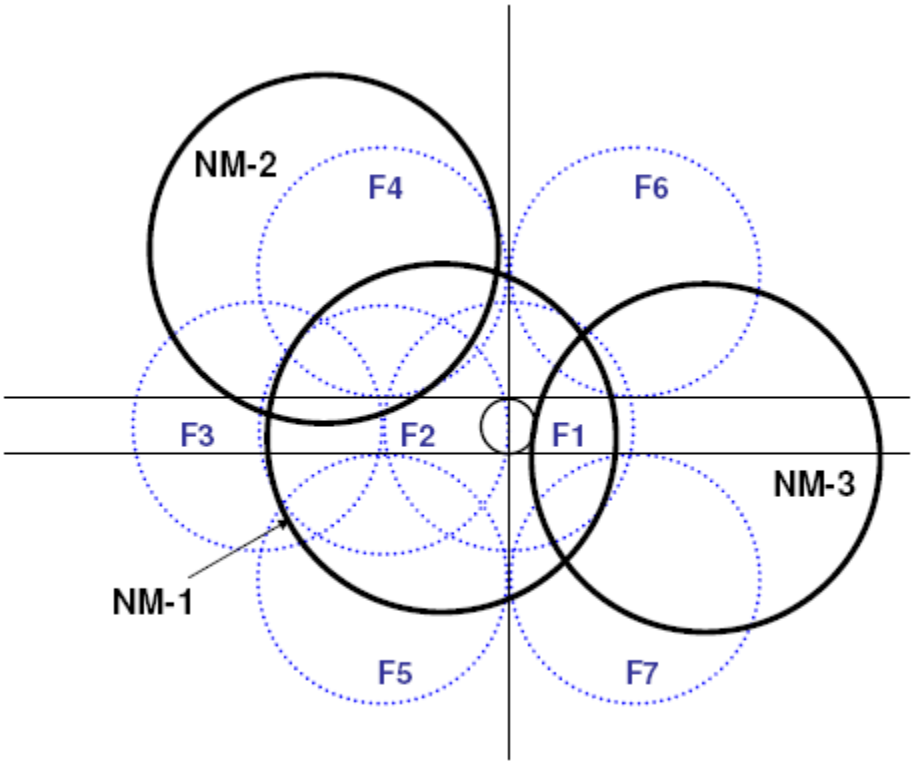


Figure 3.2 Joslin Vision Network Non Mydriatic Fields (black circles), and standard ETDRS 7 fields (dotted blue)

3.1.3 Joslin Clinic Protocol

The Joslin Vision Network (JVN) is a telemedicine platform designed to facilitate the access of patients with diabetes into the chronic disease management program of diabetes within the Joslin Diabetes Eye Health Care Model. This system incorporates a commercially available non-mydriatic retinal fundus camera optimized for low-light level imaging of the retina. The protocol [15], developed with the aim of reducing patient discomfort and of providing an easy picture taken by non-certified photographers, is a three field non-mydriatic 45° photographs. These fields are described in Table 3.2, and they are represented in Figure 3.2 superimposed to the ETDRS protocol. This protocol was validated against the ETDRS 30° 7-field stereo. It was demonstrated that the determination of clinical level of diabetic retinopathy using the JVN stereoscopic non-mydriatic digital-video color retinal images from three distinct retinal regions obtained using a 45° non-mydriatic camera optimized for low-light level imaging (JVN images) is in substantial agreement (k =0.65) with dilated ETDRS seven standard field 35-mm stereoscopic 30° retinal photography (ETDRS photos).

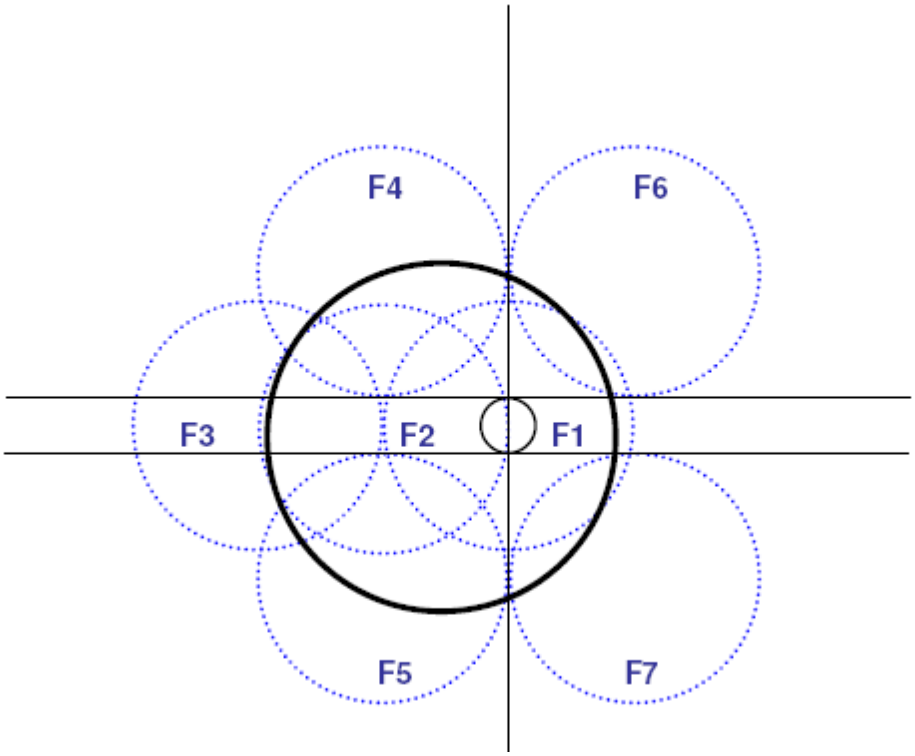


Figure 3.3 Non Mydriatic Monochromatic Field proposed in [16] (black circle), and standard ETDRS 7 fields (dotted blue)

3.1.4 Single Field Monochromatic

In [16], a single wide angle field, monochromatic, was tested against the ophthalmoscopy conducted by an experienced ophthalmologist and against the ETDRS 7-field stereo. The single field of the 45° photograph was centered on a point halfway between the temporal edge of the optic disk and the fovea, and included areas of the retina on either side of both structures (Figure 3.3). Taking the ETDRS retinopathy level 35 as threshold for referral, digital imaging had a sensitivity of 78% and specificity of 86% when compared with standard seven-field color photography.

3.1.5 Fields Protocol

In [17], a non-mydriatic digital fundus photography without pupillary dilation was tested using a non-mydriatic 45 Topcon TRCNW6 fundus camera (Topcon Europe, Rotterdam, The Netherlands) for sensitivity and specificity against the seven ETDRS mydriatic stereo standard fields. in the Early Treatment Diabetic Retinopathy Study

(ETDRS) for DR screening. Five 45°non-stereoscopic images of five overlapping fields were taken for each eye: one image was centered on the macula, including the optic disc, and one each on the nasal, temporal, superior and inferior fields. The sensitivity of detection for moderately severe to severe forms of DR ranged from 92% to 100% and the specificity from 85% to 88%.

3.1.6 Single-Field Colour Protocol

In [1] four screening methods (an exam by an ophthalmologist through dilated pupils using direct and indirect ophthalmoscopy; an exam by a physician assistant through dilated pupils using direct ophthalmoscopy, a single 45° retinal photograph without pharmacological dilation; a set of three dilated 45° retinal photographs) were compared with a reference standard of stereoscopic 30° degrees retinal photographs of seven standard fields read by a central reading center. Sensitivity, specificity, and positive and negative likelihood ratios were calculated after dichotomizing the retinopathy levels into none and mild non-proliferative versus moderate to severe non-proliferative and proliferative. The sensitivities, specificities, and positive and negative likelihood ratios are summarized in Table 3.3. In [3], diabetic patients referred for screening were studied in a prospective fashion. A single 45° fundus image was obtained using the non-mydriatic digital camera, and the validation was performed using as ground truth the diabetic retinopathy grading by a consultant ophthalmologist. The sensitivity for detection of any diabetic retinopathy was 38% and the specificity 95%.

3.2 Hypertensive Retinopathy

3.2.1 ARIC Protocol

The Atherosclerosis Risk in Communities (ARIC) Study is an epidemiological research study of the major factors contributing to the occurrence and trend of cardiovascular disease in middle-aged adults in the United States. The ARIC Study has two main objectives: firstly, to investigate the factors associated with both atherosclerosis and incidence of clinical cardiovascular disease, and secondly to measure coronary heart disease occurrence and trends and relate them to community levels of risk factors, medical care and atherosclerosis. Fundus photographs were used to evaluate changes in the retinal vasculature (presumed to be related to hypertension and/or arteriolar sclerosis) that may be prognostic for various cardiovascular outcomes, but other significant retinal conditions were noted, such as diabetic retino-

pathy or vascular occlusions. Within the context of the ARIC Study, the protocol consists of one non-mydriatic 45° retinal photograph. The photographs are subsequently sent to the ARIC Retinal Reading Center for assessment of retinal status [18], [19]. To obtain consistent field specification even when inexperienced technicians take the photographs, the camera used in the ARIC study is provided with a mask on which to align the optic disc. These aligning masks are provided by the Retinal Reading Center and, when, properly attached to the monitor, they position the optic nerve centered from top to bottom and the nasal edge of the optic nerve falls between 1.5-2 optic disc diameters from the nasal edge of the photograph.

3.3 Protocol for Hypertensive Retinopathy

In the clinical routine, when checking the retina for retinopathies, it is common to find wide-angle photographs, digital for the newest systems or film for the older, with a varying number of fields, depending on the whim of the taker, and on his/her opinion regarding the presence of significant lesions in non-standard fields. Nevertheless, the most usual field employed as a starting point is the one centered on the macula: this is the most important area to be checked for sight-threatening lesions. Combining a macular field with wide-angle photographs, it allows to evaluate most of the vascular arcades for abnormalities, and to have both the macula and the optic disc available for examination. Even if photographs are non-stereo, optic disc and macula appearances can suggest and sometimes clearly point out the presence of swellings and oedema.

The acquisition protocol used to build one of the datasets used in this thesis (as described in Sec. 6.5) is a single-field, non-stereo, mydriatic photograph with a 50° angle, and centered on the macula.

3.4 Conclusions

Several studies [20] have showed that, as a tool to detect vision-threatening retinopathy, single-field fundus photography interpreted by trained readers has sensitivity ranging from 61% to 90% and specificity ranging from 85% to 97% when compared with the gold standard reference of stereo-photographs of 7 standard fields. When compared with the dilated ophthalmoscopy carried out by an ophthalmologist, single-field fundus photography has sensitivity ranging from 38% to 100% and specificity ranging from 75% to 100%. Therefore, although single-field fundus photography is not a substitute for a comprehensive ophthalmic examination, it can serve as a screening tool to identify patients for referral for ophthalmic evaluation and management.

The advantages of single-field fundus photography interpreted by trained readers are ease of use (only one photograph is required), convenience, and ability to detect retinopathy. These advantages, together with the additional consideration regarding the widespread utilization of wide-angle retinal photography as examination procedure in the clinical practice, have led to the choice of a single 50° field centered on the macula as the imaging protocol for this thesis.

ETDRS Field	Field Definition
F-1	Optic Disc: 30∘ field focused centrally on the optic disc
F-2	Macula: 30° field focused on the center of the macula
F-3	F-3 Temporal to Macula: 30° field focused so the nasal edge of the field crosses the center of the macula
F-4	F-4 Superior temporal: 30° field focused so the lower edge of the field is tangent to a horizontal line passing through the upper edge of the optic disc and the nasal edge of the field is tangent to a vertical line passing through the center of the disc
F-5	F-5 Inferior temporal: 30° field focused so the upper edge of the field is tangent to a horizontal line passing through the lower edge of the optic and the nasal edge of the field is tangent to a vertical line passing through the center of the disc
F-6	F-6 Superior nasal: 30° field focused so the lower edge of the field is tangent to a horizontal line passing through the upper edge of the optic disc, and the temporal edge of the field is tangent to a vertical line passing through the center of the disc
F-7	F-7 Inferior nasal: 30° field focused so the upper edge of the field is tangent to a horizontal line passing through the lower edge of the optic disc, and the temporal edge of the field is tangent to a vertical line passing through the center of the disc
F-8	30° field focused outside the seven standard fields

Table 3.1 Early Treatment Diabetic Retinopathy Study Seven Standard Field Definitions, from [15], [12], and [7]

JVN Field	Field Definition
NM-1	45° field focused centrally between the temporal margin of optic disc and the center of the macula: Center the camera on the papillomacular bundle midway between the temporal margin of the optic disc and the center of the macula. The horizontal centerline of the image should pass directly through the center of the disc. A stereoscopic image is obtained by capturing one image through the left aspect of the pupil opening, shifting the camera laterally, and then capturing a second image through the right aspect of the pupil. A slight delay between the first and second image may be necessary to allow for adequate pupil mydriasis
NM-2	45° field focused superior temporal to the optic disc: Center the camera laterally approximately one-half disc diameter temporal to the center of the macula. The lower edge of the field is tangent to a horizontal line passing through the upper edge of the optic disc. This image is taken temporal to the macula but includes more retina nasal and superior to the macula than standard Field 2
NM-3	45° field focused nasal to the optic disc: This field is nasal to the optic disc and may include part of the optic disc. The horizontal centerline of the image should pass Tangent to the lower edge of the optic disc.
NM-4	45° field focused temporal to the macula (obtained through dilated pupils only)
NM-5	45° any optional field focused beyond the def initions of NM fields 1-4

Table 3.2 Joslin Vision Network Non-mydriatic Retinal Fields

	Ophthal-mologist	Physician Assistant	Single non-mydriatic photograph	Three mydriatic photographs
Sensitivity	0.33	0.14	0.61	0.81
Specificity	0.99	0.89	0.85	0.97
Positive ratio	72	12	4.1	54
Negative	0.67	0.87	0.46	0.19

Table 3.3 Results obtained in [1] for four screening protocols

Chapter 4

The Adaptive Optics System: Compensation of Aberrations

Adaptive optics (AO) has been recently used for the development of ophthalmic devices. Its main objective has been that of obtaining high-resolution images for diagnostic purposes or to estimate high-order eye aberrations. The core of every AO system is an optical device that is able to modify the wavefront shape of the light entering the system; if you know the shape of the incoming wavefront, it is possible to correct the aberrations introduced in the optical path from the source to the image.

The aim of this chapter is to demonstrate the feasibility, although in a simulated system, of estimating and correcting an aberrated wavefront shape by means of an iterative gradient-descent-like software procedure, acting on a point source image, without expensive wavefront sensors or the burdensome computation of the point-spread function (PSF) of the optical system. In such a way, it is possible to obtain a speed and repeatability advantage over classical stochastic algorithms. A hierarchy in the aberrations is introduced, in order to reduce the dimensionality of the state space to be searched.

The proposed algorithm is tested on a simple optical system that has been simulated with ray-tracing software (ZEMAX), with randomly generated aberrations.

4.1 Software Analysis for the Compensation of the Primary Aberration

In the early days, adaptive optics (AO) were used mainly in astronomy to compensate for atmospheric turbulence. Recently, applications for ophthalmology have received growing attention ([21], [22], [23], and [24]). Their main objectives are to obtain higher-resolution images for diagnostic purposes, estimate high-order eye aberrations, or in experimental ophthalmology [25], [26]. In particular, it has been shown that the compensation of the optical aberrations introduced by the eye can greatly improve the quality of retinal images.

The core of every AO system is an optical device able to modify the wavefront shape of the light entering the system. Ideally, by carefully controlling this device, it

is possible to introduce a deformation to the wavefront that is the exact complement of the one that the light has undergone along its path, therefore imposing a perfectly spherical shape to the wavefront. To perform such control it is crucial to estimate the shape of the incoming wavefront. For applications in ophthalmology, this can be achieved in a variety of ways. The most widely used techniques include the aberroscope, the Hartmann–Shack wavefront sensor [27], the psychophysical methods [28], and the double-pass methods which estimate the eye point spread-function (PSF) [29].

Recently, no-wavefront sensor systems that make use of model-based approaches [30] [31] or stochastic optimization techniques have been proposed. In particular, the latter search the state space of the AO in order to obtain the best configuration for reducing optical aberrations ([32], [33], and [34]) that are indirectly measured by some image quality metrics ([34], [35], and [36]). Given the high dimensionality of the state space, and the possible presence of local extrema for the objective function, these methods provide variable results and need a large number of iterations to converge. In contrast, the model-based optimization scheme ([30], [31]) makes use of only N+1 measurements of a spot image for the estimation of N aberration coefficients.

This chapter demonstrates the feasibility, although in a simulated system, of estimating and correcting the wavefront shape by means of an iterative software procedure, which exploits *ad hoc* cost functions and analyzes a small subset of states at a time. In this way, the dimensionality of the search space is reduced, achieving faster convergence and better sensitivity.

4.1.1 The Zernike Polynomials

Thanks to their characteristics, Zernike polynomials are particularly attractive for wavefront representation. They are a complete set of polynomials orthogonal over the interior of the unit circle and they can be written in polar coordinates as products of angular functions and radial polynomials [37]. To estimate the aberrations of the wavefront, the Zernike coefficients can be evaluated.

Following the Air Force enumeration scheme, used by the ray-tracing software ZEMAX (ZEMAX Development Corporation, San Diego, California), the coefficients that can be estimated using the described algorithm are the z_4 term, which represents defocus; z_5 and z_6, which are associated with astigmatism at 0° and 45°, respectively, plus defocus; z_7, which represents the coma (i.e. the comatic aberration) along the x plus x tilt; z_8, which represents the coma along the y axis plus y tilt; and finally z_9, which represents the spherical aberration. Hence, the objective is to estimate the coefficient vector $Z = \{z_4, ..., z_9\}$.

Given an image of a point source, it is possible to correct the aberrations introduced in the optical path from the source to the image, making use of an AO Σ_2,

whose surface is defined by the Zernike coefficient vector Z_{Σ_2}, describing its wavefront modification. This method does not make use of either wavefront sensors nor of the burdensome computation of the PSF of the optical system. For a generic optical system, a detector positioned on its image plane will acquire an image I. When a point source S is present, the image of S on the image plane is P and its quantized and acquired version is $Pq \subseteq I$. The proposed method analyzes the image I, obtaining information on the aberrations that are present, and then modifies Σ_2 by varying its Zernike coefficients. Then a new image I is acquired to test the aberration correction introduced, and then the algorithm is iterated until no residual aberration is detected.

To develop such an algorithm, a hierarchy in the aberrations is introduced, so that aberrations higher in the hierarchy can be estimated without knowledge of the aberrations lower in the hierarchy. By this means, the system achieves a dimensionality reduction of the search space in addition to that obtained by considering only six Zernike coefficients: in fact, the hierarchy will aim at the optimization of six one-dimensional problems instead of one six-dimensional problem.

4.1.2 Aberration Hierarchy

To obtain the estimation of the Zernike coefficient vector Z, a six-dimensional space must be searched, leading to a difficult optimization task. To increase the convergence speed and decouple the aberration interactions, it we must find a way to divide the six-dimensional optimization problem into some smaller-dimensional optimizations: ideally, the aim is to end up with six one-dimensional problems. In order to provide this dimensionality reduction in the estimation of Z from I, it is important to find a way to obtain information on single aberrations, without the procedure being influenced by the possible presence of other aberrations. Even if this is not possible in general, a less stringent requirement can be met. A hierarchy among the aberrations can be devised: one aberration can be estimated regardless of the presence of aberrations lower in the hierarchy, whereas it cannot be estimated reliably as long as aberrations that are higher in the hierarchy are present. Among the Zernike coefficients to be estimated here, the highest in the hierarchy is z_9, related to the spherical aberration. Then there are z_7 and z_8 related to a coma aberration. In fact, when a coma is present but there is no spherical aberration, a characteristic tail is present (see Figure 4.1) in P_q (the acquired image of S), which makes it clearly identifiable. At a lower step, z_4 is found, related to focus shift, and finally the coefficients z_5 and z_6 of astigmatism follow. Even if intuitively astigmatism should come before defocus in the hierarchy, it is easily shown that the estimation of astigmatism in the presence of an unknown defocus is not possible. The astigmatism axis changes with focus position (see Figure 4.2), thus making it almost impossible to identify the sign and amplitude of its two Zernike coefficients without knowing the wavefront phase. In contrast, after a focus shift correction, the astigmatism would present itself

in the circle of minimum confusion. Even if no information on its axis can be gathered at this point by simply analyzing I, it is shown that the astigmatism can be corrected and the coefficients z_5 and z_6 can be estimated. With this hierarchy, and considering the unavoidable coupling between z_7 and z_8, and between z_5 and z_6, we can reduce the original problem of estimating $Z \in \mathbb{R}^6$ into the sequence of four problems of dimensionality at the most in $\mathbb{R}^2$: first $z_9 \in \mathbb{R}$ will be estimated, then $[z_7, z_8] \in \mathbb{R}^2$, subsequently $z_4 \in \mathbb{R}$, and finally $[z_5, z_6] \in \mathbb{R}^2$.

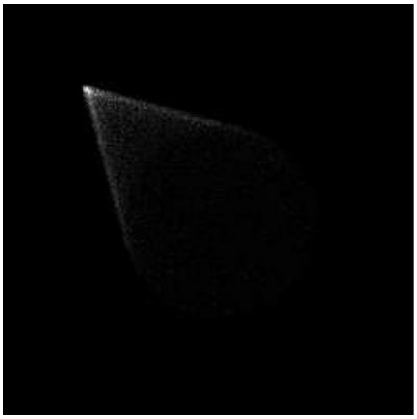
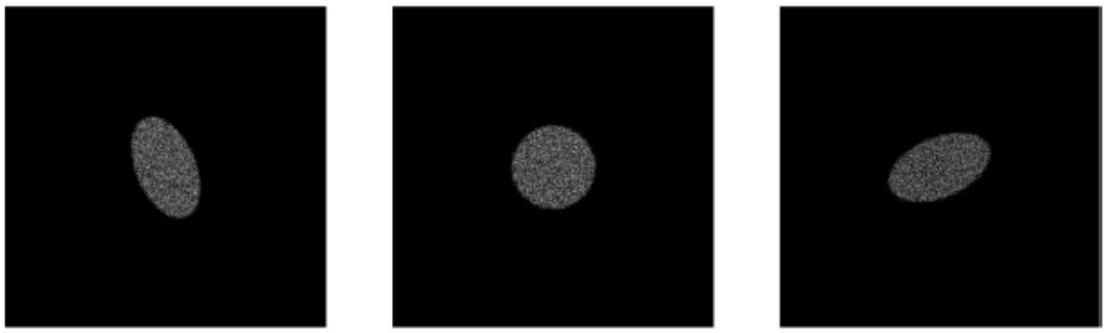


Figure 4.1 Typical image of a point source image affected by coma.



(a) (b) (c)

Figure 4.2 Point source image affected by astigmatism at different focal plane positions. The position (b) corresponds to the so-called "circle of least confusion."

4.1.3 Aberration Correction

The described aberration ranking allows the development of a system that progressively corrects the aberrations, starting from those highest in the hierarchy and ending with the lowest. An outline of the proposed system is shown in Figure 4.3: after the image I is acquired, a spherical aberration is corrected by iteratively modifying the Zernike coefficient z_{9,Σ_2} of the AO until no further improvement can be

obtained. Then the algorithm detects and corrects coma, defocus, and finally astigmatism.

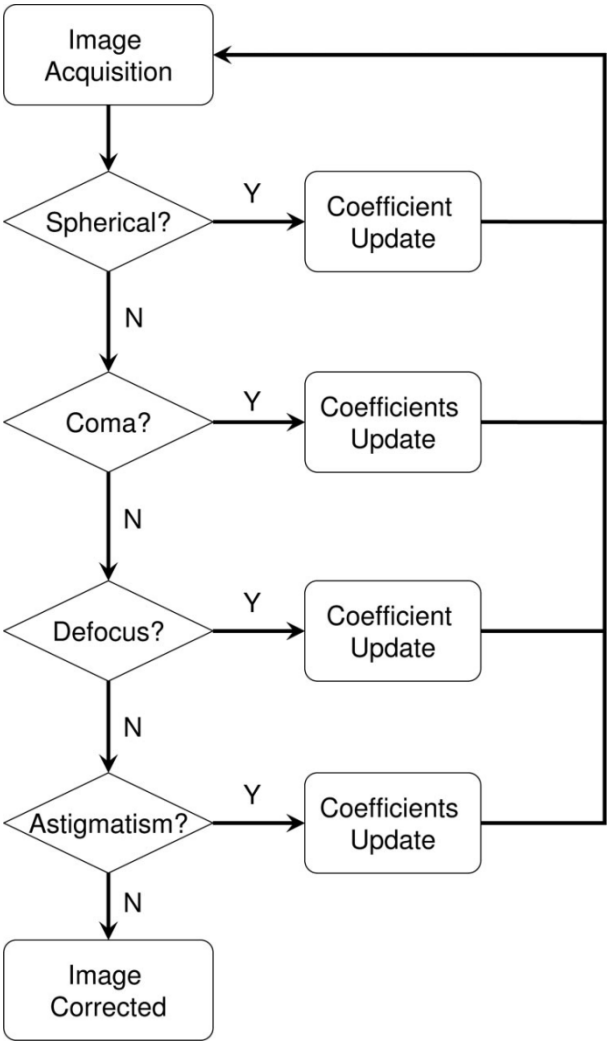


Figure 4.3 Flow chart of the proposed algorithm. Zernike coefficients related to each aberration are hierarchically and separately estimated.

4.1.3.1 Spherical Correction

Spherical aberrations cause the probe point image P to spread, scattering the light power symmetrically around the center of P. To estimate the amount of spread, two different metrics in a two-stage process have been used: the first stage tries to maximize the amount of power present in the image by changing the coefficient z_9 in the direction that locally increases the S_1 image metric described by Muller [35]:

$$S1 = \int I(x, y)\, dxdy. \tag{4.1}$$

In the second stage, the mean intensity value μ_I of the nonzero pixels of the image I is maximized: in this way we obtain an image with the power as concentrated as possible around P_q. To have a coherent approach in the correction of the various aberrations considered, the maximization problem is recast as a minimization problem. Hence, the objective function to be minimized is

$$J_1 = \begin{cases} -S_1, & \text{for the stage 1} \\ -\mu_I, & \text{for the stage 2} \end{cases} \tag{4.2}$$

At every iteration i of the optimization procedure, $z_{9,\Sigma_2}(i)$ is set to

$$z_{9,\Sigma_2}(i) = z_{9,\Sigma_2}(i-1) + \delta_z(i) \tag{4.3}$$

where $\delta_z(i)$ is the optimization step varying the value of the z_9 coefficient. During the procedure, the $\delta_z(i)$ magnitude is decreased and its sign changed depending on the values of $S_1(i-1)$ and $S_1(i-2)$ in the first stage, and on the values of $\mu_I(i-1)$ and $\mu_I(i-2)$ in the second stage. The step update is then

$$J_s(i-2) \geq J_s(i-1) \rightarrow \delta_z(i) = \delta_z(i-1) \tag{4.4}$$

$$J_s(i-2) < J_s(i-1) \rightarrow \delta_z(i) = -0.5\,\delta_z(i-1) \tag{4.5}$$

4.1.3.2 Coma Correction

A point source image of a point affected by a coma is characterized by the presence of a tail along the coma axis. The presence of a coma can be detected by looking at the distance between the centroid $c_1 = [x_{c_1}, y_{c_1}]$ of the nonzero pixels of I and the centroid $c_2 = [x_{c_2}, y_{c_2}]$ of the pixels weighted by their gray-level value (related to the power density); the two centroids are shown in Figure 4.4 in a sample image.

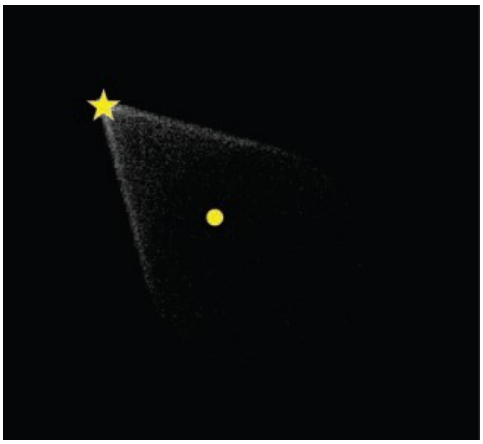


Figure 4.4 Coma detection: the white star is c_2 and the white circle is c_1, as defined in the text.

The more the two calculated centroids are apart, the more the coma is assumed. However, since it may happen that part of the coma tail is outside the field of view, thus creating local minima that impair the algorithm, this distance is weighted by the negative of the light power in the image. The function to be minimized is

$$J_c = (1 - \int I^2(x,y)\,dxdy)\|c_1 - c_2\|_2 \tag{4.6}$$

where $\|\cdot\|_2$ is the L_2 norm. By looking at the covariance of the nonzero pixels (which represent P_q), the angle ϑ_{coma} of the coma axis can be estimated from the eigenvector associated with its highest eigenvalue. The Zernike coefficients related with coma z_{7,Σ_2} and z_{8,Σ_2} are varied of a quantity δ_z so to compensate for the aberration, they are applied to the adaptive optics surface Σ_2. At every iteration i:

$$\mathrm{z}_{7,\Sigma_2}(i) = \mathrm{z}_{7,\Sigma_2}(i-1) + \delta_z(i)\cos\left(\vartheta_{coma}(i)\right) \tag{4.7}$$

$$\mathrm{z}_{8,\Sigma_2}(i) = \mathrm{z}_{8,\Sigma_2}(i-1) + \delta_z(i)\sin(\vartheta_{coma}(i)) \tag{4.8}$$

In the case of the coma, since the aim is to minimize J_c, the decreasing strategy for the step I is

$$J_c(i-2) > J_c(i-1) \rightarrow \delta_z(i) = \delta_z(i-1) \tag{4.9}$$

$$J_c(i-2) \leq J_c(i-1) \rightarrow \delta_z(i) = -0.5\,\delta_z(i-1) \tag{4.10}$$

4.1.3.3 Focus Shift Correction

Once the spherical and coma aberrations have been corrected, the optical system might still be affected by focus shift and astigmatism. The acquired image P_q of S, when affected by astigmatism alone, would appear as a circular spot with a dimension depending on the astigmatism, whereas it would become elongated when some focus shift is present in the system. Therefore, in order to correct the focus shift, the algorithm aims at obtaining a P_q that is as circular as possible, and as small as possible. This can be achieved by means of a min–max optimization of the covariance matrix: the objective is to minimize the maximum value in the covariance matrix. A two-stage process similar to the one used for correcting the spherical aberration is used. The first stage minimizes the opposite of the image intensity in a small disk A centered on P_q, corresponding to the opposite of the metric S_5 in [33]:

$$S_5 = \int I(x,y)dxdy \tag{4.11}$$

whereas in the second stage the maximum of the covariance matrix of the pixels in A, $\max(\mathrm{Cov}(A))$, is minimized. The objective function J_d to be minimized for defocus correction is then

$$J_1 = \begin{cases} 1 - S_5, & \text{for the stage 1} \\ \max(\mathrm{Cov}(A)), & \text{for the stage 2} \end{cases} \tag{4.12}$$

the coefficient update at the *i-th* iteration is

$$\mathrm{z}_{4,\Sigma_2}(i) = \mathrm{z}_{4,\Sigma_2}(i-1) + \delta_z(i) \tag{4.13}$$

with the step δ_z update rules

$$J_d(i-2) > J_d(i-1) \rightarrow \delta_z(i) = \delta_z(i) \tag{4.14}$$

$$J_d(i-2) \leq J_d(i-1) \rightarrow \delta_z(i) = -0.5\,\delta_z(i) \tag{4.15}$$

4.1.3.4 Astigmatism Correction

Finally, astigmatism has to be corrected. At this point, when the focus shift has been corrected, no information on the astigmatism axis can be obtained by looking at *I*. Therefore there is no possibility to have a measure of the influence of the coefficient z_5 and z_6 separately. When the image is perfectly focused, astigmatism causes P_q to appear as a circle, so the objective of the correction is to reduce the dimension of

P_q. To evaluate the dimension of P_q, the maximum eigenvalue λ_{max} of the covariance matrix of the brightest pixels in I is used. Minimization of $J_a = \lambda_{max}$ is supposed to yield the desired aberration correction.

Since no information on the direction of the astigmatism can be gathered explicitly, each iteration of the optimization procedure has to evaluate the gradients of J_a with respect to both z_5 and z_6 separately, modifying the sign and magnitude of steps δz_5 and δz_6 accordingly.

4.2 Simulation Setup

To test the proposed algorithm, a simple optical system has been simulated as shown in Figure 4.5. This system has been kept as simple as possible, in order to evaluate the possibility of estimating the Zernike coefficients by means of a software analysis of the point source image. In this way the algorithm performance is tested *per se*, without considering any other aspect of wavefront correction and imaging.

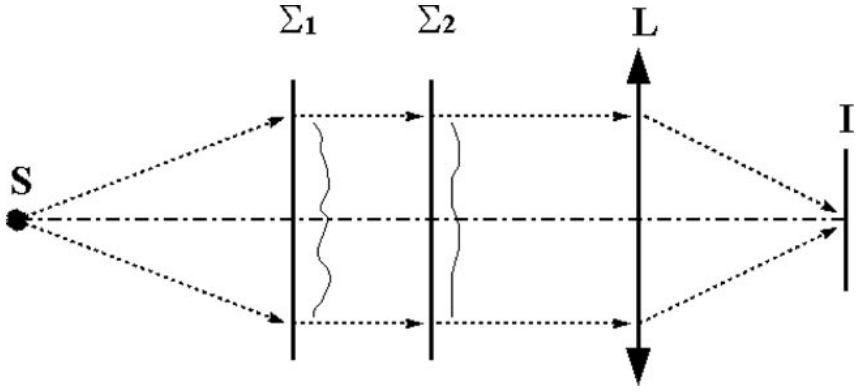


Figure 4.5 Equivalent model of the simple optical system simulated for testing the aberration correction algorithm.

S is an on-axis source at infinity, equivalent to a source with a finite dimension of 3.6 arc sec. Σ_1 and Σ_2 are ideal surfaces able to modify the shape of the wavefront passing through them. The modification introduced depends on the values of the Zernike coefficient vectors Z_{Σ_1} and Z_{Σ_2} that describe the surfaces. Finally, an ideal paraxial lens L with a 100 mm focal length focuses the light beam on the detector located on the focal plane. In the specific setting used, the detector samples the image with a resolution of 2 μm providing an image of 500 × 500 pixels. Hence, due to the optical geometry of the system and the quantization introduced by the detector, the aberration-free image of S is represented on the detector with an 8 × 8 pixels square P_q.

In this simple and ideal system, the surface Σ_1 introduces the fixed but "unknown" optical aberrations, whereas Σ_2 acts as the aberration-correction system. Each com-

ponent z_i, with $i = 4, \ldots, 9$, of the coefficient vector $\mathbf{Z}_{\Sigma_1}$ describing the aberrations of the system has been drawn from a uniform distribution $U[-0.1,\ 0.1]$. Fifty different $\mathbf{Z}_{\Sigma_1}$ were generated to test the ability of the proposed algorithm to correct the optical aberrations introduced by Σ_1. Along with the results obtained with the proposed methods, the Zernike coefficients were also estimated through the direct maximization approach proposed in [30]. The coefficient vector $\mathbf{Z}_{\Sigma_2}$ providing the $N+1$ measurements needed were located at the vertices of a simplex distant 0.1 from the origin.

In this way the N-dimensional simplex lay close to the N-dimensional hypercube that the coefficients were drawn from.

4.3 Results

First, a qualitative evaluation of the performance of the algorithm in the 50 sample cases can be gathered by comparing the plots of the coefficients describing Σ_1 versus the opposite of those describing the AO surface Σ_2 at the end of the estimation procedure. In Figure 4.6, the comparison plots for the six coefficients are shown: the estimates lay around the identity lines, even if the estimation worsens for astigmatism and defocus. Three indices are then used to evaluate the performance of the algorithm.

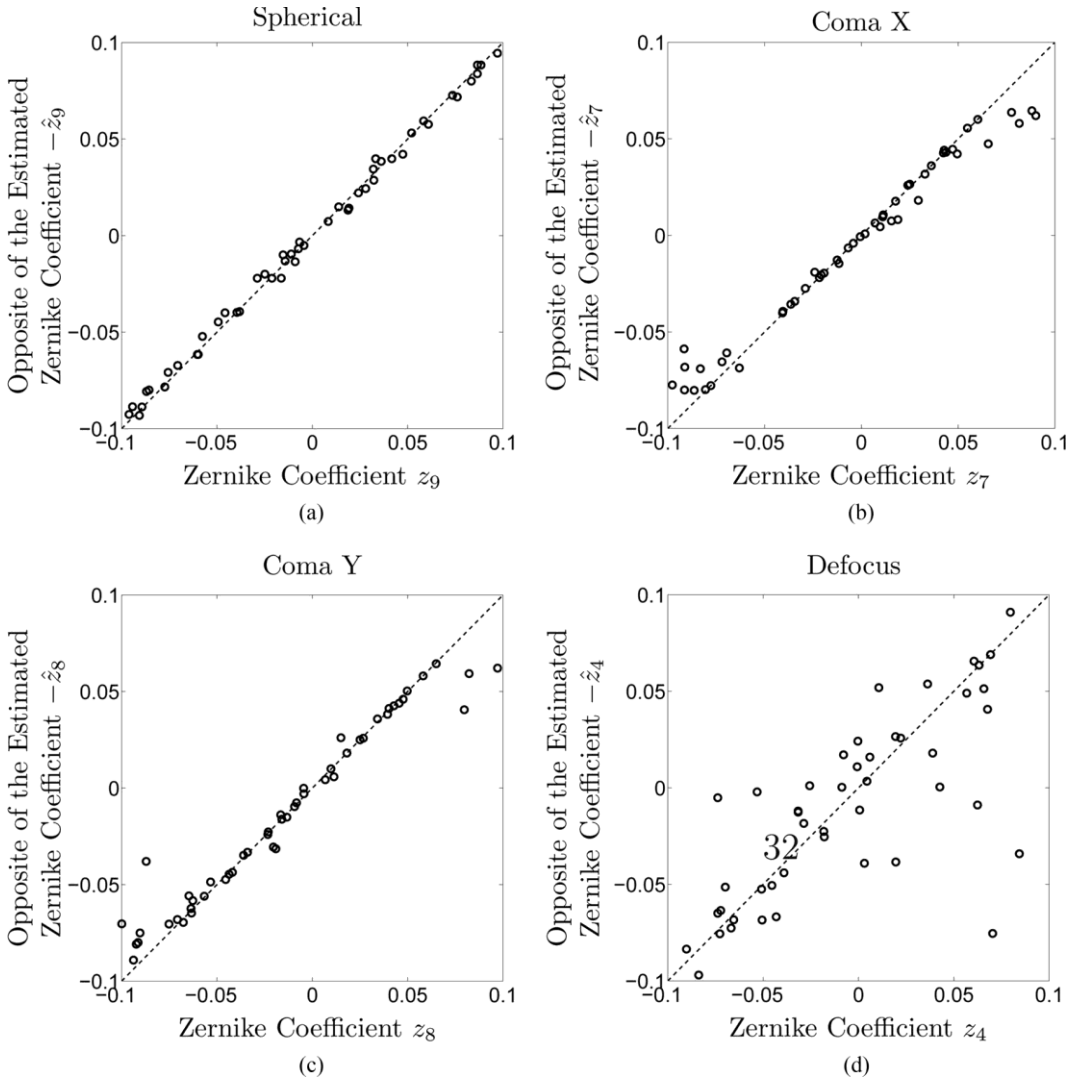


Figure 4.6 Comparison plots of the Zernike coefficients of the fixed surface Σ_1 versus the estimated coefficient describing the surface Σ_2. In Figure 4.7(a) the plot for the z_9 coefficient is represented, Figure 4.7(b) for the z_7 coefficient, Figure 4.7(c) for the z_8 coefficient, Figure 4.7(d) for the z_4 coefficient, Figure 4.7(e) for the z_6 coefficient, and finally Figure 4.7(f) for the z_5 coefficient.

The first index is the absolute sum between the six estimated Zernike coefficients $\hat{z}_i \in Z_{\Sigma_2}$ used to compensate the optical aberrations and those $z_i \in Z_{\Sigma_1}$ of the aberrating surface Σ_1. Since a perfect compensation of the aberrations is achieved when the two surfaces Σ_1 and Σ_2 are complementary, the estimated coefficient Z_{Σ_2} should have a value opposite that of the coefficient Z_{Σ_1}. The absolute estimation error of the i-*th* Zernike coefficient is thus

$$\varepsilon_1 = |z_i + \hat{z}_i| \tag{4.16}$$

This shows the capability of the system to accurately describe the unknown aberrations. The median values, along with their standard deviations, are reported in

Table 4.1, whereas in Table 4.2 the same values obtained estimating the coefficients with the direct maximization are reported.

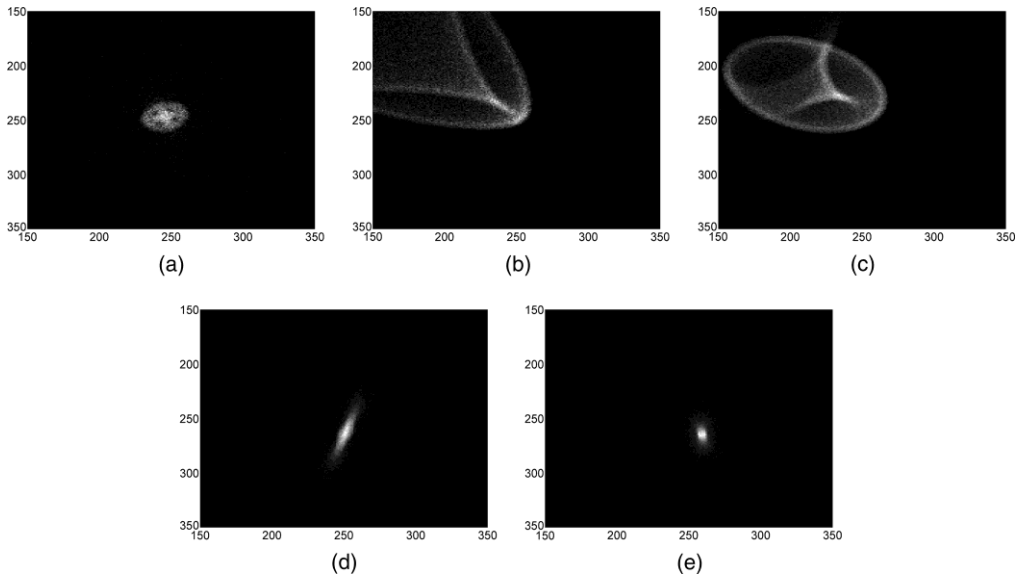


Figure 4.7 Progressive aberration estimation and correction. The *xy* plot scale is the same for all the images, however the color map is different, so that each image is normalized to its maximum intensity to visualize the point source shape. (a) Original aberrated point image. Maximum intensity is 2×10^{-4}, and the function f(c) described in [30] is 0.19. (b) Aberrated point image after spherical correction. Maximum intensity is 5×10^{-4}, and the function f(c) described in [30] is 0.99. (c) Aberrated point image after coma correction. Maximum intensity is 6×10^{-4}, and the function f(c) described in [30] is 0.98. (d) Aberrated point image after defocus correction. Maximum intensity is 16×10^{-4}, and the function f(c) described in [30] is 0.90. (e) Aberrated point image after astigmatism correction. Maximum intensity is 16×10^{-4}, and the function f(c) described in [30] is 0.90.

Additionally, in Figure 4.8 the distributions of the estimation errors $e_i = z_i + \hat{z}_i$ are shown for each Zernike coefficient separately, and in Figure 4.9, the distribution of the estimation errors obtained with the direct maximization procedure are shown. At variance with the proposed algorithm, it is clear how the error distributions are similar for all coefficients, but the variances of the error are greater than those provided by the proposed method.

	ε_4	ε_5	ε_6	ε_7	ε_8	ε_9
median	0.0127	0.0232	0.0209	0.0097	0.0091	0.0029
standard deviation	0.0300	0.0222	0.0398	0.0143	0.0149	0.0018

Table 4.1 Absolute error on the estimates of the Zernike coefficients of the aberrating surface

	ε_4	ε_5	ε_6	ε_7	ε_8	ε_9
median	0.0514	0.0510	0.0485	0.0385	0.0409	0.0466
standard deviation	0.0288	0.0299	0.0309	0.0299	0.0326	0.0304

Table 4.2 Absolute error on the estimates of the Zernike coefficients of the aberrating surface obtained with the Direct Maximization method proposed in [30]

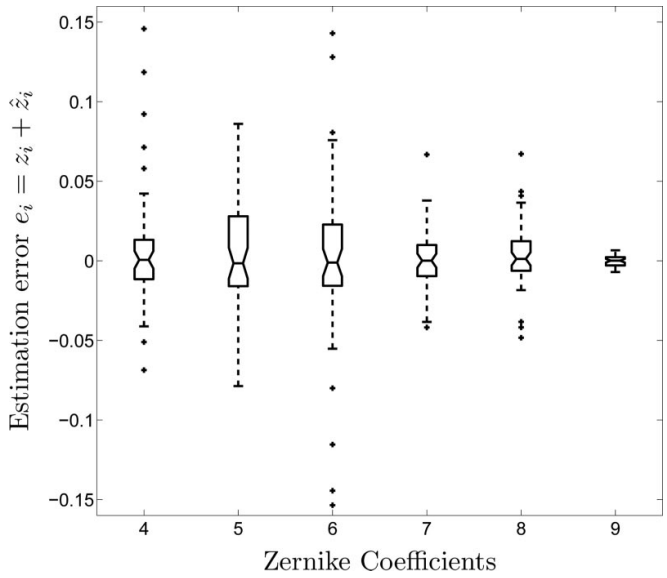


Figure 4.8 Error distribution in the estimation of the Zernike coefficients. Each box has lines at the lower quartile, median, and upper quartile values. The whiskers are lines extending to the most extreme value of the data inside 1.5 times the interquartile range. Outliers are data with values beyond the ends of the whiskers, and are plotted with a single cross.

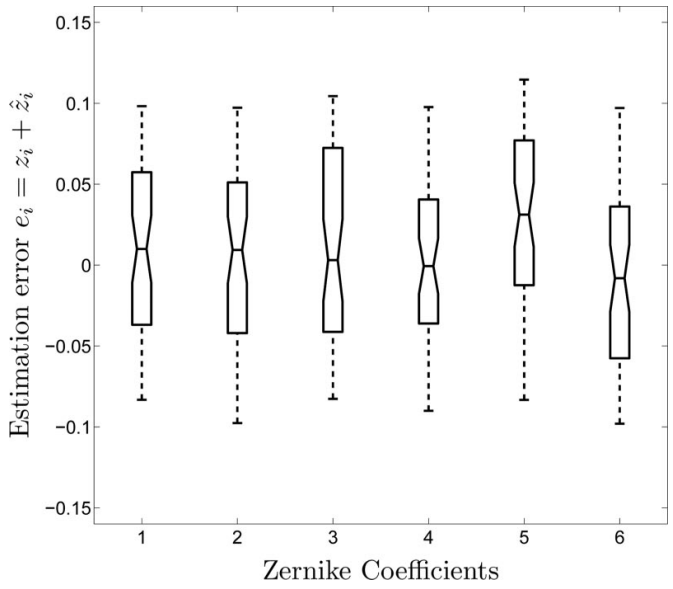


Figure 4.9 Error distribution in the estimation of the Zernike coefficients obtained with the direct maximization proposed in [30]. Each box has lines at the lower quartile, median, and upper quartile values. The whiskers are lines extending to the most extreme value of the data inside 1.5 times the interquartile range. Outliers are data with values beyond the ends of the whiskers, and are plotted with a single cross.

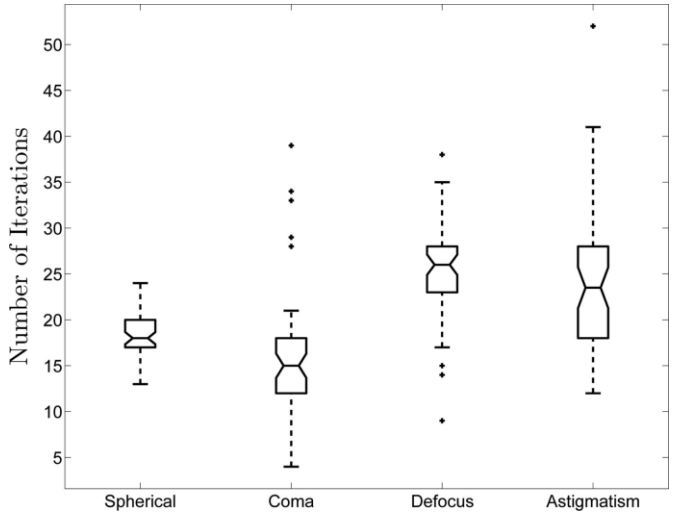


Figure 4.10 Number of iterations needed for the proposed algorithm to converge for each single type of aberration to be estimated. Each box has lines at the lower quartile, median, and upper quartile values. The whiskers are lines extending to the most extreme value of the data inside 1.5 times the interquartile range. Outliers are data with values beyond the ends of the whiskers, and are plotted with a single cross.

It is apparent from an analysis of both Table 4.1 and the figures that the estimation error increases in the coefficients that are estimated last. There are two reasons which explain this behavior of the algorithm. First, when estimating coefficients low in the hierarchy, residual errors in the already estimated coefficients can mislead the estimation procedure. Second, as the size of P_q decreases, the sensitivity of the objec-

tive functions used decreases, since the image resolution is not sufficient for reliable detection of the remaining aberrations.

The second index is the number of pixels $n_{3\,\mathrm{dB}}$ that are above the -3 dB threshold (half-maximum) with respect to the maximum power density value, at the end of the procedure. The optical system described in 4.2 provides a nominal non-aberrated and quantized image of S of 8×8 pixels. Hence, the closer the dimensions of the imaged point resulting at the end of the procedure are to the nominal ones, the better the compensation of the aberration. The average $n_{3\,\mathrm{dB}}$ side dimension of the resulting P_q is nine pixels with a standard deviation of 1, showing an excellent ability to reduce the spot size.

Finally, the third index is the number of iterations n_{it} required to achieve the convergence. This is a measure of the speed of the algorithm, in order to assess the possibility of using the proposed algorithm in a real system where convergence must be achieved in a few seconds: in our simulations, the number of iterations n_{it} required by the algorithm to converge has proved to be very limited, thus making viable an on-line implementation. The average n_{it} is 78 with a standard deviation of 14, for estimating the six Zernike coefficients considered, and the maximum number observed in the 50 repetitions of the experiment was 117: in Figure 4.10 the box-plots show the distribution of the number of iterations separately for each estimated coefficient, so that an idea of the convergence speed separately for each optimization can be gathered. The deterministic nature of the algorithm ensures that it will converge to the same estimate at each run, given the same starting conditions, at variance with stochastic algorithms widely used for this kind of optimization, as simulated annealing or genetic algorithms. Moreover, its gradient-based nature will ensure that it will quickly reach the nearest (local) optimum of the objective function without trying random coefficient configurations that lay far from the direction of objective function decrease.

In Figure 4.7 the progressive aberration correction operated by estimating the related Zernike coefficients is shown in a sample setting. Looking at the shapes of the different point images, it is easily understandable that a single cost function based on image quality metrics would never allow it to step from an image as that in Figure 4.7(a) to those in Figure 4.7(c) or Figure 4.7(b): from a purely imaging point of view, Figure 4.7(c) or Figure 4.7(b) appear as worsening of the first image Figure 4.7(a). In contrast, adapting a specific objective function for each aberration allows it to overcome this limitation, achieving a better aberration compensation and a smaller spot size.

4.4 Conclusions

The described method does not need either wavefront sensor or the knowledge or computation of the PSF of the system. It only requires the acquisition of images of a

point source while the aberrations are corrected; it relies on image analysis and on the identification of a specific objective function to be optimized for each Zernike coefficient considered. A strategy for reducing the dimensionality of the state space of the coefficients has been devised, which together with the deterministic, gradient-like optimization procedure has proved to require very few iterations to converge, and to be able to estimate the Zernike coefficients of the real aberrations with appreciable accuracy. After the simulation test reported in this chapter, the software has been tested on a test bench with real optics, as described in the next chapter of this thesis.

Chapter 5

The Adaptive Optic System: Fundus Camera Prototype

This Chapter concentrates on description of a fundus camera with an adaptive optics (AO) system with no wavefront sensor to correct primary aberrations is presented. This system is based on the closed loop software described in the previous chapter. It iteratively analyzes a point source target image on the instrument focal plane and suitably modifies the AO device.

Although the tests carried out with a pull-only deformable mirror (DM) have shown that the system reaches an optimal focusing condition in a few seconds, the acquisition of artificial retinal fundi has shown poor performance. Because of the poor S/N ratio of the acquired target image, a variety of modifications have been introduced in the optical path, none of which, however, has led to comforting results. The incapability of the system to deal with the low physiologic reflectance of the human retina (4%), together with the intrinsic loss of intensity due to its peculiar optical path, strongly discourage the usability of the system for clinical purposes. The most promising improvement to be taken into consideration will consist in redesigning the optical path for the near infrared spectrum.

5.1 Introduction

Minimization of wavefront (w-f) aberrations is an obvious and fundamental goal in the design of any optical system. A great deal of attention has historically been devoted to the subject, confirming the great interest and importance it has.

Until a few years ago however, rarely were problems related to the minimization of "time-dependent" optical aberrations at the center of major studies. This was mainly due to the fact that normal optical systems operate either in a static, or extremely slow varying, environment, or in a situation in which time variations can be considered negligible. In all these cases, "rigid" optical elements, i.e. optical elements whose optomechanical parameters – such as refractive index and shape – are not time-dependent, can be used. When necessary, simple mechanisms can be adopted to either change the relative position of one or more optical elements (as is the case with many camera objectives), or to slightly modify the shape and curvature of an optical

element (as actually happens with deformable mirrors (DM) in astronomy active optics) in order to maintain the focus of the system.

In the last few years however, interest has increased also as regards the realization of what we may call "dynamic" optical systems: in this case, not only does the optical environment in which the system has to work varies rather quickly with time, but mainly it varies in an unknown way. For this class of optical systems, mechanisms slowly changing the optical parameter in a predefined way are not useful, and adaptive optics (AO) with a closed loop control system has to be implemented.

The most noticeable application of closed loop correction by means of AO in dynamic systems is the acquisition of astronomy-related images through the use of ground-based telescopes [38]. In this case, in order to remove the star twinkling due to time-dependent local variations of the atmospheric density in the air column above the telescope, the w-f of the observed object is acquired and analyzed by a suitable w-f sensor, as for instance a Shack–Hartmann device, by means of dedicated algorithms [39]. Then, the precise information about the w-f distortion is suitably passed to an AO, as a fast DM that changes its shape to compensate for these rapidly time-dependent aberrations.

Many other optical applications are now making use of AO systems: for example, AO has been employed to enhance the performance of free space optical communications systems [40], [41], and it is becoming very important for off-axis aberration correction in microscopy applications [42], [43]. In many cases, however, it is not really necessary to have fast and accurate systems as those used by astronomers, and simpler instruments can be realized. A typical case is instrumentation dedicated to ophthalmic investigation [44][24][32][26]. It is obvious that an AO system for this type of application has rather different requirements than one used by astronomers. On the one hand it can be a simpler instrument: although the eye changes the w-f continuously with relatively high frequencies ([45], [46]) in fact, rapid eye variations do not have a significant impact on image quality, since in many cases the interest is in the "average" w-f. It is therefore necessary to adapt the optical system only when changing the patient. On the other hand, a substantial difference that makes these instruments rather complex is that they also have to provide a suitable illumination to generate the w-f which has to be analyzed, since the object of interest is not a light source by itself. That of ophthalmic instrumentation is not an isolated case, and many other applications can be found in which the characteristics of an optical system need to be varied from run to run, with several minutes to hours time variations: this is the case of industrial instrumentation in a slowly varying environment [47], lab experiments [48][49][50], the alignment of optoelectronics devices [51]. In all these cases, there is not a real need to have a fast and continuous monitoring of the instrument's optical performance, with all the related complexity. For these typologies of application, it might be more convenient to have a simpler AO system, able to monitor only the slow variations of the w-f aberrations.

To this end, an instrument in which the w-f first order aberrations are estimated by a software code that analyzes the image produced by an *ad hoc* point-like source

was realized. As in a classical AO system, the information obtained by this software is then given as input to a DM that changes its shape to reduce the aberrations. The obvious advantage of this instrument if compared to a classical AO system is that the w-f sensor is no longer necessary; this reduces the cost of the instrument, and avoids the many problems related to maintaining the performance of such a device once installed and aligned. However, it also has the well-known limitation that with a simple image analysis it is not possible to obtain the entire and correct information about the aberrations present in the system. Actually, the realized instrument is not able to remove at once all the aberrations of the system, as an AO system with a w-f sensor can do; the system has been conceived to make a gradual reduction of the aberrations, by means of the iterative process described in the previous chapter of this thesis.

It must be mentioned that w-f sensorless AO systems are not a novelty, and several techniques have been developed that allow their use; generally, these systems are based on stochastic optimization procedures, such as genetic algorithms [42], [49], [52] or the simulated annealing one [32]. These methods however have the significant drawback of requiring either rather long computation, or many iterations before converging. This means that up to several minutes can be necessary before reaching the desired system optimization. The technique here described, instead, allows the instrument to correct the system aberrations in a straightforward manner; this strongly reduces the number of cycles, and consequently the time necessary to realize the system correction from minutes to a few seconds. More specifically, since the whole process usually requires less than a hundred iterations, working at a standard 25 frames/s rate implies that the whole process can be completed in 3–4 seconds or less, allowing it to work in *quasi*-real time.

The optical setup adopted to test this instrument is described in the following section: for these tests a prototype DM [53], having slightly less than a 12 mm useful diameter and a $\approx$ 10 μm maximum possible deformation (at the mirror center) has been used. The obtained results show that although the system has reduced the system aberration in a few seconds, the final images, acquired from an artificial retina, present both low contrast and low luminosity, impeding any automatic system from performing a reliable analysis.

It must be noted that the functioning of the mirror used is based on the deformation of a nitrocellulose aluminum coated membrane by means of local variations of the electrostatic pressure between the membrane itself and a pattern of electrodes underneath. Since with this DM the deformation of the membrane can be actuated only in one direction, the possible aberration corrections that can be performed are limited and often not sufficient to fully correct the system. To overcome this problem, the DM could have been set to half of its maximum deflection as a starting position [9]: this introduces some defocus that can be compensated by axially shifting a lens somewhere else in the optical path, but then the DM can be effectively moved in a push–pull way. However, to allow a wider range of the DM deflection, we preferred to avoid this solution and accepted some limitations to the tested system.

5.2 Software Concepts and Aberration Correction Strategy

The working principle at the basis of the designed instrument consists of analyzing the image of a known point-like source passing through the optical system under test, and modifying the DM shape according to the image analysis to reduce the image aberrations (see Figure 5.1).

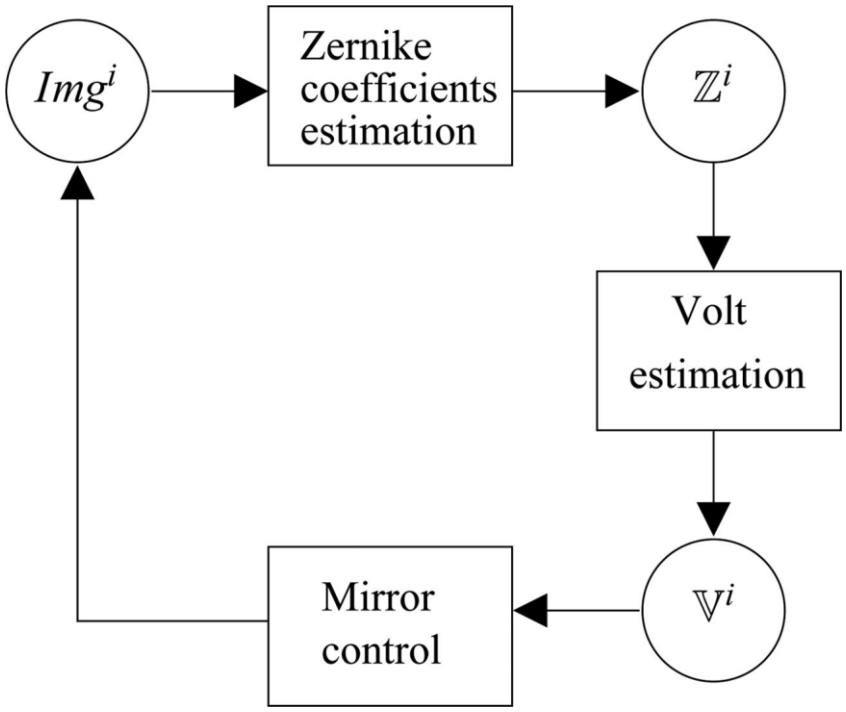


Figure 5.1 Block diagram of the software iterative procedure to minimize the aberrations in the optical system.

An illuminated pinhole has to be projected on the retina itself through a dedicated optical path. The light that is back-diffused by the retinal fundus acts as a point source, and its w-f can be analyzed to estimate the aberrations present along the optical path from the retina to the detector.

The aberration estimation is performed by the software described in the previous chapter, which analyzes a first image Img_0 produced by the point source with the DM in its "rest" condition, corresponding to a shape described by the Zernike coefficients $\{z_0, z_1, ..., z_n\} \equiv \mathbb{Z}^0$ (in the specific case, n = 6). The image is analyzed, and the possible presence of aberrations is evaluated, together with the direction of change of $\mathbb{Z}^0$, which is the vector of sign of the gradient $\nabla\mathbb{Z}^0$. Then the coefficients corresponding to the detected aberrations are changed, and the new $\nabla\mathbb{Z}^1$ vector is addressed to the DM electrodes voltage estimation routine to produce the mirror shape that best

approximates the one described by the estimated Zernike coefficients. The modification introduced by the mirror deformation gives rise to a new image Img_1, and the procedure is then iterated obtaining the sequence of images Img_0, Img_1, ..., Img_k, in which Img_k tends to be aberration free.

The described aberrations ranking and the iterative nature of the algorithm allows the progressive correction of all the aberrations, starting from those higher in the hierarchy and ending with the lowest: after the image Img_0, corresponding to the vector of Zernike coefficients $\mathbb{Z}^0$ is acquired, the spherical aberration is corrected by iteratively modifying the Zernike coefficients z_9 describing the shape of the DM, until no spherical aberration is detected; then the algorithm detects and corrects coma, defocus, and finally astigmatism. The implemented code, on the basis of the given inputs, then estimates also the $\{V_0^0, V_1^0, ..., V_m^0\} \equiv V^0$ array of voltages to be applied to the m electrodes of the DM [55], [56], [57].

It is worth noting that the closed-loop method of correcting the aberrations of an optical system which has been described above is very stable, at least with respect to possible misalignments of the DM or the aging of the mirror membrane. This stability is inherent in the adopted approach to the problem, where, unlike instruments using a w-f sensor, we are not going to measure the w-f aberrations. Less ambitiously, the goal of this method is to minimize the size of a reference target image in the detector focal plane: by obtaining this, the image quality of the optical system is optimal as well. It is also interesting to observe that in theory, if this AO system is working in an optical instrument, it is no longer necessary to realize a perfect alignment of the instrument itself, because any misalignment would be compensated by the DM.

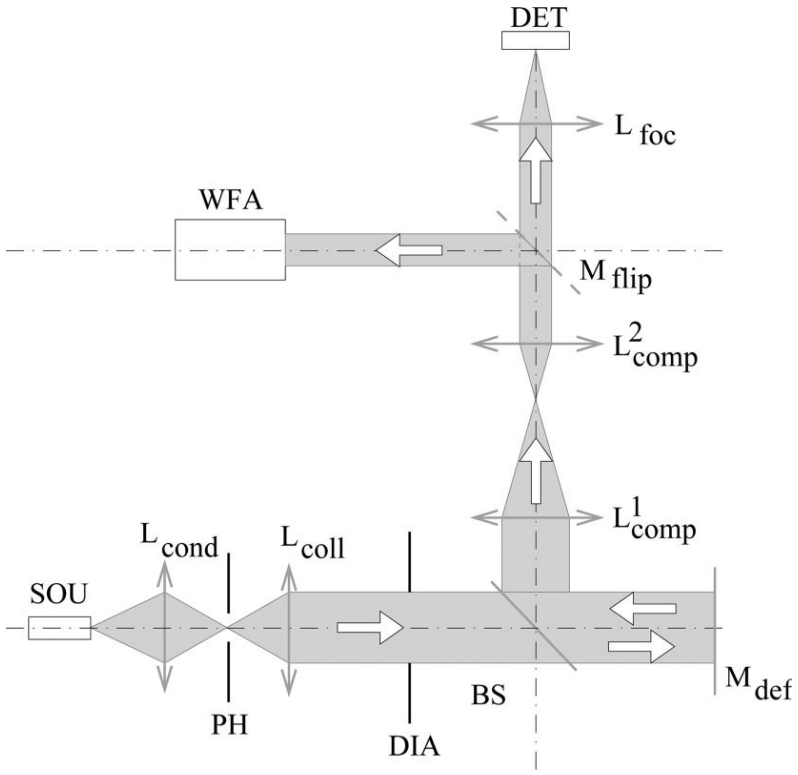


Figure 5.2 Schematic of the optical setup used in the tests of the AO system.

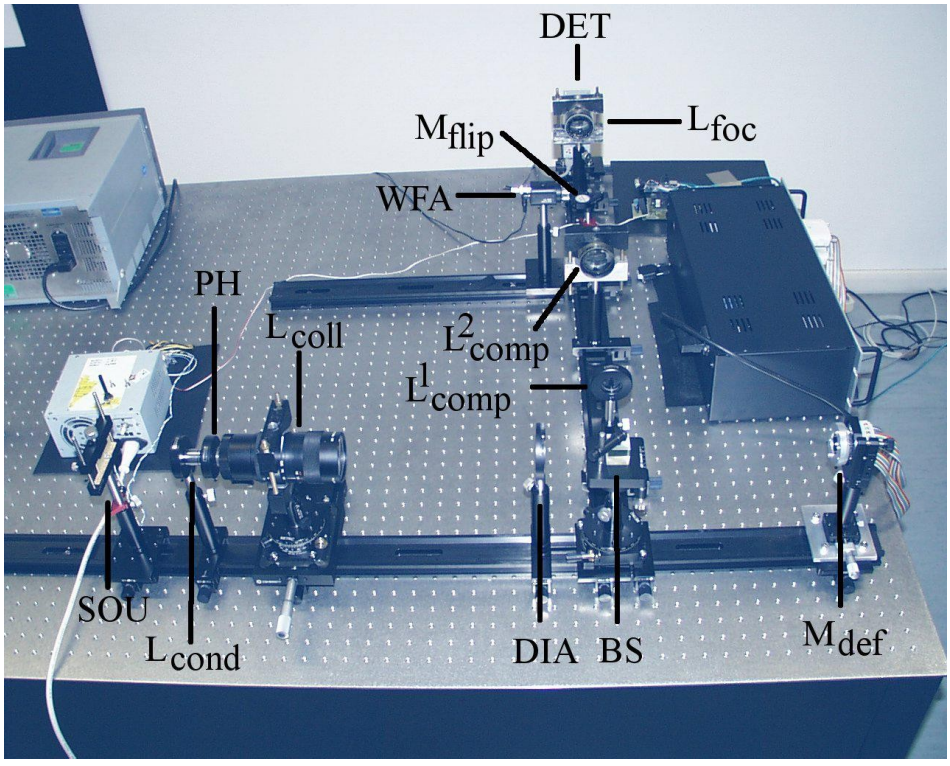


Figure 5.3 Picture of the optical setup used in the tests of the AO system.

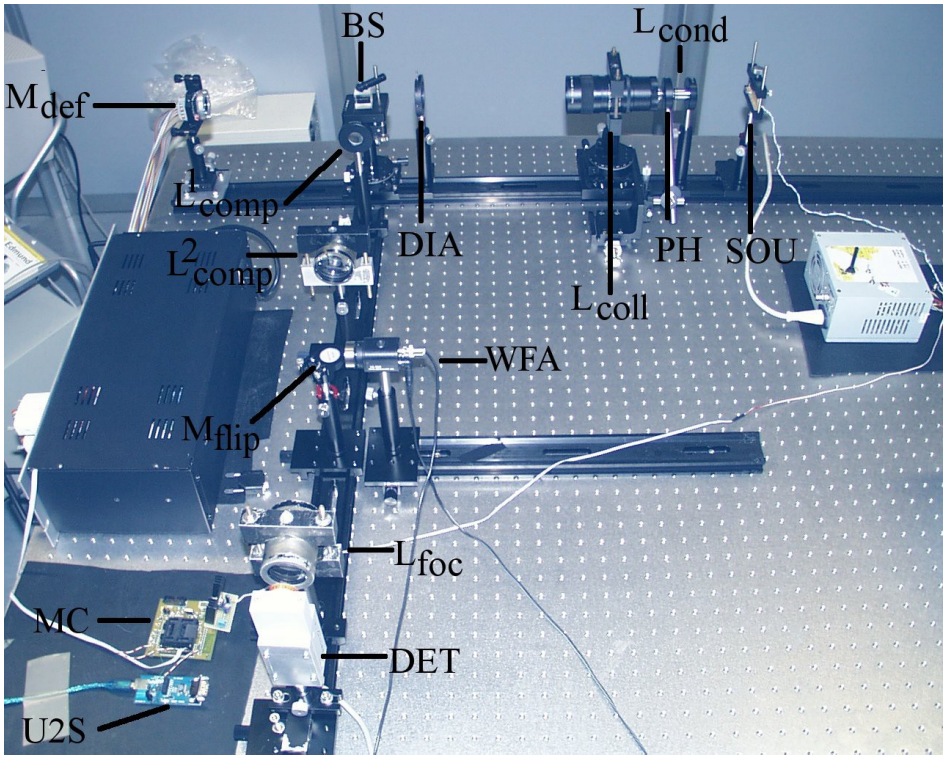


Figure 5.4 Another picture of the optical setup used in the tests of the AO system

5.3 Experimental Setup for the Test of the AO System

To check the performance of the AO system, a semplified optical test bed has been devised (Figure 5.2). In this test bed the 527.5 nm visible radiation emitted by a LED diode source (SOU) is condensed by a microscope objective lens L_{cond} on a 10 μm pinhole (PH). The radiation emerging from the pinhole is collected by zoom lens (L_{coll}) acting as a collimator; from an analysis of the zoom parameters, an effective focal length of 29.4 mm and an $f/2.6$ aperture have been estimated. The collimated beam is then spatially limited by a diaphragm (DIA) at an 11 mm diameter, which passes through a beam splitter (BS) and impinges normally on the DM M_{def}. After back reflection, the beam is 90° deviated by the BS, and then it is reduced approximately three times in diameter (bringing it from 11 to 4 mm) by an a-focal Newtonian system $L_{comp}{}^{1}$ and $L_{comp}{}^{2}$).

The collimated "compressed" beam can then follow two different paths. In the first case it is collected by a focusing two-lens system L_{foc} (effective focal length 47 mm) that makes the image of the pinhole on the detector (DET). The latter is the PL-A741 PixeLINK CMOS digital camera (pixel pitch of 6.7 μm), which transfers the data to a PC via a FireWire interface.

The whole optical system makes a ≈4.5 magnification of the pinhole, so that the nominal (aberration free) pinhole image diameter is of the order of 45 μm, corres-

ponding to approximately 7 pixels. In the second path, the collimated beam is deviated by a flip mirror M_{flip} and directly sent to an OKO Technologies Hartmann w-f analyzer (WFA). The latter, whose entrance aperture is ≅4 mm (which was driving the beam size reduction), has been used to measure the w-f aberrations before and after the correction performed by the DM, allowing an accurate check of the DM performance. The WFA w-f measurements are expressed in wavelength units, which we have calibrated assuming the source wavelength $\lambda = 527.5$ nm.

With this system, by varying the focal length of the zoom lens L_{coll} and tilting the $L_{comp}{}^{1}$ lens, it was possible to introduce controlled amounts of both defocus and astigmatism on the nominal pinhole image. Then, analyzing the acquired image and estimating the present aberrations, the voltages to be applied to the DM electrodes are calculated and the mirror is consequently deformed, closing the loop.

5.4 Wavefront Aberration Correction Results

Three cases have been considered to show the capability of this system to correct the w-f aberrations: case (A), in which defocus is the main aberration; case (B), where the main aberrations are astigmatism and coma; case (C) where both defocus and astigmatism are present in an almost comparable amount. In all these cases, the root mean square (RMS) of the introduced w-f aberration is of the order of 0.5 waves $\lambda/2$: this value has been selected to stay within the range of the possible DM corrections, which are presently limited by the possible membrane deformation of the used prototype DM. For each considered case, two plots showing the w-f before and after the correction are given in Figure 5.5. Moreover, to quantify the goodness of the introduced correction, Figure 5.6 shows in a graphic way the Zernike coefficient values before and after the correction. In these figures also the w-f peak-to-valley (P-t-V) and RMS values are given.

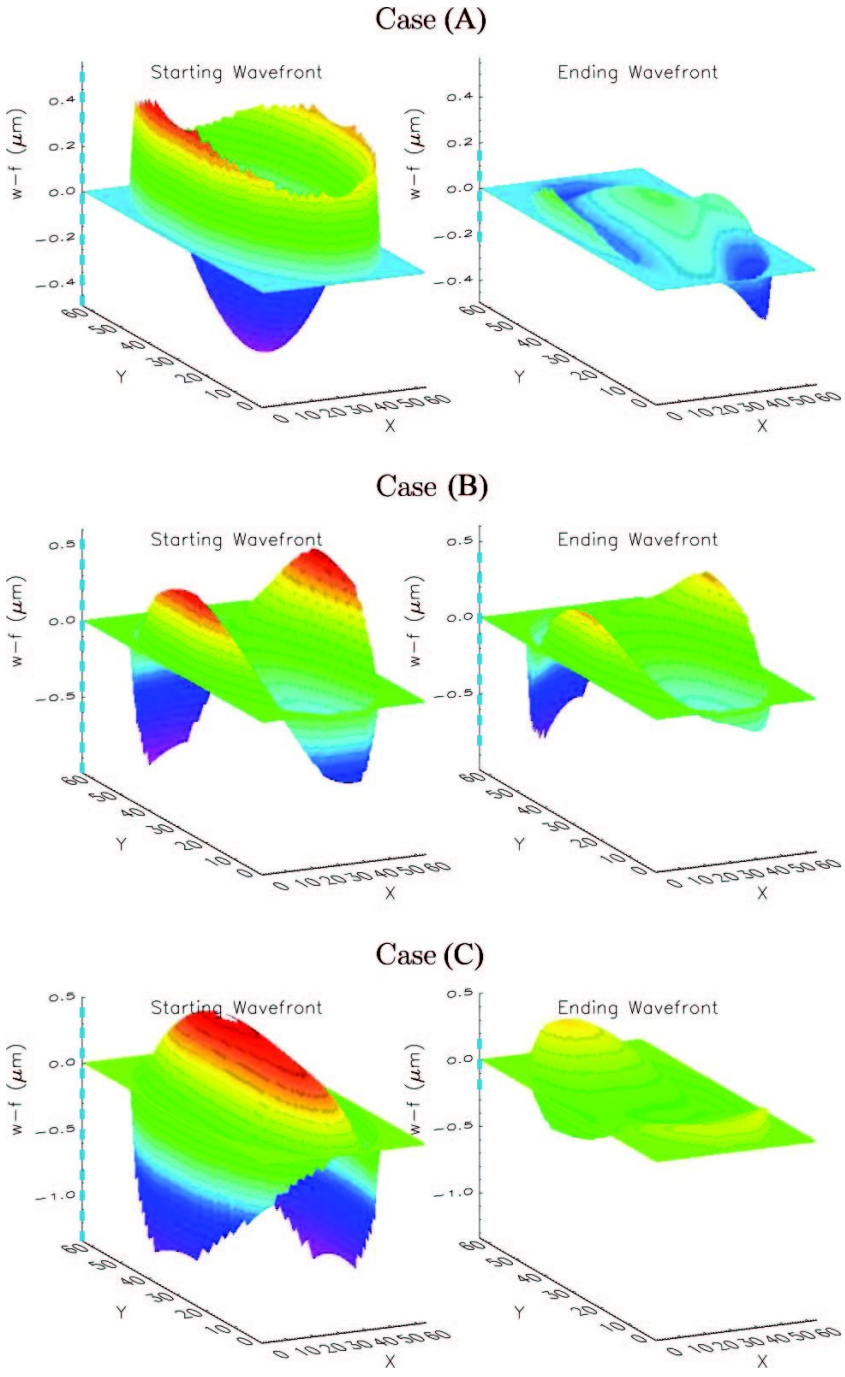


Figure 5.5 Wavefront surfaces (obtained with the WFA) before and after the DM correction for the three considered cases. The blue dashed lines overplotted to the z axis represent the total w-f excursion.

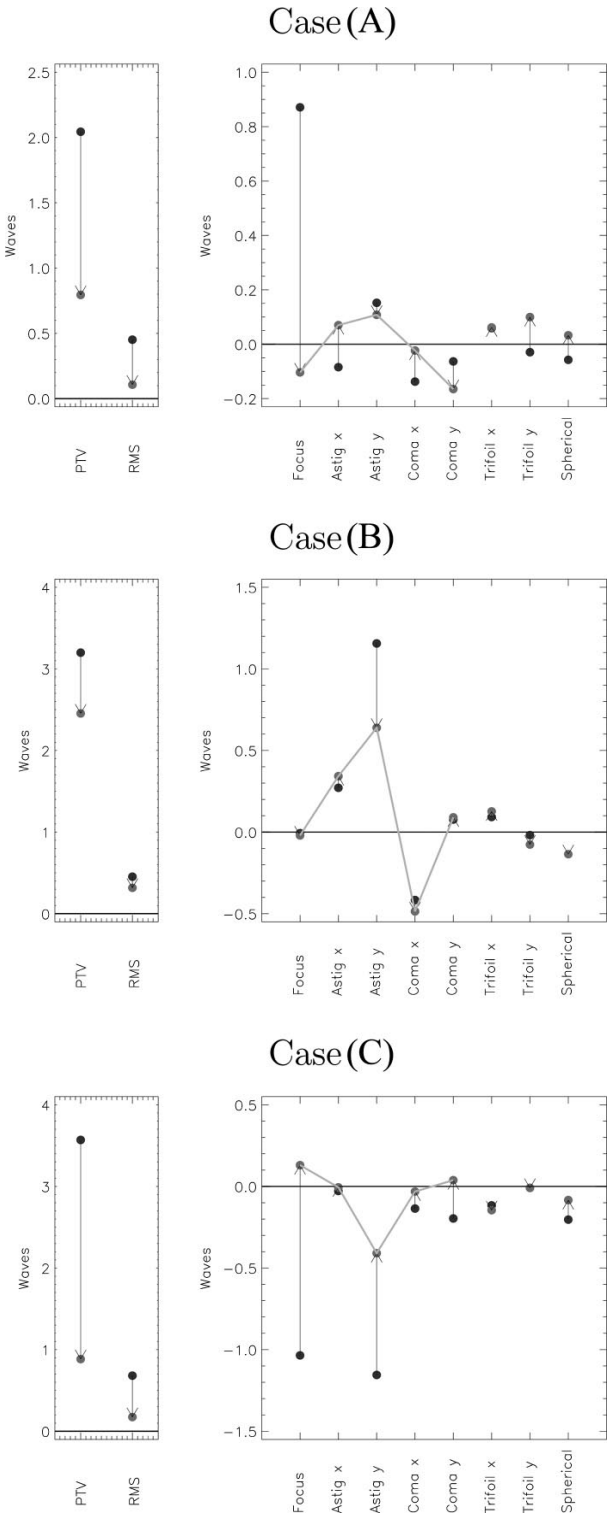


Figure 5.6 Zernike coefficient values before and after the correction for the three considered cases. Dark points represent the aberrations before the correction; the gray ones are representative of the corrected w-f. In addition, the surface P-t-V and RMS values are reported (with the same color meaning). A gray line joins the three main aberrations (defocus, astigmatism, coma); this line, in case of ideal correction, would coincide with the dark continuous one.

Some considerations can be made on the obtained results: Case (A) is dominated by a defocus aberration "positively" oriented (i.e. with a positive value of the defocus aberration coefficient), which is the way in which the pulling action of the electrodes on the DM membrane is effective in reducing the aberration; no other significant aberration is present. Looking at the quasi-optimal w-f shape after the DM action, it is evident that the aberration correction performed by the system was good. To quantify this performance, we can note that the P-t-V has decreased to 40% of its initial value (but looking at the w-f plot, it is evident that the P-t-V value would be much lower if a local problem at the edge of the w-f was not present), that the w-f RMS value is now λ/10 (@527.5nm), and that the defocus coefficient has been reduced by almost 90%—without considering the sign of the Zernike coefficient. This result shows that the system is effective in identifying and correcting this aberration.

Case (B) has no defocus, but a significative "positive" astigmatism (mainly the C[2, -2] coefficient) coupled to coma (C[3, 1] coefficient). It is evident from the saddle w-f shape that to optimally correct these aberrations the pull-only action of the mirror membrane is not sufficient; in this case a proper correction cannot be expected. In fact, the obtained results show that the system has actually performed some correction, at least within the limits of the possible membrane deformation, but not sufficient to reach an optimal level. In particular, the P-t-V has been reduced by ~25%, the astigmatism y coefficient has been halved, and the RMS w-f value has been decreased to 0.3 waves (λ/3 @527.5 nm); all the other optical coefficients have not been varied in a significant way. Again, this is not an optimal result, but the actual limit can be related to the present DM design, not to the implemented method: with a push-pull DM, the result could have definitely been much better.

Finally, case (C) shows a peculiar and rather interesting behavior. In this case, the w-f has strong defocus and astigmatism (C[2, -2] coefficient), while all the other primary aberrations are much smaller. Since the defocus has a negative coefficient, owing to the DM pull-only limitation one could expect that the system is not able to correct it. However, in this case, the w-f does not have a marked saddle shape, as in the previous case, and some corrective action can be done by the DM (looking at the w-f shape in Figure 5.5, we may think that the DM is able to "pull up" the "lower" sides of the w-f). In effect, the obtained final w-f shows that the algorithm for the analysis of the pinhole image has been able to minimize the aberrations. The result is a considerable reduction to 25% of the P-t-V and a w-f RMS reduction to (λ/6 @527.5 nm), with a great decrease in all the aberration coefficients.

Three other general considerations can be made.

The first is that looking at Figure 5.5 at the w-fs before and after the DM correction, it is clear that the DM is acting very well within its physical limitations.

The second is that in all the presented cases the Zernike coefficients not involved in the correction process have not been sensitively modified. This permits to state that the introduced correction is obtained without degradation or perturbation of the uncontrolled Zernike coefficients, so it confirms the goodness of the implemented algorithm for the aberration estimation by a pinhole image analysis.

The final consideration is relative to the speed of the system. In all the tested cases, the algorithm takes less than 100 cycles to reach the "optimal" condition; since one cycle takes approximately 1/20–1/25 s, the whole optimization takes just 4–5 s. If this time is compared with the time which is generally necessary to optimize other sensorless AO systems, the improvement introduced by this technique becomes evident.

5.5 Experimental Setup for the Retinal Fundus Acquisition

In order to test the capability of the system to acquire images of real retinal fundus, in our laboratories we built a prototype of fundus camera, composed by the integration of the apparatus described in Sec. 5.3 and the framework of the commercial fundus camera MP-1 Nidek Technologies®, which we regarded as the main reference model.

The device functionality can be reassumed by its three different components: an illumination system, an imaging system, and the system of projection of the reference pattern for the aberration estimation.

The first system provides the uniform illumination of the retinal fundus for an area that corresponds to a FoV of 50°. This is realized by projecting a beam of polychromatic light, provided by a halogen lamp, through the pupil of the patient. The second system gathers the radiation back-reflected by the retina and then focalizes it on a high-resolution digital camera. In order to compensate the aberrations introduced by the patient's eye the AO system has been integrated along this last optical path. The third system, which provides the projection of the reference pattern for the determination of the aberrations, shares in great measure the optical path of the imaging system. It consists in a 527.5 nm visible radiation LED diode source that projects, through the imaging optical path, the pattern on the retinal fundus. The back-reflected radiation retraces the imaging optical path until an opportunely positioned splitter extracts it and sends it to a dedicated detector.

The complete integrated system has been tested on artificial eyes, whose reflectance (4%) mimes the human retina one.

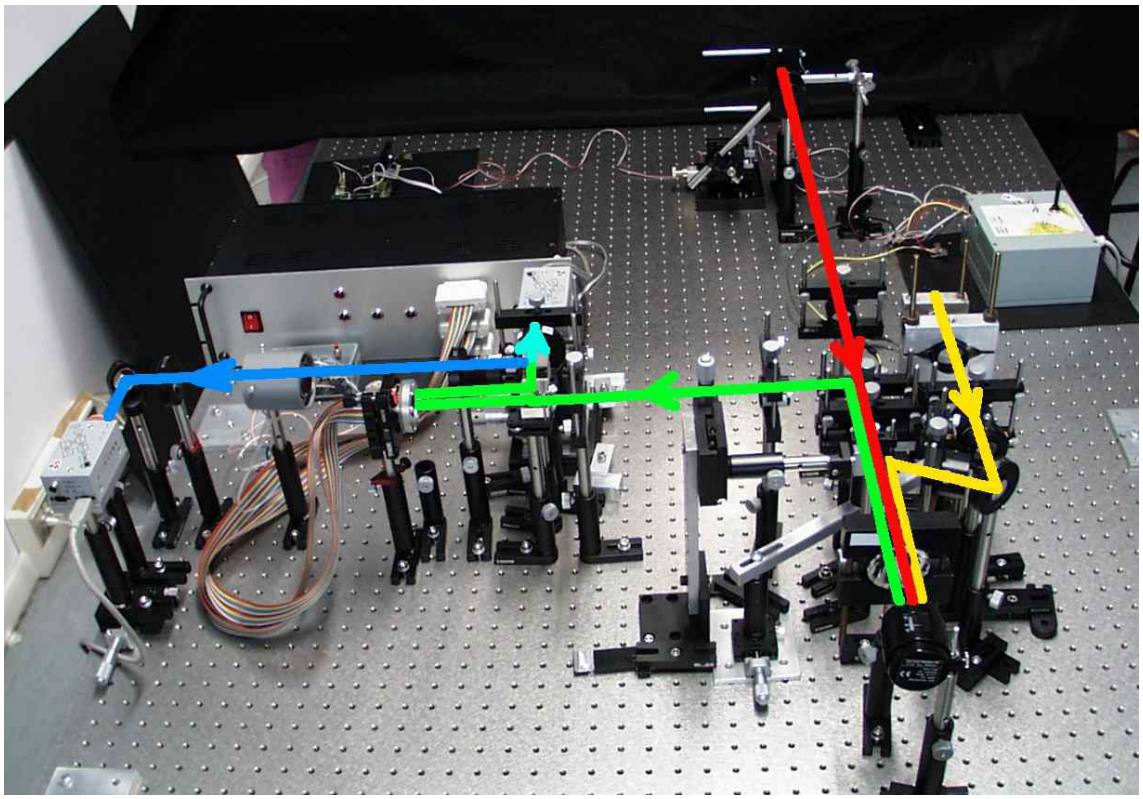


Figure 5.7 Picture of the AO fundus camera system built for the experimental setup; yellow - illumination path; red - path for the projection of the reference pattern; green - imaging path leading to the DM; pale blue - path of the split beam sent to the aberration detector; blue - path of the split beam sent to the imaging system.

Extreme attention has been devoted to the respect of the current security normative on the ocular radiometry, with the aim of ensuring with complete certainty that the system could not endanger the patient's eye.

The system required at least 5 seconds before completing the compensation of the aberration complete. Ideally, for all the duration of the procedure the patient should not blink, nor move, as the process of compensation would diverge in the attempt to compensate a false signal. For that reason the intensity of the pattern projection beam was set low enough to increase the patient's comfort.

When the aberration compensation finishes, the illumination system provides the flash, which is gathered by the imaging system and brought to the HR digital camera. Although the intensity of the flash has been opportunely calibrated for security reasons, the tests made it quite evident that it would be impossible, for an average patient, not to close his/her eyes immediately after the beam emission.

5.6 Artificial Retinal Fundus Acquisition Results

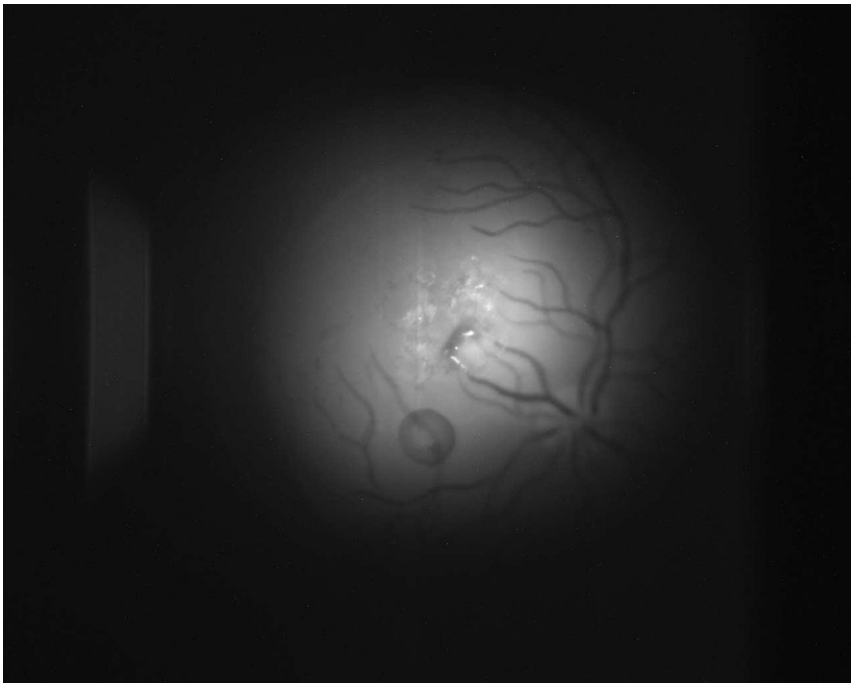


Figure 5.8 Example of picture acquired from the artificial fundi with the AO fundus camera prototype.

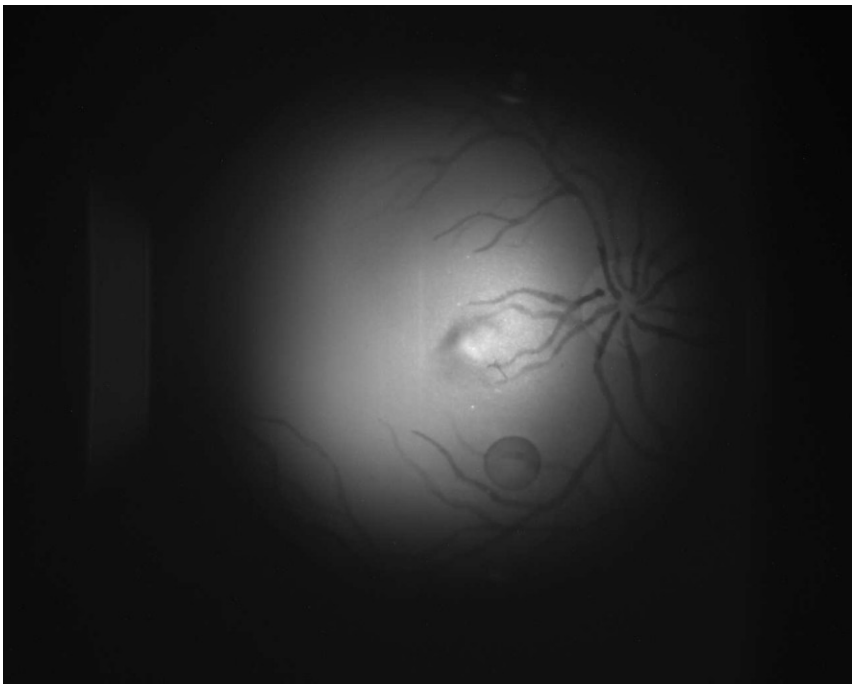


Figure 5.9 Another example of picture acquired from the artificial fundi with the AO fundus camera prototype.

While the images of the artificial fundus acquired by the prototype appear to be quite well focused, they exhibit both inadequate illumination and some acquisition artifacts. The major appreciable defect is the strong loss of luminance from the inner to the outer region of the images and the consequently low contrast between vessels and background, which hamper any attempt to characterize the morphology of the vessel network. The artificial fundi used for the acquisition test do not present any sort of non-vascular features typical of the real retina. Although no test has been lead on a real fundus, it is hypotizable that the addition of the non-vascular features would further decrease the discriminability among retinal objects in the acquired image. On the left of the images (see Figure 5.3 and Figure 5.4) an artifact due to some reflex introduced by the ambient can be seen.

Many attempts have been implemented to solve those problems. In order to minimize the loss of intensity along the optical paths and reduce the number of spurious reflexes sneaked in, a number of different configurations for the optical paths have been tried, trying to decrease the number of reflecting surfaces and splitters as much as possible (3 in the most recent version). Each of the lasts, in fact, is responsible for a 50% loss of intensity of each of the two beams it provides. One of the most recent additions has been the addition of an intensifier at the end of the imaging system, which has been introduced with the aim of increasing the signal-to-noise ration. However, because of the number of spurious reflexes gathered by the device from the environment, this amplifying approach has brought to the only result of an increased background noise in the final image. In addition, it must be noticed that we are not using a low-noise camera, and some time-consuming image filtering is necessary (since the signal-to-noise ratio is very poor) to remove undesired features from the image.

A number of attempts that had been planned in a first moment will not be realized because of the lack of promising evidences; the brief list that follows is aimed at describing some of them. A polarized beam of light could be used for the projection of the reference pattern in the retina. Then, the separation of the two variety of light (polarized and not polarized) would not require the employing of splitters. However, the measure of depolarization caused by the transit of the light through the eye is not known. Still, the projection of an ultraviolet pattern has been taken into consideration at first, and then discarded as the intensity at which this spectrum becomes harmful to the retina is way too much feeble to be useful for any acquisition process.

The most promising improvement that could be taken into consideration consists in using a near infrared pattern projector, which would require a complete redesign of the optical paths for the proper management of the two different spectra.

5.7 Conclusions

The description of an AO system for the acquisition of retinal fundus with no w-f sensor to correct primary aberrations has been given. The system is based on an

iterative process that analyzes a point source target image, acquires some information on the aberrations present and consequently changes the shape of a DM to minimize them.

The system performance have been assessed with a two-stage experiment: first, a simple optic framework has been devised in order to test the capability of the AO device to compensate the unknown aberrations introduced by the optical system under testing; secondly, the first framework has been integrated with the optical scheme of a commercial fundus camera in order to prove the usability of the device to acquire real fundus images.

The tests with the pull-only deformable mirror (DM) have shown that the system reaches an optimal focusing condition in a few seconds, while the acquisition of artificial retinal fundi has revealed discouraging performances.

Having considered the poor S/N ratio of the acquired target image, a variety of modifications have been introduced in the optical path, all of them, however, exhibiting no comforting results. The incapability of the system to reach useful signal-to-noise ratio is undermined by the low physiologic reflectance of the human retina and the intrinsic characteristic of the developed optical path to leak out light intensity. These results strongly discourage the usability of the system for clinical purposes. The most promising improvement to be taken into consideration will consist in redesigning the optical path for the near infrared spectrum.

Such a system can perhaps be applied in fields in which a real-time optical adaptation is not necessary. For the aim of this thesis, the current prototype has proved to be of no use in providing fundus images that can be suitably analyzed by the developed software.

Chapter 6

Collected Datasets

This chapter provides a description of the features and the provenience of the datasets used to train and test the developed software for the automatic analysis of the retinal fundus.

Since the current fundus camera prototype was not able to provide processable fundus images, we opted for creating a usable database of images combining a number of datasets which have been kindly shared in the Internet by researchers in the field of ophthalmology with sets of images we have gathered thanks to the collaboration our group has with clinical centers.

6.1 The DRIVE Dataset

The photographs for the DRIVE database [58], [59] were obtained from a diabetic retinopathy screening program carried out in The Netherlands. The images were acquired using a Canon CR5 non-mydriatic 3CCD camera with a 45° field of view (FOV). Each image was captured using 8 bits per color plane at 768 by 584 pixels. The FOV of each image is circular with a diameter of approximately 540 pixels.

The set of 40 images has been divided into a training and a test set, both containing 20 images. The authors made available a single manual segmentation of the vasculature for the training images, and two manual segmentations for the test case. As far as the two testing manual segmentations are concerned, the authors suggest using one as gold standard, while the other can be used to compare computer-generated segmentations with those of an independent human observer. All human observers that manually segmented the vasculature were instructed and trained by an experienced ophthalmologist. They were asked to mark all pixels of which they were at least 70% certain that they were vessel.

Thanks to the DRIVE database made publicly available to download at http://www.isi.uu.nl/Research/Databases/DRIVE/, we could evaluate the performances of our vessel tracking algorithm (See Sec. 7.4 Chapter 7and Sec. 8.4).

6.2 The STARE Dataset

The STARE dataset [60] consists of twenty retinal fundus slides. The slides were captured by a TopCon TVR-50 fundus camera at 35° field of view. Each slide was digitalized to produce a 605x700 pixel image, 24-bits per pixel (standard RGB). Ten images are from patients with no pathology (normal). Ten images contain pathologies that obscure or confuses the blood vessel appearance in varying portions of the images (abnormal). The authors explained that this selection was made for three reasons. First, most of the referenced methods had only been demonstrated upon normal vessel appearances, which are easy to discern. Second, some level of success with non-normal vessel appearances must be established to recommend clinical usage. Third, they desired to evaluate the performance differences (if any) of the algorithms on normal and abnormal case.

Two human observers carefully labeled by hand each of these twenty images, to produce ground truth vessel segmentation and a second observer's reference. We used the STARE dataset to evaluate the performance of the vessel tracking algorithm proposed in this thesis. The STARE dataset can be downloaded from the web page http://www.ces.clemson.edu/~ahoover/stare/.

6.3 University of Wisconsin Dataset

Twenty 30° color retinal images acquired during the DCCT study [61] and eighteen acquired during the ETDRS study [62] were made available by the Department of Ophthalmology and Visual Sciences, University of Wisconsin, USA (from now on, called the "UoW dataset"). The images were saved in digital format, with a resolution of 3.7 μm/pixel, resulting in 2346x2652 pixel images for the DCCT dataset and 2983x2344 pixel images for the ETDRS dataset.

Unlike the two previously mentioned datasets, this one is not accompanied by a manual segmentation of the retinal structure. For each image, instead, expert clinicians have provided the AVR parameters as far as the ETDRS set is concerned, and the AVR, CRAE, and CRVE parameters as far as the DCCT set is concerned.

We used the data kindly provided data by the University of Wisconsin to assess the capability of our software, paired with the one proposed in [63], to accurately and reproducibly describe the above mentioned clinical parameters, by means of a correlation comparison with the measures obtained by trained and proved personnel.

6.4 Moorfields Eye Hospital Dataset

The Moorfields Eye Hospital of London supplied a set of 19 TIFF images (3008x2000 pixels) and 7 JPEG images (1536x1024), all acquired with a Topcon Retinal Camera TRC-50IX. A clinical evaluation of the global tortuosity, accurately estimated by an expert ophthalmologist, has been provided for each image of the set. This evaluation envisages three levels of tortuosity and, specifically for the level "2", three degrees of severity, namely "low", "medium", and "high" degree.

We used this dataset (from now on, the "MEH dataset") and the clinical evaluation to validate the capability of our software in discriminating the different degrees of tortuosity of the vessel network.

6.5 DB60, Yet Another Homemade Dataset

The images used to build this dataset are acquired following the protocol described in Chapter 3. The photographs were taken at the Ophthalmology Clinics of the Universities of Padova, Udine and Trieste by experienced technicians.

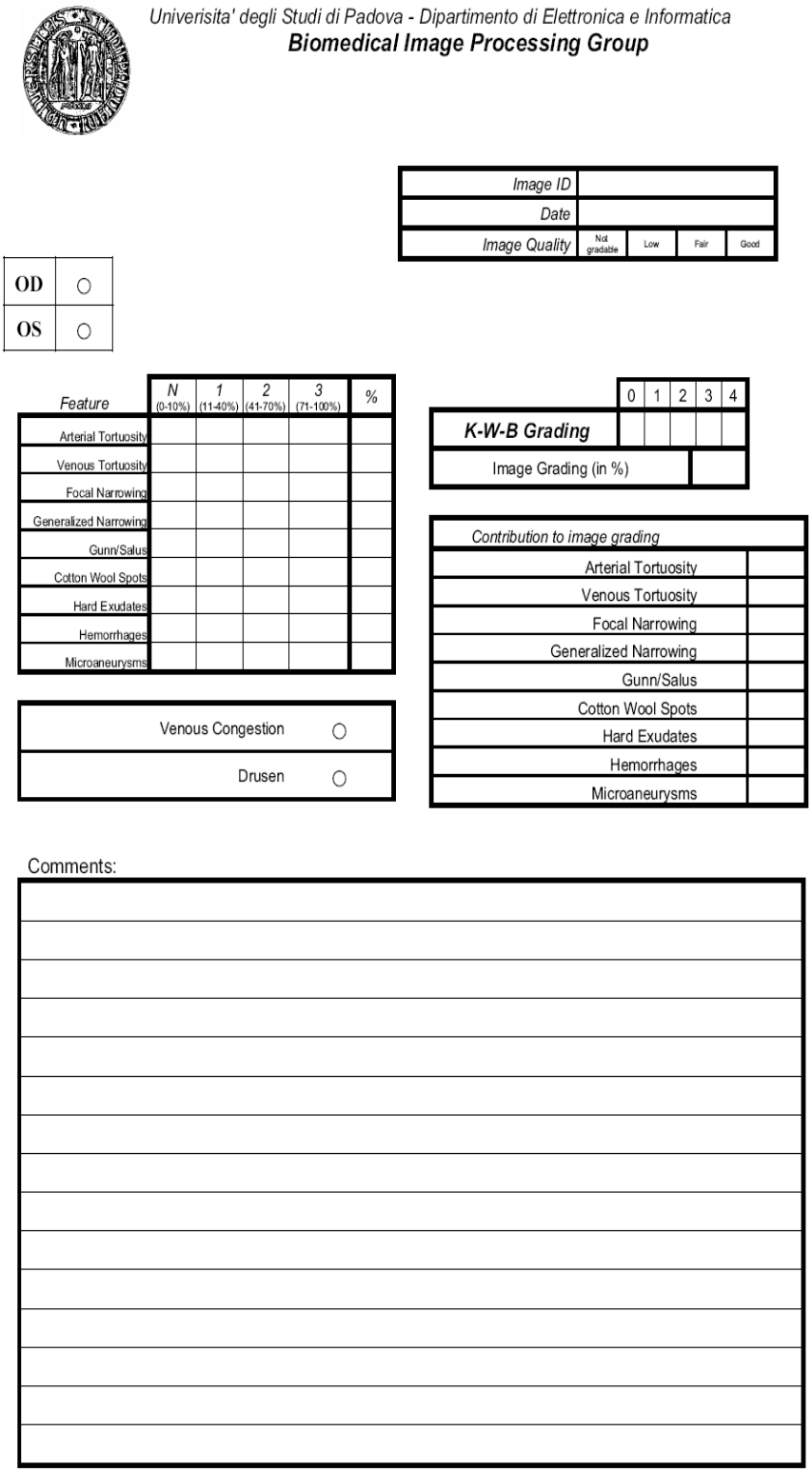
The films were subsequently sent to the Department of Information Engineering of the University of Padova, where they were digitized at 1360 dpi, 24 bits per pixel, using a Canon scanner. 1444 retinal images of various quality and retinopathy level were digitalized, yielding images of the approximate size of 1400x1200 pixels. An expert ophthalmologist chose 60 images creating what will be called the DB60.

6.5.1 Image Collection

To provide a ground truth evaluation of the images chosen in the DB60, a standard report form has been set up, and it is shown in Figure 6.1 and Figure 6.2. The first page of the report contains all the information relevant in the evaluation of the retinopathy. The second page requires the ophthalmologist to sketch on the scheme the approximate position of individual lesions (crossing abnormalities, focal arteriolar narrowing, non-vascular lesions), on the scheme. The standard clinical evaluation for hypertensive retinopathy is the Keith- Wegener-Barker grading scheme [8], or that proposed by Scheie [9]. The single abnormality is evaluated usually as none, mild, moderate or severe. Such qualitative evaluations provide a very rough assessment of the pathology and of its constituting damages. In order to overcome this limitation, the ophthalmologist was required to fill in for every abnormality a grading in a percent scale, with percent intervals corresponding roughly to the none-mild moderate-severe grading.

The images in the DB60 were evaluated by two experienced ophthalmologists of the Ophthalmology Department of the University of Padova. In the end, a manual segmentation of the vessel network was provided by 3 technicians, opportunely trained by the same ophthalmologists who validated their final work.

The DB60 dataset allows the evaluation of the performance of the vessel tracking algorithm proposed in the following chapter of this thesis.



Univerisita' degli Studi di Padova - Dipartimento di Elettronica e Informatica

Biomedical Image Processing Group

Image ID	
Date	
Image Quality	Not gradable / Low / Fair / Good

OD	○
OS	○

Feature	*N* (0-10%)	*1* (11-40%)	*2* (41-70%)	*3* (71-100%)	%
Arterial Tortuosity					
Venous Tortuosity					
Focal Narrowing					
Generalized Narrowing					
Gunn/Salus					
Cotton Wool Spots					
Hard Exudates					
Hemorrhages					
Microaneurysms					

	0	1	2	3	4
K-W-B Grading					

Image Grading (in %)	

Contribution to image grading	
Arterial Tortuosity	
Venous Tortuosity	
Focal Narrowing	
Generalized Narrowing	
Gunn/Salus	
Cotton Wool Spots	
Hard Exudates	
Hemorrhages	
Microaneurysms	

Venous Congestion	○
Drusen	○

Comments:

Figure 6.1 Standard report form (front page).

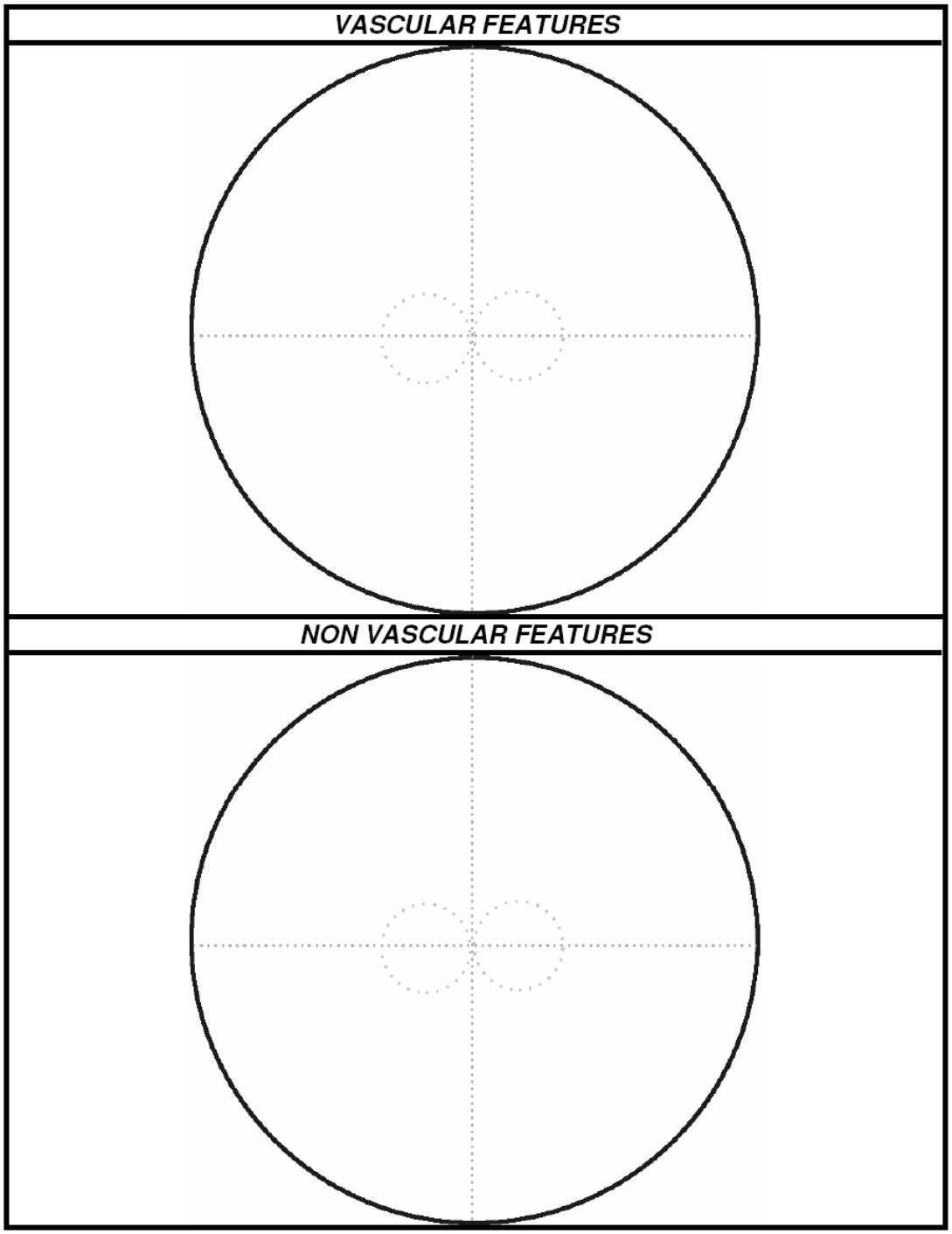


Figure 6.2 Standard report form (rear page).

Chapter 7

Vessel Tracking

Most retinopathies, deriving e.g. from hypertension or diabetes, could be early diagnosed and treated if an accurate and objective analysis of symptoms at their initial onset could be performed. The analysis should be accurate enough to detect minor pathological signs, and objective enough to be able to compare results with accepted clinical standards and with results obtained from the same patient at different times. The latter requirement is of paramount importance when assessing the effect of established therapeutic treatments and even more central when evaluating in a quantitative way the efficacy of new drugs during their development.

Most of the early symptoms indicating the onset of retinopathies are related to morphological features of the retinal vascular tree [6]. When no major signs of retinal degeneration are present (such as cotton wool spots, hemorrhages, exudates), the clinical diagnostic procedure for retinopathy always starts with a careful evaluation of the main features of the network of retinal vessels, obtained from fundus camera images. The clinically most relevant signs taken into account by expert ophthalmologists are in general vessel tortuosity, vessel caliber and its distribution among different vessels, presence of vessel caliber irregularities along the same vessel, and the so-called Gunn and Salus signs, i.e., local caliber reduction or local deviation of vessel direction at the crossings between artery and vein [64].

In order to detect and quantitatively describe these diagnostic signs, the information which has to be extracted from the vascular network regards the layout and the dimension of all the relevant vessels contained in the image. This task is relatively easy for an expert ophthalmologist if performed at a qualitative level, but rather cumbersome, highly subjective and error-prone if a set of measurements is sought for [65], [66]. For this reason, a number of research projects have been carried out to develop automatic computerized systems for the extraction of retinal vascular structure.

Here, a new system for the automatic extraction of the vascular structure in retinal images is proposed. Such system is based on a sparse tracking technique via a multi-directional graph search approach. We consider the image as a weighted un-oriented graph with edges connecting adjacent pixels and assume that vessels are minimum cost paths connecting remote nodes.

The first step consists of a preprocessing of the image. After the normalization of contrast and luminosity provided by the method proposed in [67], a simple morphological operation is employed to get rid of arterial central reflexes. Then, a seed-finding algorithm based on fast 1-dimensional multi-scale matched filters is run over a

regular grid. Simultaneous best-first search graph explorations start from each seed: when two search frontiers meet, the computed shortest path is recorded and exploited for a new search starting from it. New paths are found by iterating the procedure, until the entire vessel network is reconstructed. Then, in order to cover the unexplored region with low-contrast vessels and overcome the intrinsic inability of the algorithm to find circular paths, a custom fixing procedure is run. Lastly, a false vessel detection procedure evaluates, for each vessel, a "vesselness" value which is compared with a hard threshold.

7.1 Brief Overview of Available Methods

Automatic techniques for vessel identification have been proposed for general angiography, e.g. [69], [70], [71], and also for more specialized areas such as coronary angiography, e.g. [65], [66], [68], [72], [73], [74], [75], [76], [77], and retinal angiography, e.g. [78], [79], [80], [81], [60].

In order to illustrate the methods proposed to identify vessels in retinal images, algorithms have been grouped in five classes: local operators, matched filters, morphological processing and curvature estimation, pixel-based classification and vessel tracking. It must be noted that this categorization is only functional to a simpler narrative, as most methods include several techniques belonging to different classes of approach.

7.1.1 Local Vascular Segmentation

This set of approaches to vessel segmentation try to exploit the fact that, usually, retinal vessels are darker than their surroundings. Global or local threshold and morphological operators on the image have been proposed to identify the connected regions that represent vessels.

More recently, the local gradient of the image has been used [82], [83] as a method able to recognize the edge pairs that identify the vessels. The second derivative has been used to evaluate the local candidate vessel orientation [84], and then the pixels have been classified as vessel or non-vessel based on the gradient distribution.

7.1.2 Matched Filters

Matched filtering for the detection of the vasculature convolves a 2D kernel with the retinal image. The kernel is designed to model some feature in the image at some unknown position and orientation, and the matched filter response (MFR) indicates the presence of the feature. Three primary characteristics determine properties of the kernel. Vessels usually have a limited curvature and may be approximated by piecewise linear segments; the diameter of the vessels decreases as they move radially outward from the optic disk; and the cross-sectional pixel intensity profile of these line segments approximates a Gaussian curve.

A number of filter shapes have been investigated. The most proposed is a two-dimensional linear kernel with a Gaussian profile for segmentation of the vasculature. In [78], [85], [60] extruded and rotated Gaussian filters are used, together with filters based on lines [83] and partial Gaussian [81].

The profile of the filter is designed to match that of a blood vessel, which typically has a Gaussian or a Gaussian derivative profile. The kernel is typically rotated in 30–45° increments to fit into vessels of different orientations. The highest response filter is selected for each pixel and is typically thresholded to provide a vessel image. A number of strategies have also been proposed to identify true vessels from the filter response. A local entropy thresholding method has been proposed in [86]. In particular in [60] a strategy similar to a multi-resolution approach was proposed, iteratively decrementing an initial threshold, and then checking the obtained connected component for vessel likeliness.

As noted by several authors (Patton et al.[87], Heneghan et al. [88]) a MFR method is effective when used in conjunction with additional processing techniques. However, the convolution kernel may be quite large and needs to be applied at several rotations resulting in a computational overhead which may reduce the performance of the overall segmentation approach. In addition, the kernel responds optimally to vessels that have the same standard deviation of the underlying Gaussian function specified by the kernel. As a consequence, the kernel may not respond to vessels that have a different profile. The retinal background variation and low contrast of the smaller vessels also increase the number of false responses around bright objects such as exudates and reflection artifacts. Other objects within the image such as the boundaries of the optic nerve and some hemorrhages and lesions, can exhibit the same local attributes as vessels. There are also problems associated with detecting very fine neo-vascularization partly due to image resolution. In addition, the use of an overly long structuring element may cause difficulty in fitting into highly tortuous vessels. Several authors have proposed refinements and extensions which address many of these problems (Chaudhuri et al. [78]; Kochner et al. [89]; Hoover et al. [60]; Lowell et al. [90]; Yang et al. [91]).

7.1.3 Morphological processing and curvature estimation

The basic morphology of the vasculature is known a priori to be comprised of connected linear segments. Morphological operators have been applied to vasculature segmentation (Zana and Klein [92]) and also to microaneurysm extraction. Morphological processing for identifying specific shapes has the advantage of speed and noise resistance. Gregson et al. [93] utilize morphological closing to help identify veins in the automated grading of venous beading by filling in any "holes" in the silhouette of the vein created during the processing procedure.

The main disadvantage of exclusively relying upon morphological methods is that they do not exploit the known vessel cross-sectional shape. In order to overcome this limitation, Mendonca et al. [94] presented a hybrid algorithm that starts with the extraction of vessel centerlines, which are used as guidelines for the subsequent vessel filling phase. For this purpose, the outputs of four directional differential operators are processed in order to select connected sets of candidate points to be further classified as centerline pixels using vessel derived features. The final segmentation is obtained using an iterative region growing method that integrates the contents of several binary images resulting from vessel width dependent morphological filters.

7.1.4 Pixel-based classification

Several authors have investigated a number of classification methods for the segmentation of the vessels.

Artificial neural networks have been extensively investigated for segmenting retinal features such as the vasculature (Akita and Kuga [95], Gardner at al. [96]) making classifications based on statistical probabilities rather than objective reasoning. These neural networks employ mathematical "weights" to decide the probability of input data belonging to a particular output. This weighting system can be adjusted by training the network with data of known output typically with a feedback mechanism allowing retraining.

Sinthanayothin et al. [97] preprocessed images with PCA to reduce background noise by reducing the dimensionality of the data set and then applied a neural network to identify the pathology. The result of the approach was compared with an experienced ophthalmologist manually mapping out the location of the blood vessels in a random sample of seventy-three 20×20 pixel windows and requiring an exact match between pixels in both images.

Other classifying methods have been proposed. Soares at al. [98] proposed a Bayesian classifier with class-conditional probability density functions (likelihoods) described as Gaussian mixtures. Feature vectors are composed of the pixel's intensity

and two-dimensional Gabor wavelet transform responses taken at multiple scales. The Gabor wavelet proved capable of tuning to specific frequencies, thus allowing noise filtering and vessel enhancement in a single step. The classifier employed yielded a fast classification, while being able to model complex decision surfaces. The probability distributions have been estimated based on a training set of labeled pixels obtained from manual segmentations.

Ricci and Perfetti [99] employed a support vector machine classifier. A line detector, based on the evaluation of the average grey level along lines of fixed length, is passed through every target pixel of the image at different orientations. Two segmentation methods have been considered. The first used the basic line detector whose response has been thresholded to obtain unsupervised pixel classification. As a further development, two orthogonal line detectors have been employed along with the grey level of the target pixel to construct a feature vector for supervised classification using a support vector machine.

Staal et al. [58] proposed a system based on extraction of image ridges, which are the natural indicators of vessels centerlines. The ridges are then used to compose primitives for the vessel in the form of line elements composed by ridge pixels which belong to the same ridge. With the line elements an image is partitioned into patches by assigning each image pixel to the closest line element. Every line element constitutes a local coordinate frame for its corresponding patch. For every pixel, feature vectors are computed by evaluating the properties of the patches and the line elements. The feature vectors are classified using a knn-classifier and sequential-forward feature selection.

Although supervised classification methods have provided remarkable results, they have a noteworthy disadvantage in the necessity for configuring the classifier with training data or a 'gold standard'. This gold standard data set consists of a number of images whose vascular structure must be precisely marked by an ophthalmologist. However, as noted by Hoover et al. [60] there is significant disagreement in the identification of vessels even amongst expert observers.

7.1.5 Vessel Tracking

Vessel tracking algorithms segment a vessel between two points. Unlike the previously described techniques for vasculature segmentation they work at the level of a single vessel rather than the entire vasculature. They start from a point on a vessel and move along it as far as possible by analyzing consecutive local areas, e.g. drawing scan lines across the vessel. The centre of the longitudinal cross-section of vessel is determined with various properties of the vessel including average width and tortuosity measured during tracking.

In order to identify the vessel profile along the scan line, matched filters are still used [69], [70], [68], [79], [81], [60], together with derivative analysis [75], [76], morphological filters [71] or Fuzzy C-Mean classifiers [80].

The main advantage of vessel tracking methods is that they provide highly accurate vessel widths, and can provide information about individual vessels that is usually unavailable using other methods.

Unfortunately, they require the starting point, and usually the end point, of a vessel to be defined by a user and are thus, without additional techniques, of limited use in fully automated analysis. In addition, vessel-tracking techniques may be confused by vessel crossings and bifurcations (Frameet al. [61]). Teng et al. [62] address several of these problems by proposing the use of matched filters.

7.2 Methods

The rationale of our method is to consider the image as a weighted un-oriented sparse graph where each node represents a pixel. The graph edges describe the 8-adjacency among pixels in the image. Under the assumption that vessels are minimum cost paths connecting remote nodes, we employ a graph search approach in order to identify them.

As a first step, luminance and contrast drifts are removed from the images using a correction method previously developed [67]. This pre-processing also ensures uniform and invariant inter-image contrast and luminosity. Then a simple grayscale opening provides an appreciable reduction of the luminosity of the arterial central reflex, whose presence would often hamper the correct tracking of large vessels. A seed point extraction identifies a set of points used as starting nodes for simultaneous searches. The most promising node to be expanded is selected at each iteration. When such node resides also in the exploration frontier of another node, the shortest path connecting the two is recorded, and considered as starting point for a new search. A subsequent refinement step connects the vessel segments with a custom fixing algorithm. In order to locate the estimated axis at the very middle of the vessel, the transversals symmetry along the axis is computed and its position is coherently adjusted. Lastly, a false vessel detection procedure evaluates a “vesselness” function in order to discriminate the true positive vessels from the ones which are to be discarded.

7.2.1 Preprocessing

Luminance and contrast drifts are removed using the iso-illumination method described in [67]. This pre-processing step also ensures uniform inter-image contrast and luminosity, therefore ensuring luminance and contrast invariance.

A second preprocessing step consists in a grayscale opening. Such morphological operation could be considered a naïve approach, since the results of its application depend only on geometrical information. However, in this specific instance, the peculiar features of the graph search algorithm we employed have demonstrated to couple optimally with this operation.

The main reason to employ a grayscale opening consists in the possible presence of central reflex in the retinal arteries and arterioles. In some datasets only a few (if not any) images show central reflexes (sometimes hardly appreciable), while certain datasets have almost all images with a marked central reflex. Namely, while STARE and DRIVE datasets are composed of images in which arteries and veins look almost the same, all the UoW Dataset images show a very marked central reflex in the arteries. This feature alone could strongly hamper a vessel tracking strategy not designed to tackle it. However, the consistency of a tracking algorithm able to track both a "normal vessel" and a vessel with a marked central reflex would come with an increased complexness of the algorithm and the loss of efficiency in the tracking process.

The grayscale opening allows the "filling" of the central of the arteries reflex with a relatively affordable drawback: it merges vessels that are closer than the dimension of the structuring element used. As explained in Sec. 7.3 the false vessel detection easily allows to get rid of those spurious tracked segments.

In grayscale morphology, images are functions mapping a Euclidean space or grid E into $\mathbb{R}\cup\{\infty,-\infty\}$, where $\mathbb{R}$ is the set of reals, ∞ and $-\infty$ are elements respectively larger and smaller than any real number. Grayscale structuring elements are also functions of the same format, called "structuring functions". Opening is the dilation of the erosion of a image *f(x)* by a structuring element *b(x)*:

$$f \circ b = (f \ominus b) \oplus b \tag{7.1}$$

where $\ominus$ and $\oplus$ denote erosion and dilation, respectively. In this application we used a flat structuring element. Flat structuring functions are functions *b(x)* in the form

$$b(x) = \begin{cases} 0, & x \in B \\ -\infty, & otherwise \end{cases} \tag{7.2}$$

where $B \subseteq E$. We are in a bounded, discrete case (E is a grid and B is bounded) so the grayscale erosion of f by b is given by

$$(f \ominus b)(x) = \min_{z \in B} (f(z - x)) \tag{7.3}$$

while the grayscale dilation of f by b is given by

$$(f \oplus b)(x) = \max_{z \in B} (f(z - x)) \tag{7.4}$$

Since we can expect that the width of a central reflex is between 1 and 6 pixels, depending on the μm/pixel ratio of the image, we conservatively chose the dimension of the structuring element depending on the image dimension, namely a 2 pixel radius disk in the DRIVE and STARE datasets, and a structuring element of 4 pixel radius disk in the DB60, UoW, and MEH datasets.

Figure 7.1 shows the appearance of an example image after erosion and then after dilation with different structuring element dimensions. Figure 7.2 shows an example of both the advantages and the disadvantages that can be obtained by employing the morphological operation.



(a) original image



(b) erosion with disk of radius 1



(c) opening with disk of radius 1



(d) erosion with disk of radius 2



(e) opening with disk of radius 2



(f) erosion with disk of radius 3



(g) opening with disk of radius 3

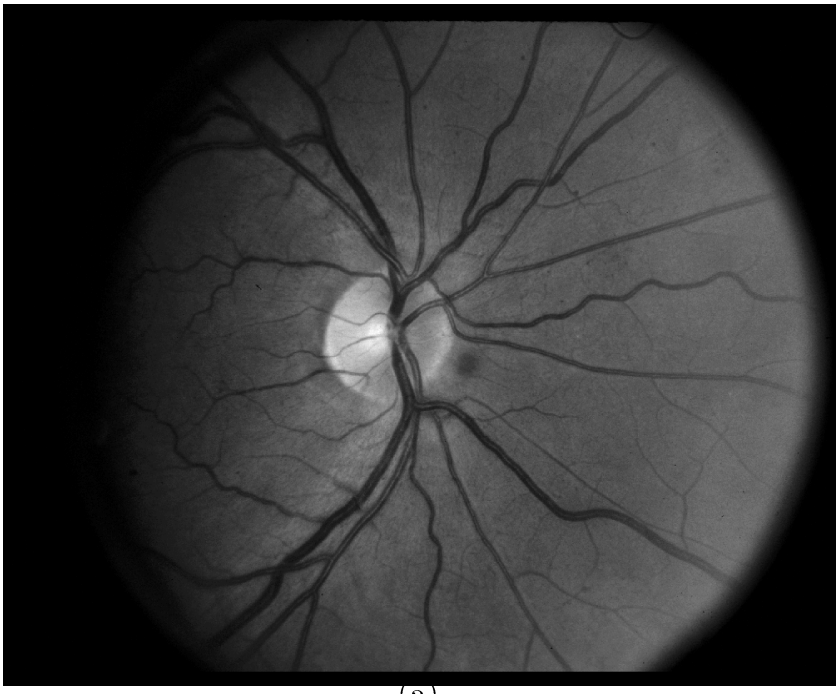


(h) erosion with disk of radius 4

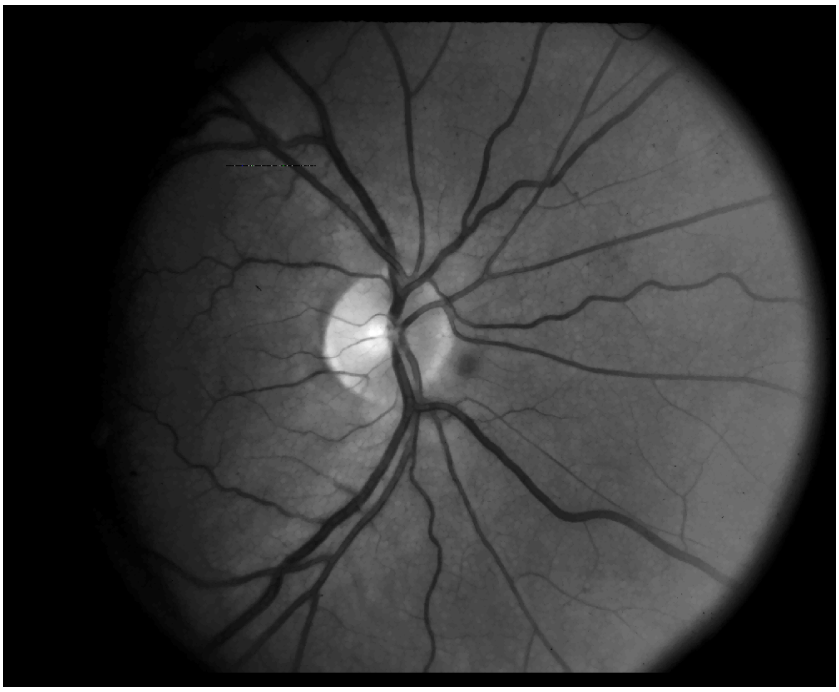


(i) opening with disk of radius 4

Figure 7.1 (a) original image and the image results of the erosion with a disk of radii 1, 2, 3, and 4 (left column), and a subsequently dilation with the same structuring element (right column).



(a)



(b)

Figure 7.2 (a) An example image from the UoW dataset; (b) after opening with a disk of 4 disk radius. While the central reflexes become quite attenuated, some vessels are erroneously merged.

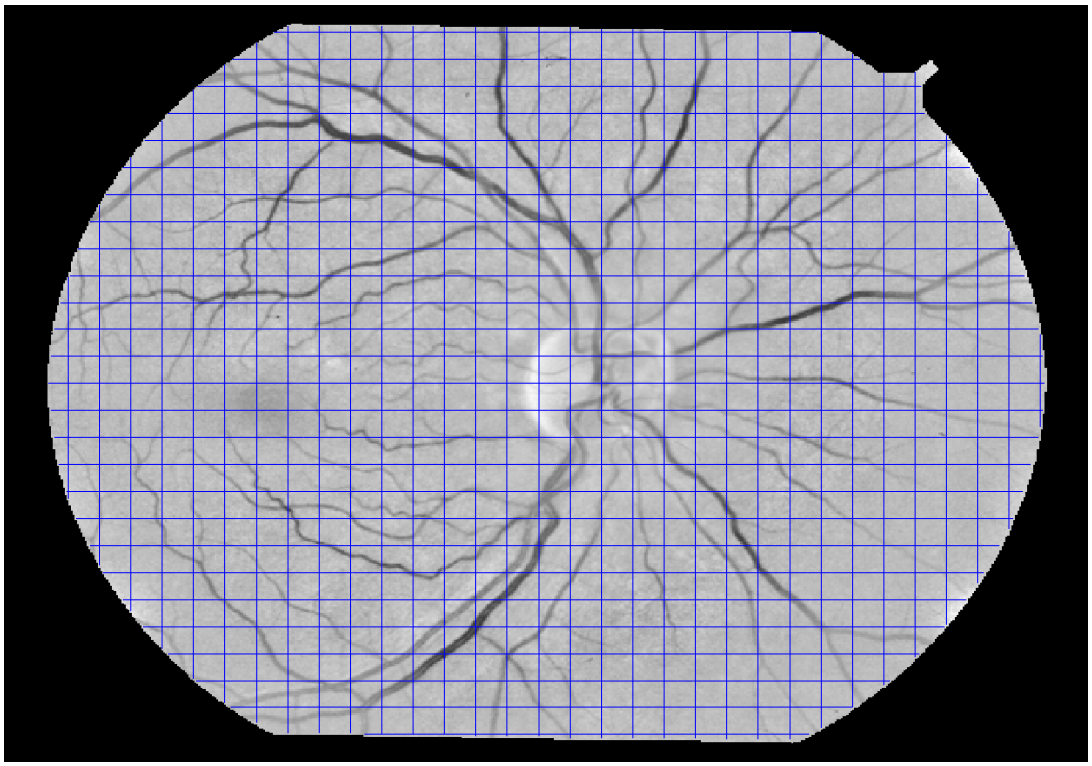
7.2.2 Seed-Finding Procedure

An initial seed-finding algorithm, based on multi-scale matched filters over two regular grids, is run (Figure 7.5).

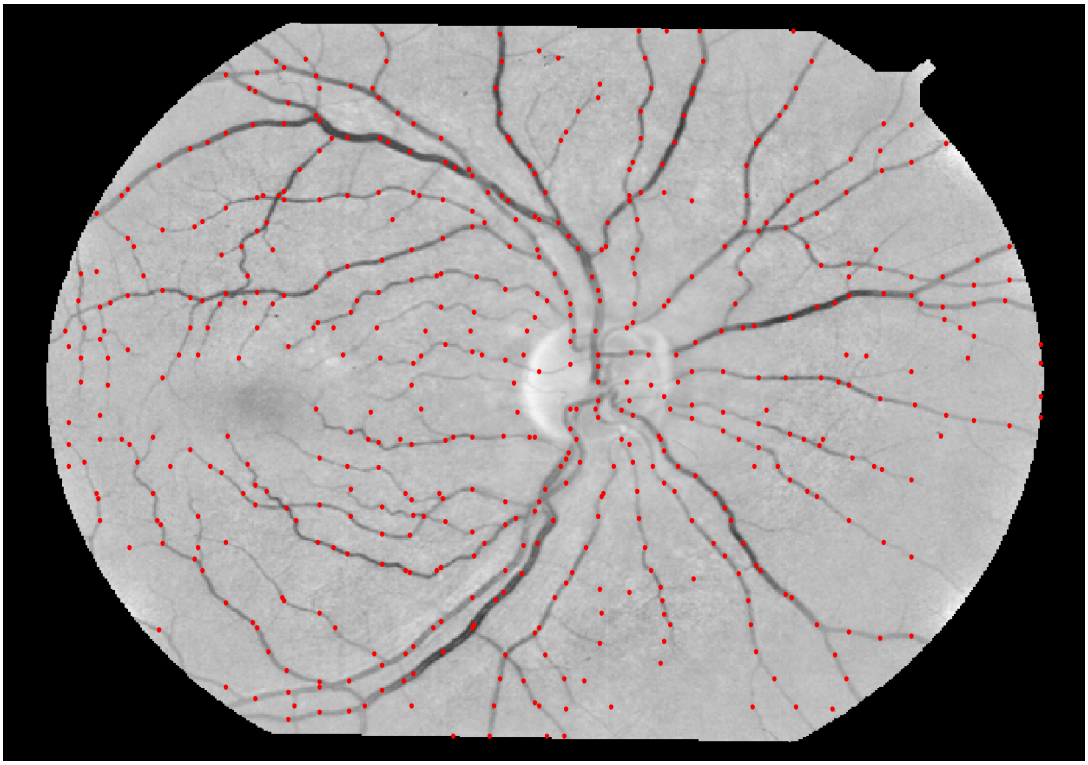
The objective of this module is to extract a set of points (seeds) from which the tracking step will start. Since the whole point of the *sparse* tracking procedure is to ensure that even non-connected vessels can be tracked, these seed points should be as spread-out as possible in the image. In order to do this, a number of lines of the image are analyzed to search for candidate seed points. From each selected line the gray-level profile $p(x)$ is extracted and analyzed by means of a matched filter method, looking for patterns corresponding to candidate vessels. The convolution of the profile with a discretized Laplacian of Gaussian function filter over multiple scales is performed. The output of each filter is then normalized, and the maximum response among the output results is considered (see Eq. 7.5 and Eq. 7.6).

The response of the convolution depends on the angle defined by a vessel and the line, from which the profile is extracted, it crosses. As we would to maximize the difference of appearance in the profile between background and vessel, the aim is to define the grid lines as perpendicular as possible to the vessels.

We opted to design two regular grids: one of equally spaced rows and columns and the other equal but rotated by 45°. As can be seen in Figure 7.3 and Figure 7.4, the two differently oriented grids allow locating seed points over differently oriented vessels.

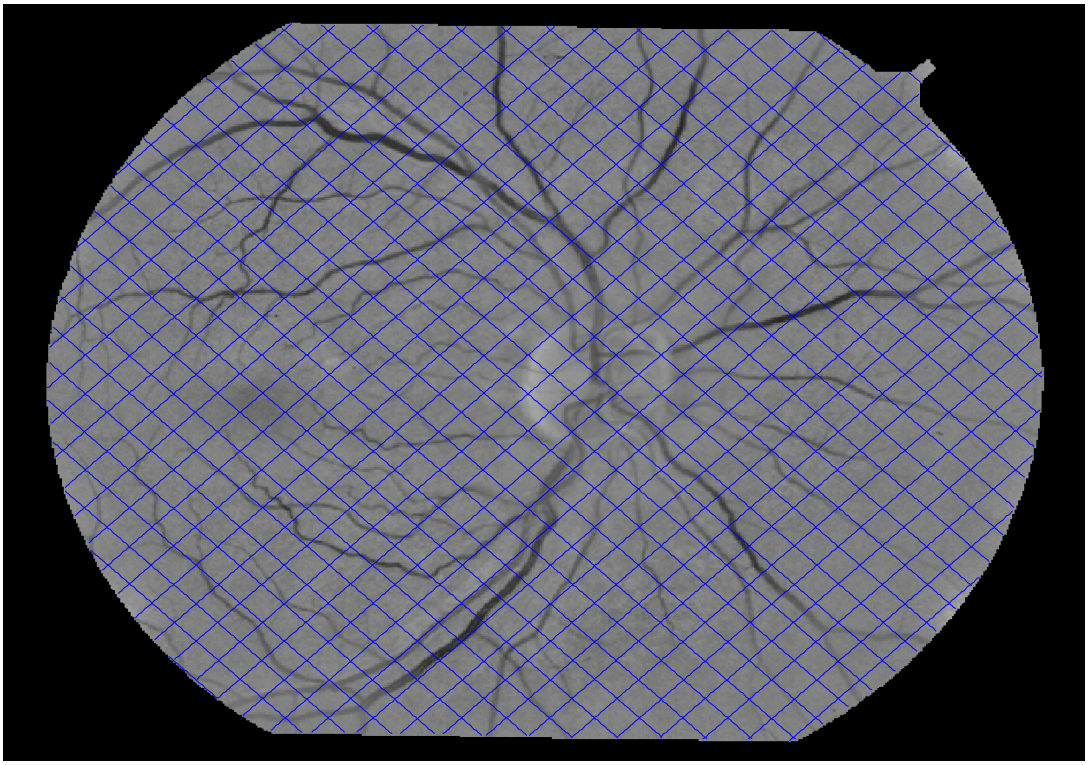


(a)



(b)

Figure 7.3 (a) regular grid of equally spaced rows and columns and (b) the corresponding seeds found.

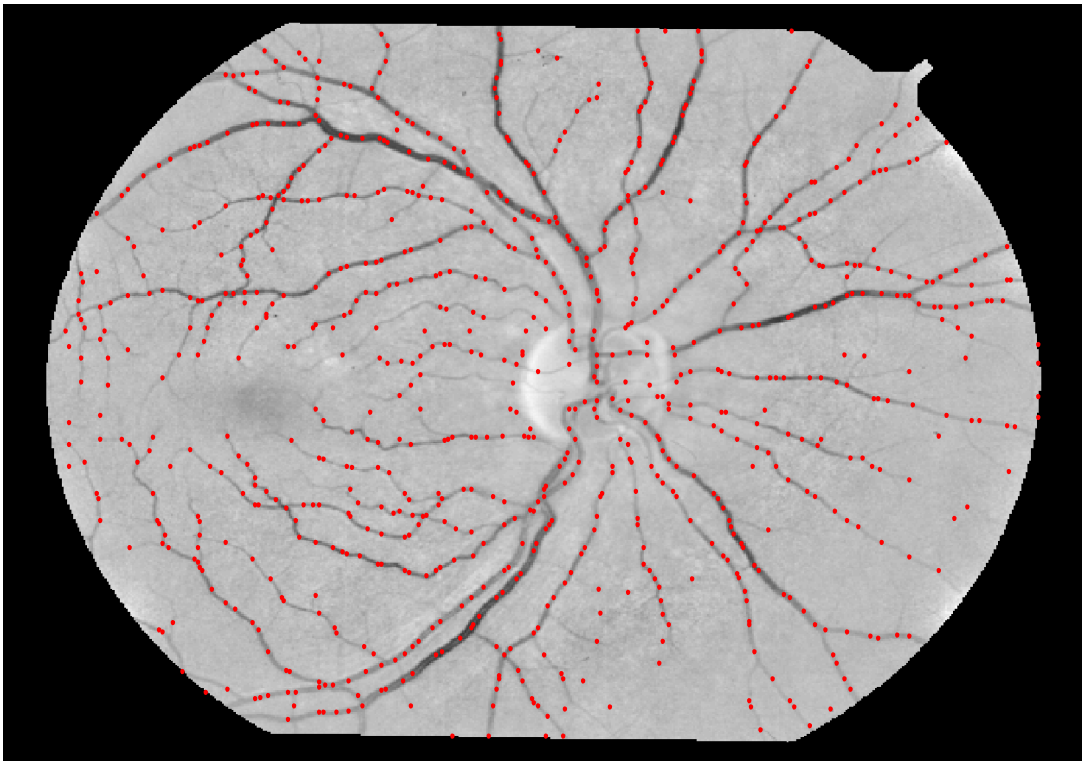


(a)



(b)

Figure 7.4 (a) regular grid of equally spaced perpendicular lines, at an angle of 45° with the image coordinates; (b) the corresponding seeds found.



ù

Figure 7.5 The total set of seeds found by employing both the horizontal and the inclined grids.

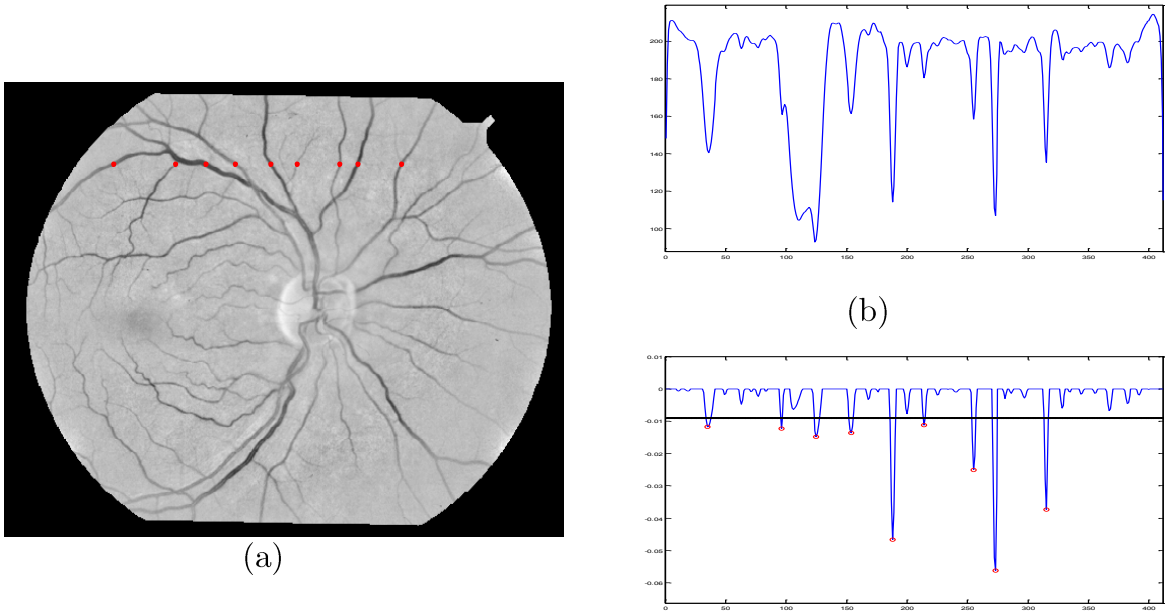
The 0-mean discrete filter used is described by the following equation:

$$f_{sc}(x) = \begin{cases} -1, & 1 < x \leq sc \\ 2, & sc + 1 < x \leq 2sc \\ -1, & 2sc + 1 < x \leq 3sc \end{cases} \tag{7.5}$$

where x and the scale sc are discrete values. Given the profile $p(x)$, the family of filters $f_{sc}(x)$, and a set of scales SC, the final filter response is given by:

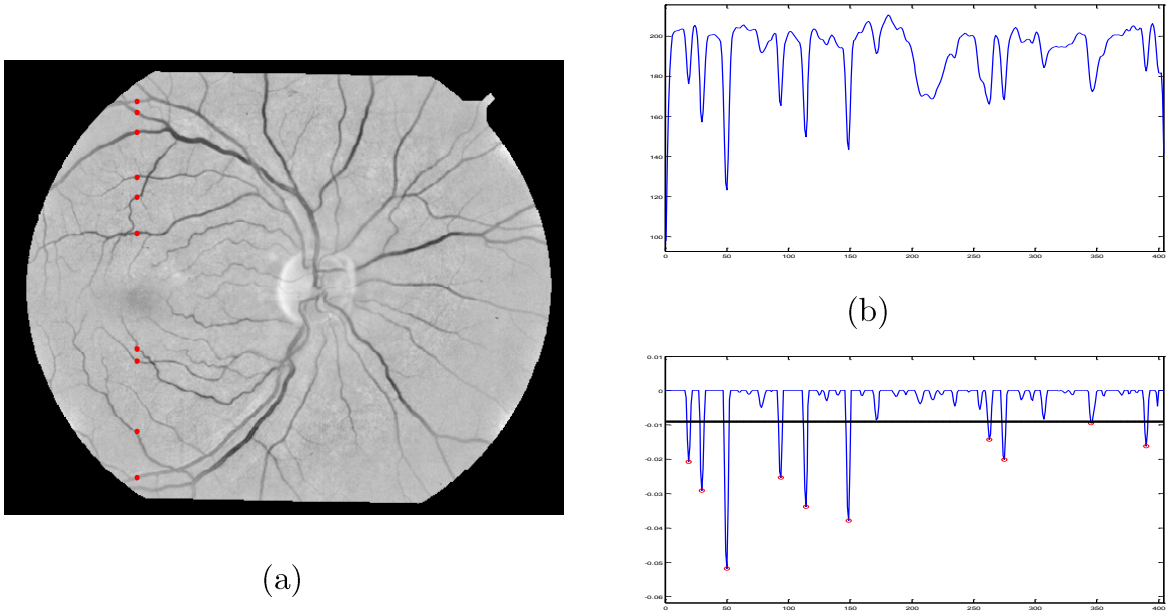
$$res(x) = max\{\, p(x) \otimes f_{sc}(x) \mid sc \in SC \,\} \tag{7.6}$$

where $\otimes$ is the operation of convolution. Looking at the most prominent local minima of $res(x)$, we derive a set $K = \{k_i,\ i = 1{:}\,N_k\}$ of points on the profile suggesting the possible presence of vessels in the corresponding points of the image. From now on, $S = \bigcup_{\infty} K$ is the entire set of detected seed points.



(a) (b) (c)

Figure 7.6 (a) seeds found in the image by analyzing the profile (b); (c) the profile resulting from the matched filtering is compared with a threshold.



(a) (b) (c)

Figure 7.7 (a) seeds found in the image by analyzing the profile (b); (c) the profile resulting from the matched filtering is compared with a threshold.

It is worth noting that we gave more importance to the sensitivity of the seed finding procedure (detected vessels over true vessels) than to its specificity (not detected vessels over "non-vessel"). As explained in Sec. 7.2.4, the efficacy of our algorithm is

not undermined by the presence of wrong seed points but rather by their lack in critical regions of the image.

7.2.3 Multi-directional Shortest Path Search Idea

The image I is a 2-dimensional array of R rows and C columns; an undirected graph $G = (N, E)$ can be derived from it. Let each node $i \in N$ be associated to the pixel $I\big(r(i), c(i)\big)$ having gray level $g(i)$. The edge $(i, j) \in E$ exists if $|r(j) - r(i)| \leq 1$ and $|c(j) - c(i)| \leq 1$. To each edge $(i, j) \in E$, a cost is associated by a real-value function $f: E \to \mathbb{R}^+$ which will be defined in Sec. 7.2.4.4. A path P in G is a sequence of nodes that are sequentially connected by edges in E. A path P connecting the nodes $a, b \in N$ is the shortest one if $\sum_{(i,j)\in P} f(i, j)$ is minimal among all paths connecting a to b.

Given a graph G and a node s, the shortest path tree problem consists in finding a spanning directed tree T^* rooted at s such that the cost of all paths in T^* from s to all other nodes is minimal in G. Algorithms that compute T^*have a common scheme: starting from an initial tree $T(0) \subseteq T^*$, they iteratively update it until, at the iteration n, $T(n) = T^*$ is found. The problem can be solved by the Dijkstra algorithm [100], which can also be used for finding the shortest path from two single vertices by early stopping the algorithm at the iteration n in which $T(n)$ meets the target vertex (without computing the entire T^*). This latter problem can be solved by a bidirectional search approach [101], which, for a running time profit, runs two simultaneous searches: one from the initial state and one from the goal, and stops when the two $T(n)$ meet.

The specific problem we are dealing with, however, requires the connection of several nodes. The scheme of the proposed algorithm is to run multiple shortest path searches, each starting from the seeds found according to the procedure described in Sec. 7.2.2. When two trees meet, they provide the shortest path connecting their roots, but differently from the bidirectional approach, the algorithm does not stop. Instead, the two trees merge into a single new tree, from which the search goes on in successive iterations.

7.2.4 The Algorithm

7.2.4.1 Initialization

Every $s \in S$ is considered as the root of a tree T_s. A different identification tag is assigned to each tree, so that for every explored node it is possible to trace which tree

it belongs to. Also, every node $i \in T_s$ carries two additional pieces of information: the distance d_i providing the total cost of the path from i to s, and the reference p_i indicating the predecessor of i in $T_s(n)$. At the first iteration ($n = 0$), every $T_s(0)$ coincides with its root s and d is equal to zero for all $s \in S$, whereas for all other nodes of the graph d is assumed to be ∞.

Algorithm 1 Initialization

```
1: function INITIALIZE(S, G)
2:     for all s ∈ S do                          ▷ for all seeds
3:         d_s ← 0                               ▷ distance from the source
4:         tag_s ← s                             ▷ tree to which the node belongs
5:         p_s ← ∅                               ▷ predecessor in the tree
6:         state_s ← leaf                        ▷ exploration starts from leaves
7:     end for
8:     for all n ∈ N(G)\S do                     ▷ for all other nodes
9:         d_n ← ∞
10:    end for
11: end function
```

7.2.4.2 Search

At each iteration n, the leaf node i with the minimum distance, i.e. such that

$$i(n) = \text{argmin}_i\{d_i \mid i \in \cup \; leaves\, of\, all\; T(n)\} \tag{7.7}$$

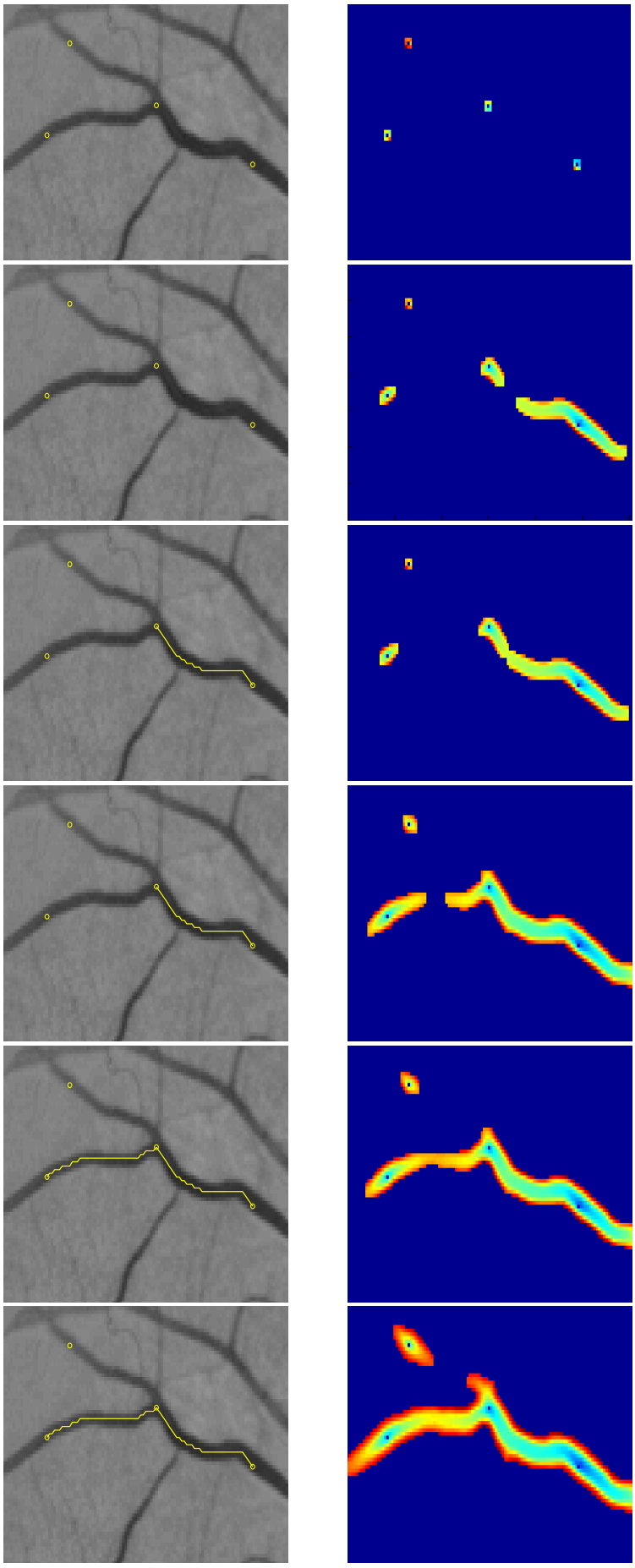
is selected. The set $J(n)$ of the nodes reached by the outgoing edges of $i(n)$ is considered. If there is a node $j \in J$ that belongs to another search tree, then the two trees are merged (see 7.2.4.3). Otherwise, all $j \in J$ are explored to expand the current T: the cost function f, defined below, is computed and for each j such that $f(i,j) < d_j$, then d_j and p_j are respectively updated to $f(i,j)$ and i.

Algorithm 2 Multidirectional Graph Search

```
1: function MULTISEARCH(S, G)
2: INITIALIZE(S,G)
3:     P ← ∅
4:     repeat
5:         i ← arg min_i {d_i | state_i = leaf, i ∈ N(G)}
6:         state_i ← explored
7:         for all j | (i, j) ∈ A(G) do
8:             if tag_j ≠ tag_i, state_j = explored then
9:                 P ← P ∪ MERGE(i, j, G)
10:            else
11:                state_j ← leaf
12:                tag_j ← tag_i
13:                newdistance ← COSTFUNCTION(i, j)
14:                if newdistance < d_j then
15:                    d_j ← newdistance
16:                    p_j ← i
17:                end if
18:            end if
19:        end for
20:        ec ← EVALUATEENDCONDITION(P, G)
21:    until ec
22: return P
23: end function
```

7.2.4.3 Merging

The merging operation consists of two steps. First, the minimum path is reconstructed by exploiting the references p, i.e. step by step backward from the node i and from the node j along their respective tree, until a seed point $s \in S$ is reached or until a node belonging to a previously found path is reached. Second, the two exploration trees are merged: all nodes belonging to the two touching trees have their identification tag equaled. This operation allows the resulting merged tree to coherently interact with the others in succeeding iterations.



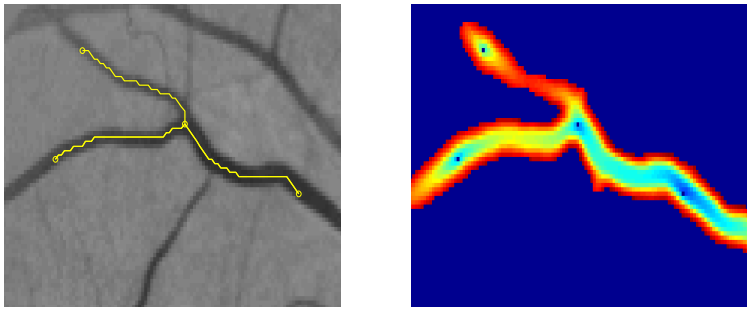


Figure 7.8 Example of exploration of four manually deployed seeds. On the left column the original image with the superimposed seeds and the identified paths. On the right column, the images of the matrix where for each pixel i the distance value d_i is stored.

7.2.4.4 Cost Function

We defined the cost function associated to the edge (i,j) as described by eq. (7.7) and (7.8), where $g(i)$, recalling from Sec. 7.2.3, is the gray level of the pixel represented by the node i.

$$f(i,j) = d_i + k_{i,j} w_{i,j} \tag{7.7}$$

$$k_{i,j} = g(i)^{p_1} + |g(i) - g(j)|^{p_2} \tag{7.8}$$

where the weight $w_{i,j}$ has the role of penalizing the exploration of the d-adjacent pixels of i: $w_{i,j} = 1$ if i and j represent 4-adjacent pixels, otherwise $w_{i,j} = \sqrt{2}$ (Figure 7.9).

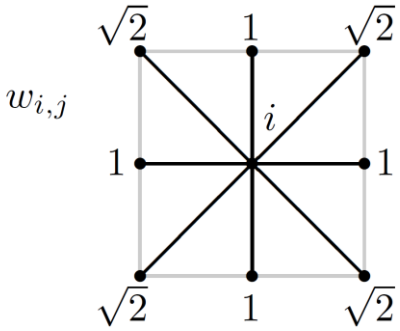


Figure 7.9 Starting from i, the weight $w_{i,j}$ has the role of penalizing the exploration of the d-adjacent pixel as their distance is $\sqrt{2}$ times the distance of the 4-adjacent pixels.

The first term of the sum (7.8), $g(i)^{p_1}$, penalizes the exploration of brighter pixels, while the second term, $|g(i) - g(j)|^{p_2}$, penalizes the transition from the inside to the outside of the vessels and *vice versa*. p_1 and p_2 are empirically chosen: however, we noted that if both p_1 and p_2 are ≥ 3, the performances provided by the algorithm tend to be good and are qualitatively similar for every arbitrary chosen value.

7.2.4.5 End Condition

It is worth noticing that, according to the defined f and the appearance of the regions around the false positive seeds, the exploration starting from the latter tends to be done at a later time than the one from the true positive seeds. Indeed, in the last iterations only false positive seeds remain to be connected. To exploit this feature, minimizing the occurrence of false vessels detection, an end condition has been defined.

In order to provide a more solid end condition, we defined it as a sequence of two checks: when the first check is verified the second one is performed.

The rationale of the first check is to consider the degree of connectivity of the estimated vessel network after a cyclic number of iterations. We considered the estimated vessel network as a set of trees in which the edges are the vessel segments, the nodes correspond to the bifurcations among vessel segments, and the leaves of the trees are the ends of the vessel segments. It is worth noticing that the trees mentioned in this circumstance have no relations with the search trees described in the previous sub-sections, since they are defined at different conceptual levels and have different purposes.

A perfect binary tree of height h has a number of nodes $n = 2^{h+1} - 1$ and a number of leaf nodes $l = 2^h$. It can be easily seen that the l/n ratio tends to ½ as h tends to infinite, and $l/n^* = ½$ is the lower bound of each possible binary tree. The behavior of the search algorithm can be qualitatively described as follows: in a first stage seed points are connected in pairs, and only after a number of iterations the other non-connected seed points are connected to the segments already found. In other words, in the first stage of the processing the number of leaves (i.e. ends) is far larger than the number of total nodes (i.e. ends plus bifurcations). However, the more the iterations of the algorithm, the more the network becomes connected, approaching towards the l/n^* ratio. Of course we cannot expect that a retinal vessel network geometry behaves like a perfect binary tree, but we empirically noticed that as the best compromise between false vessel detection and true vessel network covering was reached, $log\left(\frac{l}{n}\right) \cong 1$. This last threshold defines one of the two checks constituting the end condition of the tracking algorithm. Since in the earliest iterations of the algorithm the l/n ratio value could be very unstable, the check starts to be performed after a short delay "of confidence". The limit of such approach is that it can work only under the assumption that the processed image is a processable image (in the

other case the whole proposed framework would not be able to provide the desired results).

The second check becomes active only when the first one is verified, i.e. when $log\left(\frac{l}{n}\right)$ reaches the threshold value. From now on, every new path found is accepted only if the average gray level of its pixels significantly differs from the local average value of the preprocessed image. When three paths are consecutively discarded in this way, the algorithm ends, since it is assumed that the remaining paths cannot be better than those already found. It is worth noting that this step is effective only if it is applied to images whose luminance and contrast drifts have been removed as previously mentioned [67].

7.2.5 Post-Processing

A fault of the proposed algorithm is that it allows to connect N given seed points with at most only N-1 paths. Another drawback is the algorithm intrinsic inability to find circular paths [102]. To overcome these limitations, we have developed a fixing procedure that aims at finding possible missing branches in the vessel network reconstructed up to this point.

The rationale is to consider every end-point of the current vessel network and try to find an additional path that starts from it and proceeds beyond it to arrive at another point of the network. The segment of the current network ending at the end-point is smoothed, so as to provide a robust estimate of the perpendicular line at the end-point, which identifies the "forward" region to be explored by the fixing procedure.

The algorithm presented in Sec. 7.2.4 is then run once more, using all the end-points as seeds and having the constraint to explore the "forward" region only, without being allowed to backtrack along the vessel already traced. In this new instance of the algorithm, the threshold value of the first check of the end condition is updated to $log(l/n) = 0.3$.

7.3 False Vessel Detection

The tracking of false vessel, i.e. to consider something that is not vessel as vessel, depends mainly on the position of false seed points located in darker regions of the fundus image (such as in the fovea) or in hemorrhages.

In order to develop a false vessel detector that is able to perform well on the errors of the tracking algorithm, we have to describe vessels with features as different as possible if compared to the ones used in the tracking process. In this section we present a binary classification method based on a measure of "vesselness" determined

by the analysis of the eigenvectors of the Hessian matrix computed on the vessel axes [106].

All vessels share the same feature: in their inside, along the axis, they show gray scale uniformity, with only exceptions of in the case of a small gradient due to the slow change of luminosity through the image and the possible appearance of central reflexes. The rationale is to employ the information on the direction of the gray level gradient along the estimated axis: if this proves constant and coherent with the axis direction, we can assume that the estimation was correct. On the contrary, a fast and casual variability in the gradient direction is characteristic of the background region.

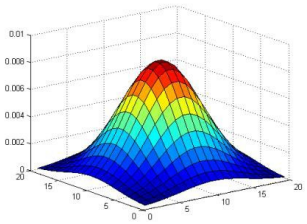
The computation of the direction of the gray level gradient is easily obtainable from the analysis of the eigenvalues and eigenvectors of the Hessian matrix

$$H_{x,y} = \begin{bmatrix} \frac{\partial^2 L}{\partial x^2} & \frac{\partial^2 L}{\partial x \partial y} \\ \frac{\partial^2 L}{\partial y \partial x} & \frac{\partial^2 L}{\partial y} \end{bmatrix} \tag{7.9}$$

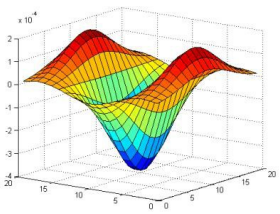
whose elements are determined by the convolution of the image with the second-order partial-derivatives of a two-dimensional Gaussian distribution G. In order to keep the computational load low, the convolution is calculated only in correspondence of the pixels covered by the estimated axes.

Once the convolutions have been performed, it is possible, for every pixel, to determine the Hessian matrix. Since it is symmetric, its eigenvectors are orthogonal and represent the main directions in which the local two-order structure is decomposed. The two eigenvectors ν^+ and ν^-, associated with the eigenvalues λ^+ and λ^-, indicates respectively the direction of faster change (ν^+) and lower change in intensity.

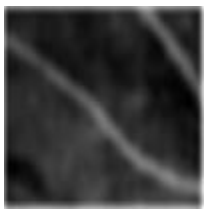
For each pixel of the estimated axis, the difference d between the angles of the vessel axis direction and the direction of ν^- is computed. We can notice that as the estimated axis leaves a vessel, entering the background region, d becomes unstable.



the kernel G



$\frac{\partial^2 G}{\partial x^2}$



$\frac{\partial^2 L}{\partial x^2}$

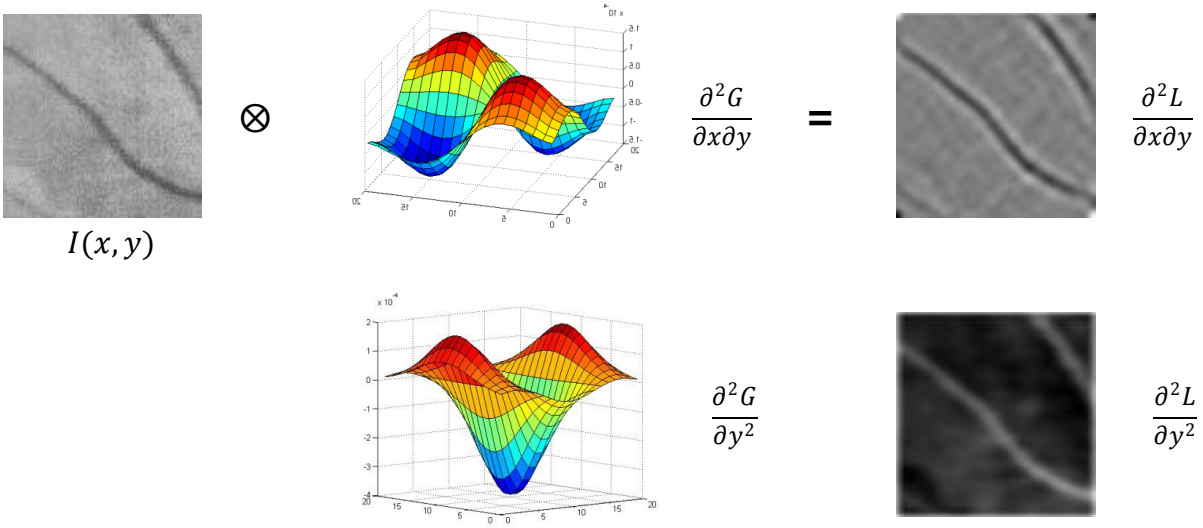
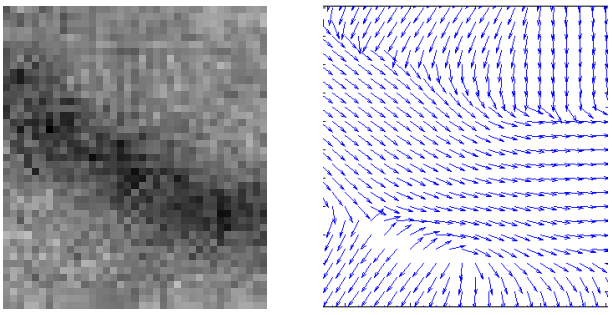


Figure 7.10 Simple scheme that highlights the usefulness of the second derivative of the kernel G and the three obtained components.



(a) (b)

Figure 7.11 (a) Detail of a vessel and (b) the ν^- corresponding to each pixel.

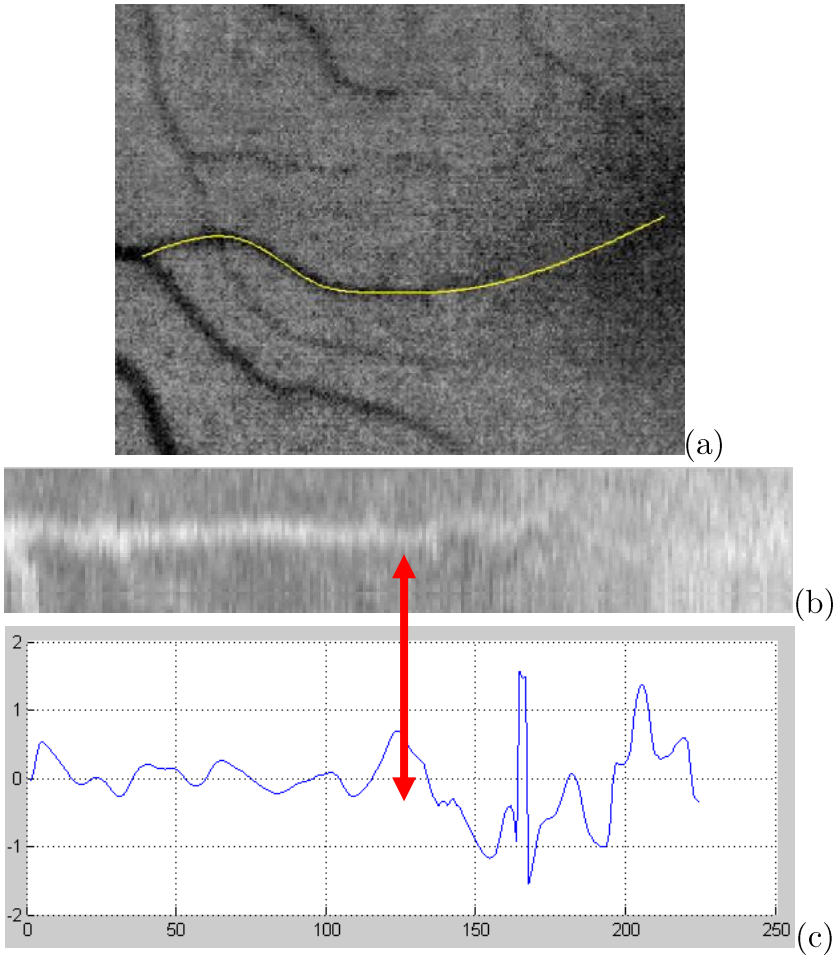
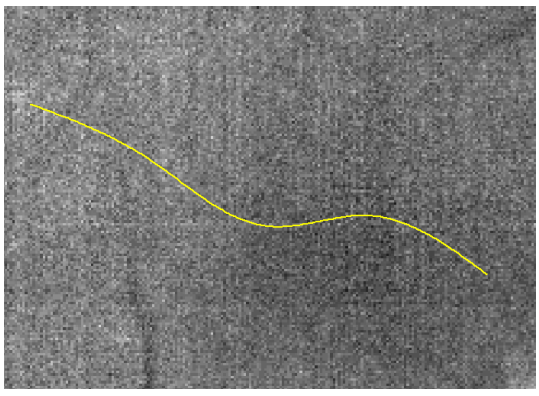
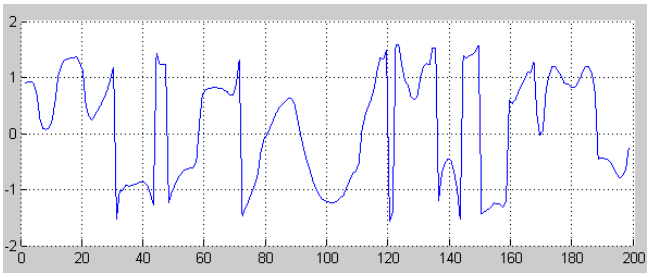


Figure 7.12 (a) Partially false tracked vessel: the second half has been detected because of false seeds laying in the fovea; (b) image of the vessel composed by taking into consideration the longitudinal profiles of the axis (displayed to provide a straightforward view); (c) difference between the angles (in radians) of the vessel axis directions and the directions of ν^{-}, along the estimated axis.



(a)



(b)

Figure 7.13 (a) vessel axis manually drawn on the background; (b) difference between the angles (in radians) of the vessel axis directions and the directions of ν^{-}, along the estimated axis.

The rationale is to classify the pixel of the axis as false vessel pixel when the corresponding d goes outside an interval of confidence, which has been empirically set to $\pm 0.2\pi$. Since the value of d computed on a background region is casual, it could happen that, for a number of false vessel pixels, d falls in the confidence region. This is the reason why after the pixel-wise classification provided by the thresholds we introduced a further verification, which tests the "choppedness" of the true-classified pixel along the axis. Simply put, a segment of axis is considered true vessel if it is composed of more than 20 consecutive pixels whose d falls in the interval of confidence.

This described implementation for the false vessel detection reached an average sensitivity of 63.8%, an average specificity of 91.9%, and a total average accuracy of 88.5 % on the DB60 dataset.

7.4 Results

The performance of the algorithm is compared with the human-labeled segmented version of the 60 images of our DB60 dataset, of the 20 test images of the DRIVE dataset, and of the 20 images of the STARE dataset, all of them assumed as ground-truth reference. Those segments of the computer-estimated network that do not exist in the ground-truth images (i.e., that exit from the vessel mask) are considered as false vessels. *Sensitivity* has been evaluated as the percent fraction of the length of correctly tracked vessels over the total length of the ground-truth vessels (skeletonization of the ground-truth vessel mask). *False vessel detection* has been evaluated as the percent fraction of the length of the false vessels over the length of all estimated vessels (not to be confused with the *false detection rate*). Results are summarized in Table 7.1, Table 7.2, and Table 7.3 in terms of mean, standard deviation, maximum and minimum of both sensitivity and false vessel detection over the whole data sets.

DB60	mean	sd	max	min
sensitivity	85.86	4.72	98.31	76.58
false detection	5.18	2.11	10.71	0.98

Table 7.1 Results of the vessel estimation in the 60 images of the DB60 dataset (%).

DRIVE	mean	sd	max	min
sensitivity	71.37	6.09	86.29	55.83
false detection	4.82	2.36	8.04	1.47

Table 7.2 Results of the vessel estimation in the 20 test images of the DRIVE dataset (%).

STARE	mean	sd	max	min
sensitivity	66.34	5.3	82.04	55.25
false detection	3.07	2.21	8.30	0.92

Table 7.3 Results of the vessel estimation in the 20 images of the STARE dataset (%).

The average run time of the MatLab® prototype of the whole algorithm on a Intel Pentium-M PC (1.8 GHz, 1 GB of RAM) is 60 seconds, while on a Intel Duo Core 2 PC (2.2 GHz, 4 GB of RAM) is 25 seconds.

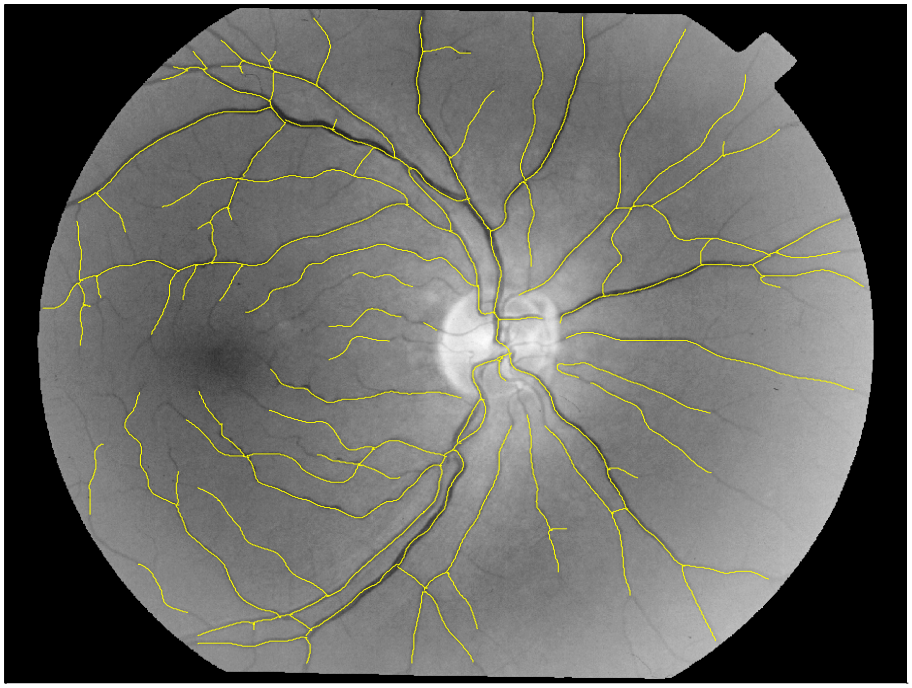


Figure 7.14 Example of vessel axis tracking results (DB60 dataset).

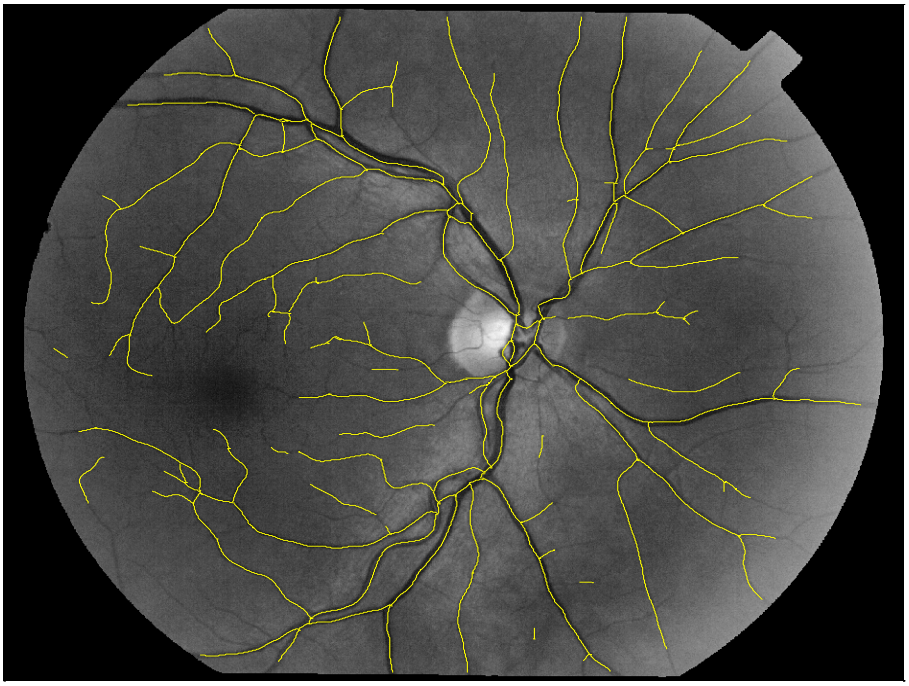


Figure 7.15 Example of vessel axis tracking results (DB60 dataset).

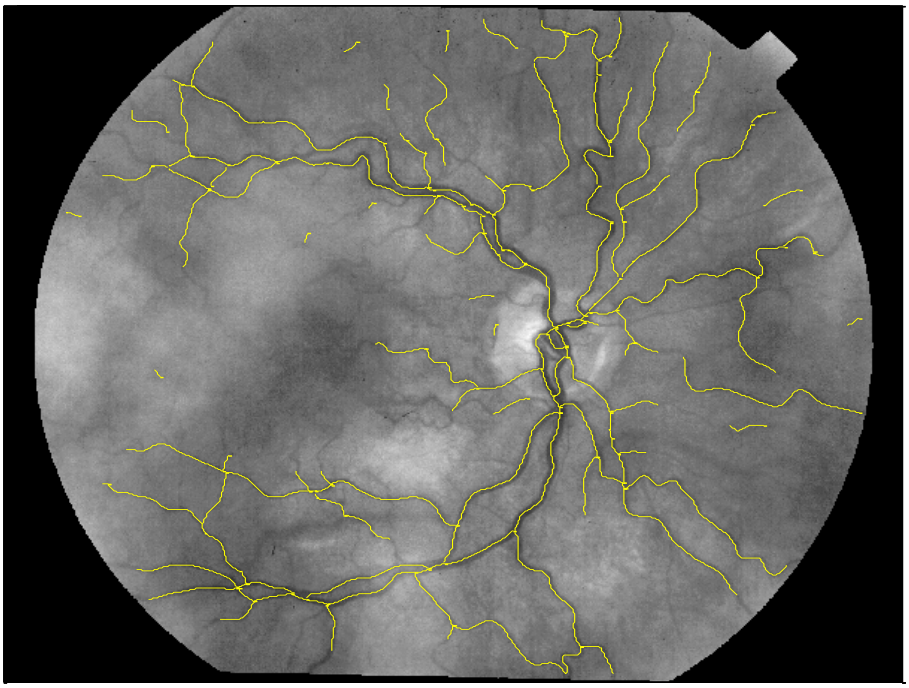


Figure 7.16 Example of vessel axis tracking results on an image containing pathology (DB60 dataset).

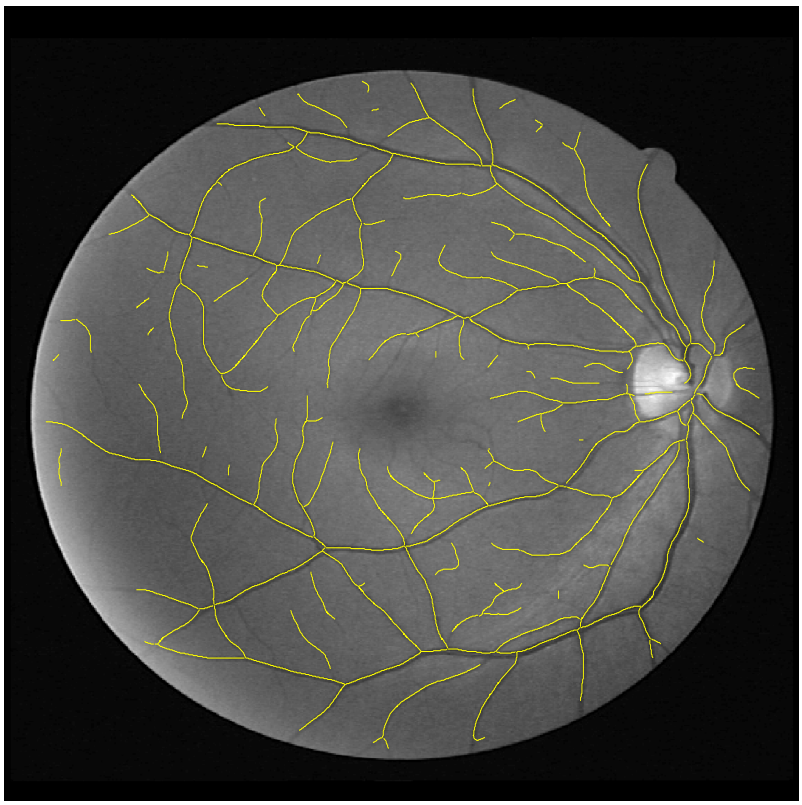


Figure 7.17 Example of vessel axis tracking results (DRIVE dataset).



Figure 7.18 Example of vessel axis tracking results (STARE dataset).

How it can be seen in Table 7.1, Table 7.2, and Table 7.3 the mean sensitivities of the method are quite different in the three datasets. This different behavior can be explained in term of the image features and the ground-truth manual labeling.

The images from different datasets have different field of view and resolution: DB60- 50°, 1400x1200 pixels; DRIVE- 45°, 768x584 pixels; STARE: 35°, 605x700 pixels. In these last two datasets, the smallest capillaries manually segmented by human observers are 1-2 pixels wide, while in DB60 the smaller capillaries manually segmented are about 3-4 pixel wide. The proposed method has not proved to be able to detect these very small vessels mainly because the seed finding procedure is not able to detect them.

Still, the DB60 dataset is the one on which the algorithm presents the highest false vessel detection, i.e. 5.18%, versus 4.82% and 3.07%. Even this behavior can be explained by the same considerations reported above. In fact, as we made the algorithm more sensible towards the small vessel of the DRIVE and STARE images, small capillaries and spurious grains not present in the ground-truth mask of DB60 were found. The false vessel detection step described in Sec. 7.3 has proved to be particularly helpful in the post-processing of the DB60 images, while its contribution has been minimal with the other two datasets.

An additional consideration can be made about the capillaries. The evaluated results are computed by comparing the length of the estimated vessel axes with the length of the ground-truth vessel mask skeletonization. Therefore, wide and narrow vessels are equivalent in the computation of the performance of the algorithm and the missed detection of a large vein brings the same error of the missed detection of a

narrow capillary with the same length. This is true of course also for the false vessel detection.

7.5 Conclusion

This chapter describes a new automatic system to extract the vessel structure in retinal images, based on a multi-directional graph search algorithm. In its present form the method has proved robust with respect to initial false positive seeds and efficient in the tracking process. Its main drawbacks are the difficulty of detecting small capillaries of 1-2 pixel diameter and the different behavior with different datasets.

Our objective was to develop a vessel segmentation method able to find the central axis of the retina vessels, leaving the detection of the vessel border to a successive step. The partition of the segmentation process in two sequential and independent tasks provides some advantages. Three considerations can be made on this issue.

First, we could use a tracking method that does not require to identify the longitudinal cross-section of the vessel and thus to detect the vessel diameters, allowing us to choose a technique that analyzes fewer pixels. The method proposed here uses the Dijkstra's algorithm, revised and expanded in order to connect multiple source points. The Dijkstra's algorithm has been widely studied, is well known, and its implementation can be highly optimized for both computational cost and memory occupancy. Since it is at the core of the tracking algorithm, the whole system benefits from its efficiency. The average run time of our MatLab® implementation of the sole multi-directional graph searching algorithm, ran on a single image is 30 seconds, using an Intel Pentium-M PC (1.8 GHz, 1 GB of RAM), and 15 seconds using an Intel Duo Core 2 PC (2.2 GHz, 4 GB of RAM).

The second consideration concerns the implementation of the edge detection algorithm, which will be described in details in the forthcoming Chapter 8. The rationale consists in employing an edge detection approach and using the vessel axis features as prior information. As will be described in Sec. 8.3.2 and Sec. 8.3.3, each point of the vessel axis is analyzed with a matched-filter technique, which exploits the information of the vessel local direction and a roughly estimated scale to reduce the dimension of the problem. Again, this approach allows sizable computational gain.

The third and last consideration involves a more general issue. In Chapter 10 we will describe an interactive user interface for the semi-automatic extraction of clinical indexes from retina images. This interface provides the user with the opportunity to select the region of interesting for the analysis, edit tracking and artery/vein classification before the computation of the clinical indexes. As far as the tracking edit tool is concerned, we decided to implement it as a modified version of the multi-directional graph search. The user who wants to add an undetected vessel (a false negative), only needs to draw a number of additional seed points in the image. At

each seed, the system displays in *quasi* real time (0–1 sec) the proposed axis of the new vessel, so the user can decide whether another seed is needed or accept the result displayed. Thanks to the way the tracking technique works, an efficient and fast procedure is provided.

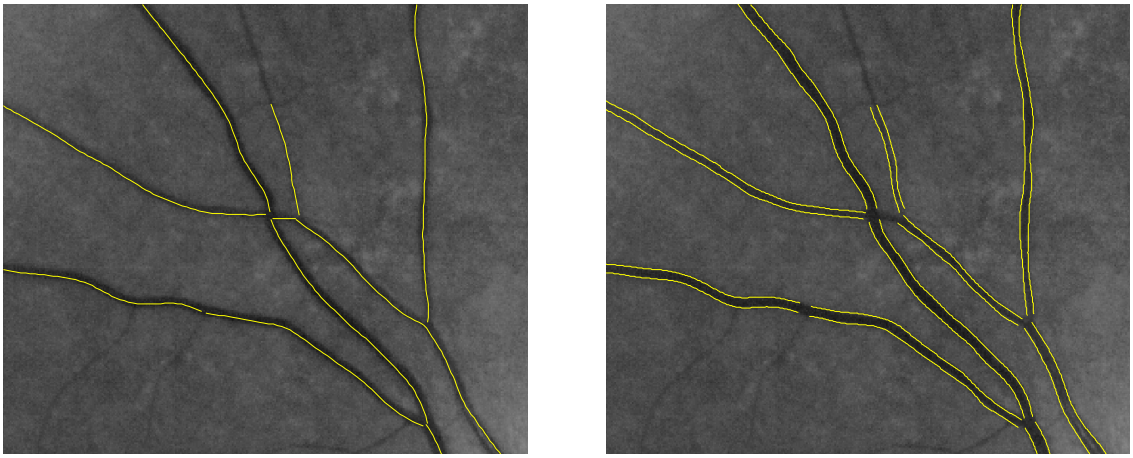
In conclusion, the satisfactory results obtained with this algorithm suggest the possibility of using it to identify the retinal vascular structures for clinical purposes.

Chapter 8

Vessel Diameter Estimation

Ocular fundus images provide important information about retinal degeneration, which may be related to acute pathologies or to early signs of systemic diseases. An automatic and quantitative assessment of vessel morphological features, such as diameters and tortuosity, can improve the clinical diagnosis and evaluation of retinopathy.

This chapter provides the description of a method to accurately evaluate vessel diameters and centerline starting from the estimated network of vessel axes. The algorithm extracts points laying on the vessel borders by means of an efficient monodimensional matched filtering approach. The orientation of the filter kernel is chosen according to the information provided by the network and the appropriate scale is computed by means of an initial diameter estimation performed on the vessels cross section profiles before the filtering process.



(a) (b)

Figure 8.1 (a) Starting network of vessel axes; (b) estimated calibers.

An adaptive correction step is then run to fix non consistent diameters, in order to obtain a regular and continuous vessel morphology. Vessel border refinement finally yields an accurate representation of the vascular structure.

Average calibers were evaluated, for a set of vessel segments, both manually by an expert and automatically by the proposed method. Comparative results show high correlation. In addition, starting from the structures assessed by the algorithm, for each processed image a binary mask has been drawn and compared with the manual segmentations available for the DB60, DRIVE, and STARE datasets.

8.1 Introduction

The morphology of the vascular structure can be affected by different abnormalities caused by acute pathologies or by early signs of certain systemic disease, such as diabetes and hypertension. Ocular fundus images can provide important information about these signs and their accurate analysis is necessary to improve clinical diagnosis of diseases. An automatic and quantitative assessment of vessel morphological features, such as diameters and tortuosity, can reveal important information on the abovementioned diseases. To this aim, the exact layout of all relevant vessels in the image must be extracted. A significant issue in fundus images is the contrast between vessel and background, which is often very poor, especially for capillaries. Digital noise represents another critical aspect and, in addition, wider vessels often present a bright reflex laying at the center (the central reflex), causing their profile to be indistinguishable from the one belonging to two narrow parallel vessels.

Matched filters have been widely used, both in their two-dimensional or mono-dimensional variant, to detect signals in presence of noise, because of the very high signal-to-noise ratio (SNR) they provide [103]. However, when applied to retinal image analysis, matched filtering requires precise knowledge of the blood vessel morphological parameters, such as thickness, orientation and shape profile, which substantially vary across the image. To circumvent this problem, multi-orientation and multi-scale approaches have been proposed: the vessel image is convolved with a set of variously oriented and scaled kernels, to get the best response.

The biggest drawback of this method is the computational time required to process the image with a high number of filters [104]. An approach proposed in literature to speed up the search for filter orientation is the use of steerable filters, such as Hessian filters [105], exhibits a major drawback in the possible overfitting of noise and of nonvascular structures. A simple solution to the unknown thickness problem may be that of choosing some effective scale that works sufficiently well for most of the vessel widths. In this case however, small-scale filters might erroneously split a wide vessel into two narrower structures. On the other hand, large-scale filters perform poorly on narrow tubular structures and might merge narrow near vessels [106].

This chapter proposes a method to accurately evaluate vessel diameters and centerline starting from an even roughly estimated vessel axis network. Each segment of the network provides the approximate direction of a corresponding vessel axis. Starting from the assumption that cross section vessel profiles can be approximated by a Gaussian shape [78], the algorithm extracts points laying on the vessel borders by means of an efficient matched filtering approach, using a discretized Laplacian of Gaussian (LOG) function as kernel. Appropriate kernel orientation and scale are preventively evaluated, in order to improve the filter precision and efficiency. A self-correcting step follows, where non-reliable border points are automatically fixed. To evaluate the performance of the method, we considered 739 vessel segments. For

every segment, we compared the average caliber calculated by manual segmentation and by our algorithm.

8.2 Materials

A set of 739 vessel segments, extracted from 3 color fundus images randomly chosen from the DB60 dataset was analyzed. Every segment considered is a portion of vessel whose extrema belong to two of the following regions: a natural vessel end point, a bifurcation, a branching, a cross. The vessels considered vessels were also manually segmented by an expert ophthalmologist, and the chosen segments span a wide range of structures: from the very wide vessels laying near the optic disk to the thin peripheral capillaries.

8.3 Methods

The system that evaluates vessel diameters and centerline is composed of several modules. The first is the preprocessing-and-profile-extraction module Sec. 8.3.1, which initially performs image enhancement [67]. Cross section vessel profiles P are then extracted along every branch of the vessel network orthogonally to the approximate axis direction.

They are then preprocessed with a mono-dimensional shift-invariant Gaussian filter, to reduce noise.

For each profile P, the edge-point-detection module (Sec. 8.3.2) carries out two tasks: a preliminary vessel width estimation is performed, which is used to set the kernel scale for the second step, consisting in a mono-dimensional matched filtering.

When a couple of candidate border points is detected for each profile, the adaptive-correction module (Sec. 8.3.3) checks their reliability. To this aim, a statistic index M is computed on the whole set of diameters of the considered vessel. Calibers that appear to be non-consistent with M are fixed by changing the matched filter scale, or forced to a trustworthy value when a reliable diameter cannot be found.

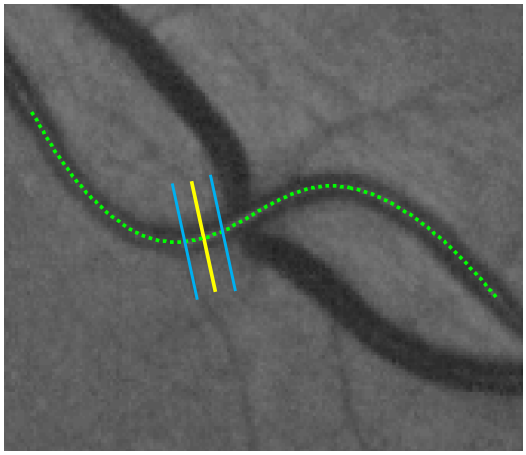
The border-refinement module (Sec. 8.3.4) is finally aimed to extract from the set of border points some regular curves delineating the final vessel edges.

In Figure 8.6 the output of the last three modules is displayed for a vessel segment where a significant central reflex is present, along with a crossing.

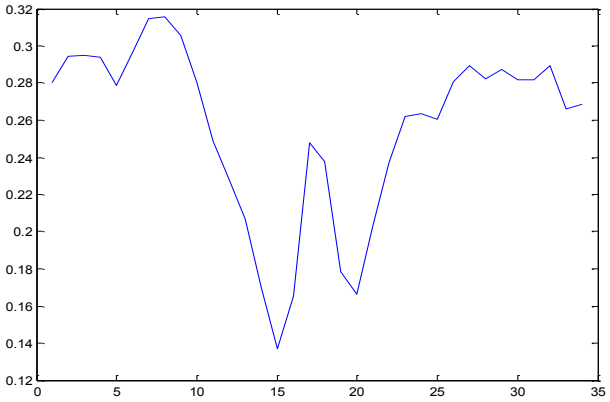
8.3.1 Preprocessing and Profile Extraction

The green component is extracted from the images, since it allows the best contrast for retinal vessels. An initial enhancement process is then applied to the whole image [67] with the aim of removing luminance and contrast drifts, to allow uniform intra- and inter-image contrast and luminosity. The intensities of the image are finally inverted so that the intensity of vessel pixels is higher, compared to the background.

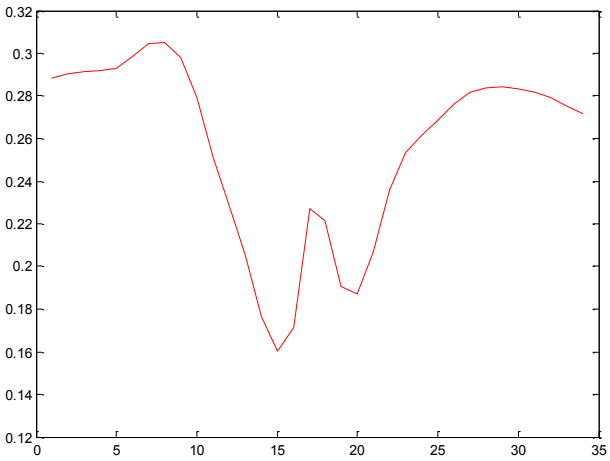
In order to perform vessel segmentation we start from the previously estimated vessel network, whose branches approximate the axis direction for every vessel segment. Every segment s of the network can be expressed in curvilinear coordinates as a curve $C_s(i),\ i \in [1, \ldots, N_s]$. At every i in $[2, N_s - 1]$ we extract a profile P_i^s orthogonal to the direction of s and centered in $C_s(i)$. In order to limit digital noise, we build P_i^s as the mean of three adjacent profiles p_{i-1}^s, p_i^s and p_{i+1}^s orthogonal to s and centered respectively in $C_s(i-1)$, $C_s(i)$ and $C_s(i+1)$. The length of every profile p_k^s and hence of P_k^s, is fixed to a value large enough to contain the widest vessel cross section. Finally, to improve the profile SNR ratio, a mono-dimensional version of the shift-invariant Gaussian filter proposed in [107] is used. This version is a combination of domain and range filtering techniques for edge-preserving smoothing. From now on we will call PF_i^s the profile P_i^s after this shift-invariant Gaussian filtering.



(a)



(b)



(c)

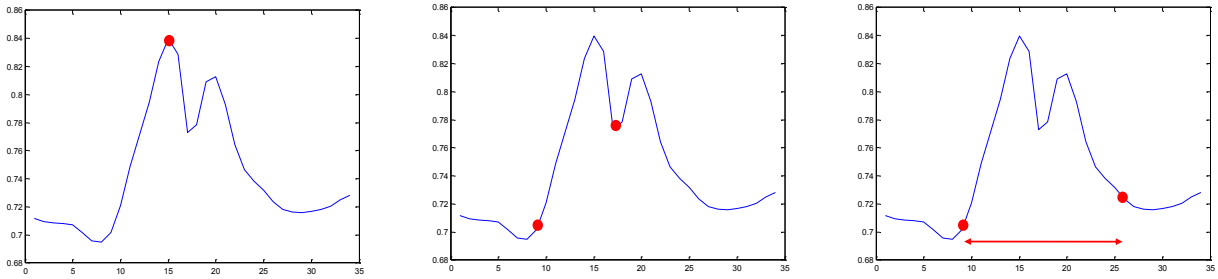
Figure 8.2 (a) Detail of an original image with the given vessel axis (green dots), the profile p_i^s of the current axis point $C_s(i)$ (yellow line), the two adjacent profiles p_{i-1}^s and p_{i+1}^s (blue lines); (b) mean P_i^s of the three profiles p_{i-1}^s, p_i^s and p_{i+1}^s; (c) The shift invariant Gaussian filtered profile PF_i^s.

8.3.2 Edge Point Detection

The task is aimed at extracting a couple of candidate border points for every profile PF_i^s obtained as described in Sec. 8.3.1.

The first step consists in estimating (even roughly) the caliber of the analyzed vessel. To this aim, the profile is initially processed with a high-pass filter to remove possible drifts at low frequencies. The diameter is then estimated starting from the maximum peak related to the center of the vessel and descending toward right and left valleys. At each iteration two points move away from the peak; the left point index li_k^s and a right one ri_k^s are determined where the slope markedly decreases with respect to its online average value.

If a central reflex is present, the vessel profile usually shows two peaks: one to the left and one to the right of the vessel centerline. In this case li_k^s and ri_k^s may stop on a valley related to the central reflex; therefore, the caliber estimation would not be correct. To overcome this problem, if the heights of li_k^s and ri_k^s are too different from each other, the highest point is moved toward the corresponding left or right terminal point of the profile, in order to reach a deeper valley.



(a) (b) (c)

Figure 8.3 A profile PF_i^s processed for the diameter estimation. (a) The red dot indicates the maximum peak related to the center; (b) the two dots indicates where the slope markedly decreases by descending toward right and left valleys; (c) the rightmost point is moved to a deeper valley, whose height is comparable to the leftmost one.

Finally, the estimated caliber EC_k^s, centered on the k-th point of the s vessel segment, is given by the distance between li_k^s and ri_k^s.

Starting from this result, candidate border points are computed by filtering the profiles PF_k^s, with a mono-dimensional matched filter. The caliber estimated as described above is used to set the kernel scale. The matched filtering consists in the convolution between PF_k^s, and a kernel function $k_{EC_k^s}(x)$. We chose a discretized LOG function defined as:

$$k_{EC_k^s c}(x) = \begin{cases} -1, & 1 < x \leq EC_k^s \\ 2, & EC_k^s + 1 < x \leq 2EC_k^s \\ -1, & 2EC_k^s + 1 < x \leq 3EC_k^s \end{cases} \tag{8.1}$$

where EC_k^s is the previously estimated scale. The final filter response is given by:

$$PFM_k^s(x) = PF_k^s(x) \otimes k_{EC_k^s}(x) \tag{8.2}$$

where $\otimes$ is the operation of convolution. Since direction and scale are adaptively computed for every single analyzed profile, we increased the matched filter efficiency. We detect possible border points for the analyzed vessel by thresholding the filtered profile PFM_k^s. Taking cue from [80], we decided to determine the threshold with a fuzzy 2-means clustering method, which has been preferred to the Otsu's method

because the first involved a smaller number of correction and forcing operation (see Sec. 8.3.3).

Fuzzy c-means (FCM) is a method of clustering which allows one piece of data to belong to two or more clusters [108]. This method is based on minimization of the following objective function:

$$J_m = \sum_{i=1}^{N} \sum_{j=1}^{C} u_{ij}^m \left\| x_i - c_j \right\|^2, \qquad 1 \le m < \infty \tag{8.3}$$

where m is any real number greater than 1 (2 in our implementation), u_{ij} is the degree of membership of x_i in the cluster j (see Figure 8.4), x_i is the ith of d-dimensional measured data, c_j is the d-dimension center of the cluster, and $\|*\|$ is any norm expressing the similarity between any measured data and the center. Fuzzy partitioning is carried out through an iterative optimization of the objective function 8.3, with the update of membership u_{ij} and the cluster centers c_j by:

$$u_{ij} = \frac{1}{\sum_{k=1}^{C} \left(\frac{\|x_i - c_i\|}{\|x_i - c_k\|} \right)^{\frac{2}{m-1}}}, \quad c_j = \frac{\sum_{i=1}^{N} u_{ij}^m x_i}{\sum_{i=1}^{N} u_{ij}^m} \tag{8.4}$$

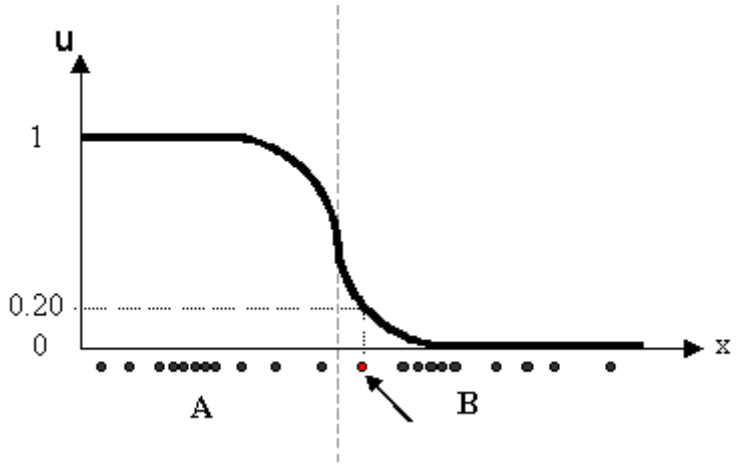


Figure 8.4 Given a certain mono-dimensional data set, suppose to represent it as distributed on an axis. Two clusters (A and B) may be identified in proximity of the two data concentrations. The datum shown as a red marked spot belongs more to the B cluster rather than the A cluster. The value 0.2 of u indicates the degree of membership to A for such datum.

This iteration will stop when $\max_{ij} \left\{ \left| u_{ij}^{(k+1)} - u_{ij}^{(k)} \right| \right\} < \varepsilon$, where ε is a termination criterion between 0 and 1, whereas k are the iteration steps. This procedure converges to a local minimum or a saddle point of J_m.

In our implementation we defined two clusters, namely “vessel” and “non-vessel”. The threshold value is the minimum x belonging to the “vessel” cluster. The value of

m was set to 2, as it is usual in the literature. Using values closer to 1 would result in crisper (i.e. non-fuzzy) partitions, while values greater than 2 would increase the fuzziness of the membership. In order to speed the convergence of FCM, we initialized it with initial cluster centers at the first and at the third quartiles of the profile. Typically, one to three iterations of FCM were adequate.

When the thresholding operation provides multiple disjoint "vessel" segments (typical when two parallel vessels with similar caliber are close - less probable but possible when a vessel with strong central reflex is filtered with an underestimated scale) the edges are extracted by evaluating, among all "vessel" segments, the nearest to the center of the profile.

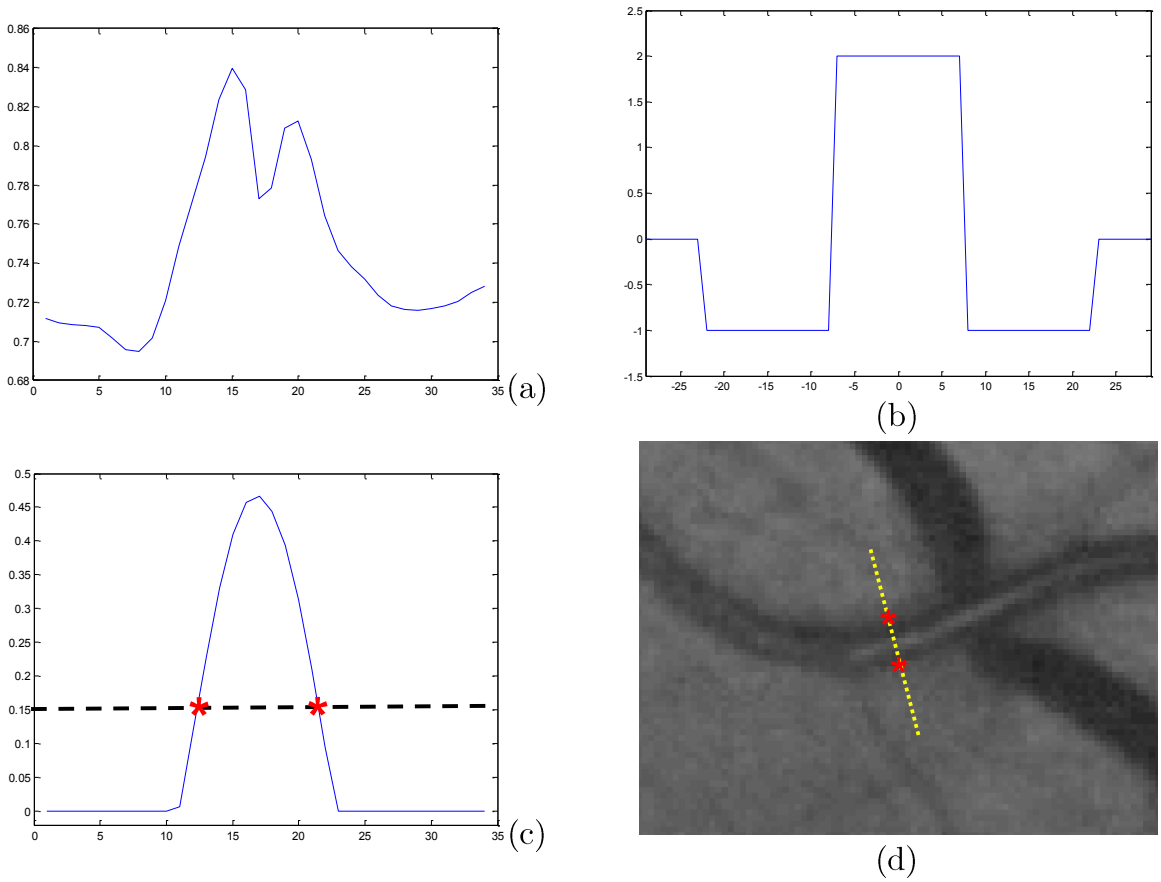


Figure 8.5 (a) The starting PF_i^s profile, (b) the kernel function $k_{EC_k^s}(x)$ centered in x=0 and with $EC_k^s = 15$ as estimated scale, and (c) the output of the matched filter, with the threshold (dashed black) chosen by using a fuzzy 2-mean clustering. The red stars represent the estimated caliber edges (c).

8.3.3 Adaptive Correction

As described in the previous sections, we processed vessel profiles averaged over three consecutive cross sections (Sec. 8.3.1), hence the analysis performed on vessels

was almost local. The major drawback of this kind of approach is that it might fail in regions where vessels are not clearly detectable with respect to the background. For example, in fundus images there might be low-contrast regions, or areas where two vessels cross or run one very near the other (or are even partially overlapped) at some intervals. Also the presence of lesions, such as hemorrhages, could partially hide vessels. In these situations, the local caliber estimation might be imprecise, causing the matched filter to use an inaccurate scale, hence potentially yielding inexact vessel border locations.

To overcome this issue, every vessel segment s is now considered at a higher level as a tubular structure, whose calibers have to satisfy some continuity and regularity constraints. The adaptive correction module checks every pair of border points (extracted as described in Sec. 8.3.2) and compares their distance to a statistic index M_s computed on the whole set of diameters evaluated for s. If the checked diameter is considerably narrower than M_s the profile is reanalyzed with a matched filter using a larger scale (2 pixels larger); likewise, if the diameter is significantly wider than M_s the filtering is performed at a smaller scale (2 pixels smaller – the minimum and maximum scales taken into consideration are respectively of 1 and 25 pixels). We therefore use for every profile the most suitable single-scale filter, while using a multiple-scale filter only for critical profiles. In this way, we improve both the matched filtering precision and efficiency. One more case is taken into account in this module, when a reliable diameter cannot be found, even after scale adjustment. If the adjusted diameter is still considerably different from the statistic index M_s, border points are forced so that their distance match M_s itself. It should be noticed that this latter approach is taken for very critical situations only, when the transition pixels from the vessel to the background cannot be locally distinguished, even after scale adjustment.

The use of the median as M_s allowed us to achieve accurate results and, at the same time, to minimize the number of forced diameters.

8.3.4 Border Refinement

For each vessel segment s, the modules described in the previous sections provide two sets of points $B1^s = \{b1_i^s,\ i = 1{:}N_{b1}^s\}$ and $B2^s = \{B2_i^s, i = 1{:}N_{b2}^s\}$ sampling the two borders of the vessel. In some regions samples might be noisy or sparse, leading to an irregular border description.

Regularity of vessel borders was achieved by means of an interpolation function. The fact that vessels are continuous structures at least with their first derivative led us to use a cubic smoothing spline interpolation. Hence two final curves $C1^s(x)$ and $C2^s(x)$ laying on the vessel borders were computed. The vessel centerline $VC^s(x)$ is the curve computed by averaging $C1^s(x)$ and $C2^s(x)$ coordinates.

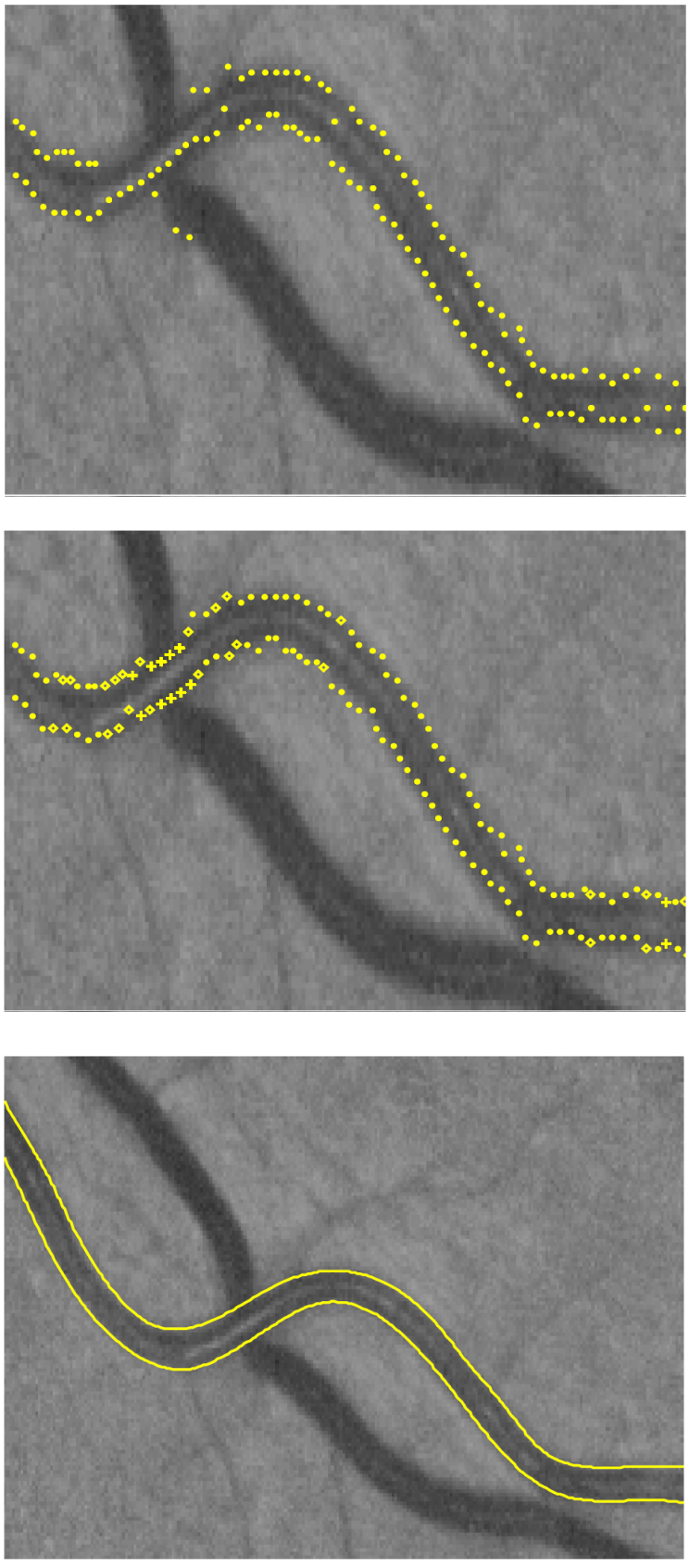


Figure 8.6 Border points evaluated before (top) and after (middle) diameter correction, along with the final vessel segmentation (bottom). In the middle image rhombus points were successfully corrected, while crosses were forced to the median caliber of the analyzed vessel segment.

8.4 Results

8.4.1 Caliber Correlation

The method has been tested by analyzing a set of 739 vessel segments that had been previously manually segmented by an expert. We obtained a vessel axis network by applying skeletonization to the binary image resulting from manual segmentation. We then ran the proposed method, to evaluate vessel diameters and centerline. The algorithm performance was assessed by computing the correlation between automatic and manual evaluation of the average caliber of the vessel segments. For the set of 739 vessel segments we obtained a correlation $\rho = 0.97$. In Figure 8.7 the scatter plot of the average caliber values, from manual vs. automatic evaluation, is shown.

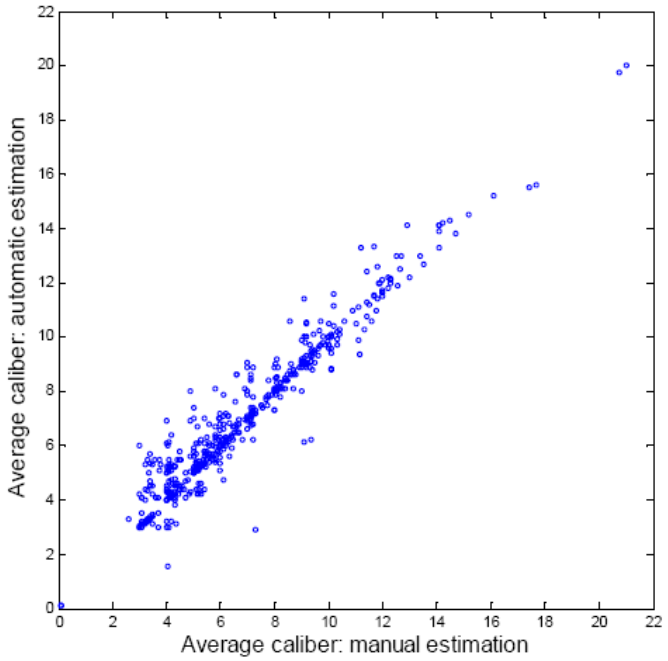


Figure 8.7 Average caliber: scatter plot of manual vs. automatic estimations

The whole evaluation required a total of 17,032 profile analyses; 4,758 of them (27.9%) needed to be processed by the adaptive correction module, in order to find a reliable diameter. 2,653 diameters were effectively recovered (55.8% of the profiles processed by the adaptive correction module), while the remaining 2,105 were forced to the median caliber evaluated on the corresponding vessel segment.

8.4.2 Mask Comparison

The proposed system for the automatic tracking of the retinal vessel network was evaluated on our own clinical dataset as well as the DRIVE and STARE databases. To perform the comparison with other retinal vessel segmentation algorithms, specificity, sensitivity and accuracy have been taken into consideration. Those three statistical measures assess the performance of a binary classification test. Sensitivity measures the proportion of vessel pixels that have been correctly identified as such, while specificity measures the proportion of background pixels that have been correctly identified. Accuracy is computed as the ratio of the number of correctly classified pixels (both vessel and non-vessel) over the total number of image pixels. The ground truth references for computing the performance measures was the manual segmentation result provided together with each database image. Table 8.1, 8.2, and 8.3 present the average accuracy, sensitivity and specificity calculated on our dataset, the DRIVE dataset, and the STARE dataset, respectively. In Table 8.2 and 8.3, performance of our method are also compared with the ones obtained by the authors who proposed the datasets [59], [60] and with the performances obtained by a second human observer (the first human observer segmentation is the ground truth reference).

	Accuracy	Sensitivity	Specificity
Our method	96.18(0.54)	82.58	97.49

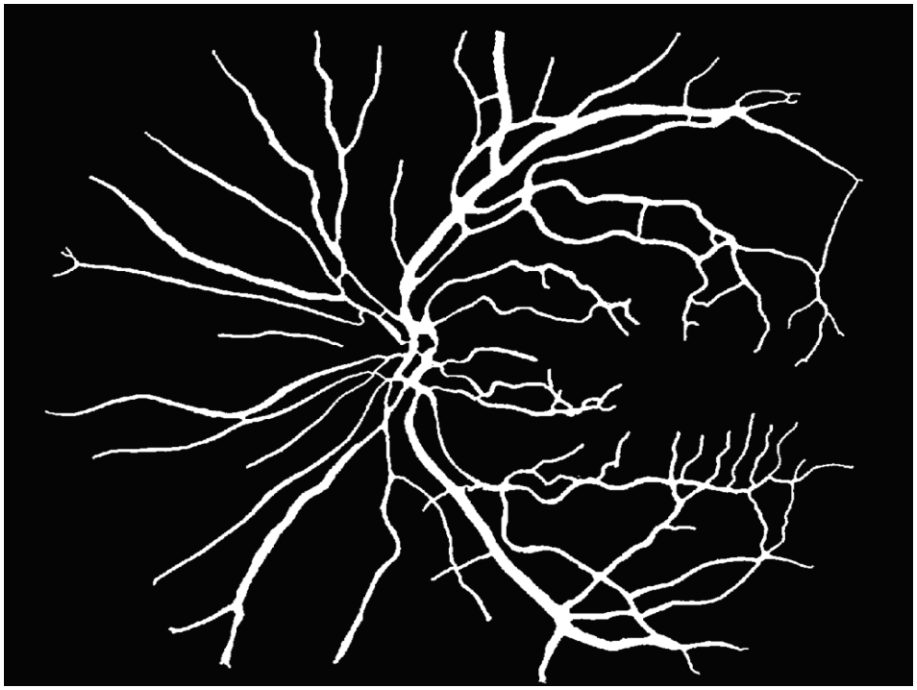
Table 8.1 Performance results of the proposed method on our dataset

Method	Accuracy	Sensitivity	Specificity
2nd human observer [59]	94.73(0.48)	77.61	97.25
Staal et al. [58]	94.42(0.65)	71.94	97.73
Niemeijer et al. [59]	94.17(0.65)	68.98	97.96
Our method	93.56(0.69)	73.04	96.62

Table 8.2 Performance results on the DRIVE dataset

Method	Accuracy	Sensitivity	Specificity
2nd human observer	93.54(1.71)	89.49	93.90
Hoover et al. [60]	92.67(0.99)	67.51	95.67
Staal et al. [58]	95.16(n.a.)	69.70	98.10
Our Method	94.01(1.60)	69.23	97.34

Table 8.3 Performance results on the STARE dataset

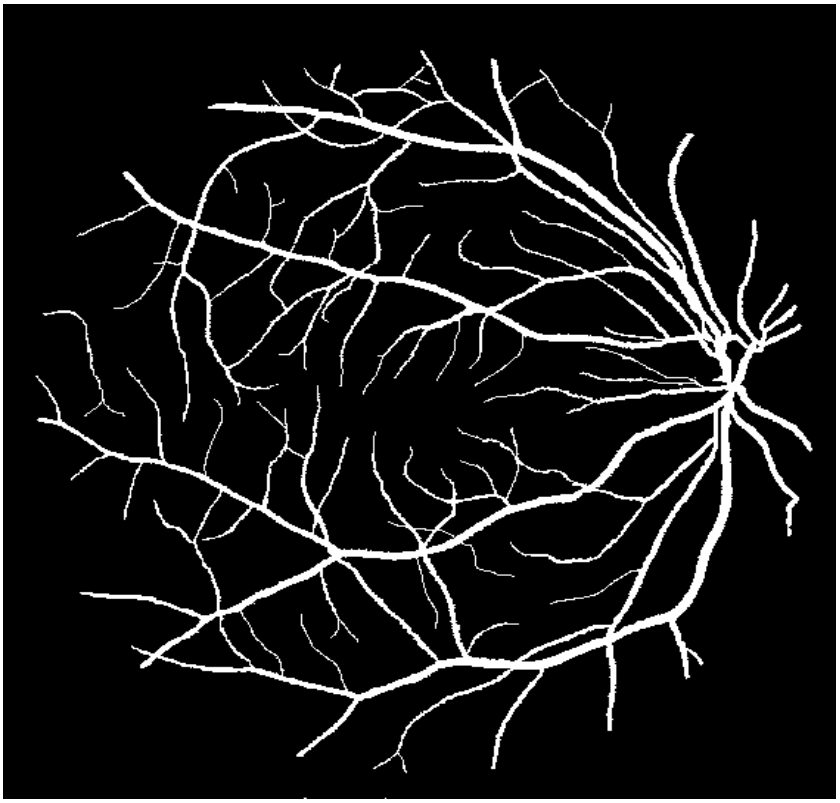


(a)

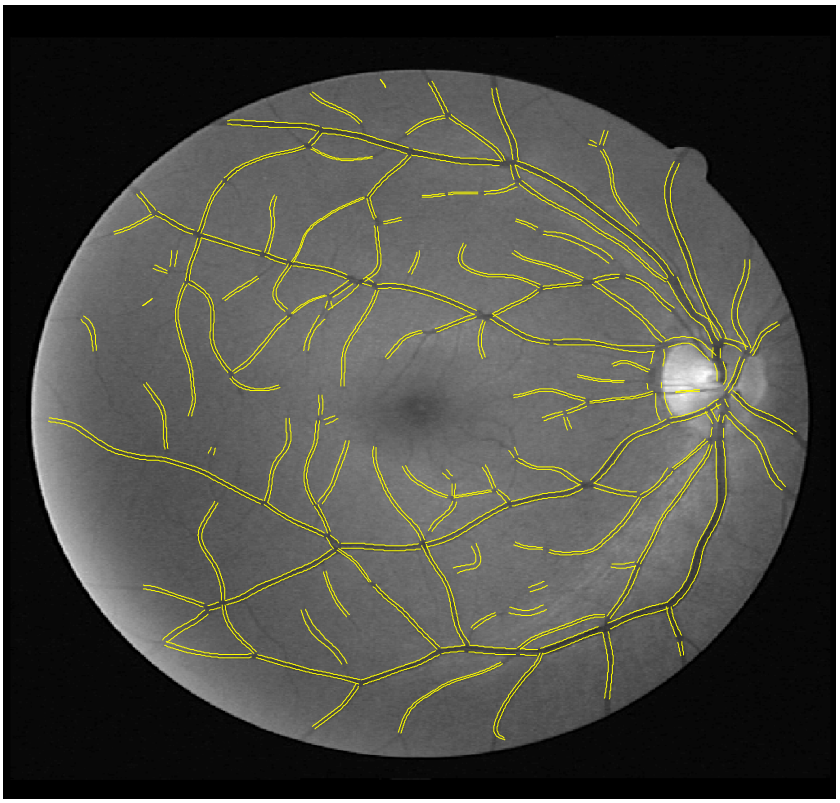


(b)

Figure 8.8 Example of segmentation result (DB60 dataset).

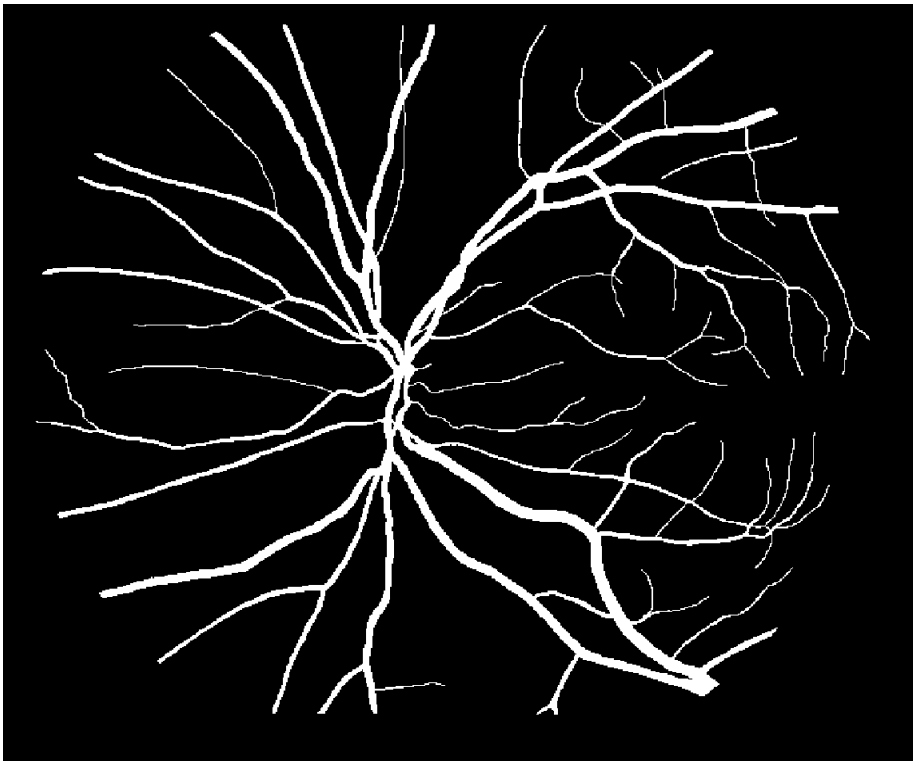


(a)

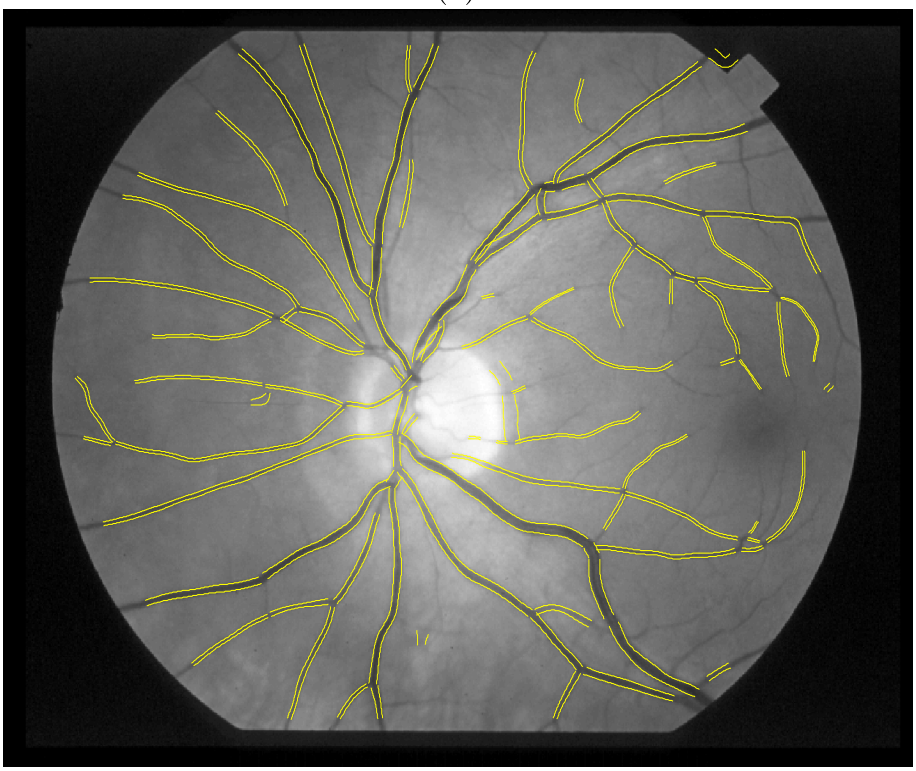


(b)

Figure 8.9 Example of segmentation result (DRIVE dataset).



(a)



(b)

Figure 8.10 Example of segmentation result (STARE dataset).

As shown in tables, the mean accuracies of the method are different in the three datasets. As already mentioned in Sec. 7.4, this behavior depends on the different image features and the differences in the ground-truth manual labeling. Since the diameter detection step operates on the vessel axis network provided by the algo-

rithm described in Chapter 7, the results are somehow correlated with the sensitivity and the specificity of the latter. However, the comparison between manual and automatic masks takes into account the actual width of the tracked vessels, and not only the detection of their presence (axis). As a direct consequence, the results are affected more by the wider vessels than by the smaller ones. As far as the DB60 dataset is concerned, the vessel axis detection shows a sensitivity of 85.86, while in the mask comparison the sensitivity is 82.58. This could suggest that, tendentially, in such database the algorithm missed more wide vessels than capillaries. In the other two datasets, the results are opposite: we have 71.37 and 66.34 of axis detection sensitivity and 73.04 and 69.23 of vessel classification sensitivity, respectively, for the DRIVE and STARE dataset.

The comparison between the automatic binary classification and the manual labeling may not be the best method to evaluate the performance of the diameter estimation step (and that is why we assessed also the diameter correlation in Sec. 8.4.1). However, it enables the performance comparison among gold standard, second human references and the performance of other algorithms (Table 8.2 and Table 8.3). In the DRIVE dataset, our algorithm shows the worst accuracy and specificity (93.56 and 96.62), even if these measures are just ~1% lower than the others. The sensitivity is ~1-4% better than the other automated methods, while it is however lower than the 2nd human observer by ~3.5%. In the STARE dataset, the performance of our algorithm is right in the middle of the other automatic method results; both accuracy and specificity, however, are slightly better than the ones obtained by the 2nd human observer.

8.5 Conclusions

This chapter describes the automatic system to extract vessel diameters from retinal images, by means of an efficient matched filtering approach. The rationale of the method consists in employing an edge detection approach that exploits the features provided by the vessel axis as prior information. Indeed, the subdivision of the segmentation process in two sequential and independent tasks has provided some saving in terms of computational load. Each point of the vessel axis is analyzed by coupling a matched technique both with the information of the vessel local direction and with a roughly estimated scale of the vessel diameter. Then, an adaptive correction step allows managing critical situations (presence of noise, lack of contrast, *etc...*) in which the algorithm may fail to detect the correct diameters.

It is worth noting that the method proposed in this Chapter strongly depends on the quality of the initial axis network: if on one hand the vessel axis information provides a prior useful to fix the filter direction and keep low the number of used scales, on the other hand a fragmented network will lead to a fragmented segmentation of vessel segments. In this case, a linking procedure would be needed to

reconstruct the complete vascular tree. A module for false vessel detection that takes into account diameter information would be useful as well to discard possible recognized segments that do not represent real vessels.

In order to assess the performance of the method, we provided two different analyses: in the first one we computed the correlation between true diameters and estimated diameters in a set of highly accurate manual segmented vessels. 739 vessel segments were analyzed to test the system, and the results were compared to the labeling provided by a human expert. Calibers estimated with the proposed method are highly correlated with those measured on the manually segmented images ($\rho = 0.97$). In the second analysis we assessed accuracy, sensitivity, and specificity of the binary classification task by comparing the automatic segmentations of the vessel network with the grand truth ones, from three different datasets. Although performances slightly differ among the different datasets, overall the method provided accuracy, sensitivity, and specificity that are comparable to the ones obtained by the 2nd human observers, as well as the ones obtained by other algorithms.

Chapter 9

Vessel Tortuosity

One of the first changes to occur in the vascular network of the retina as the consequence of a number of diseases is the increasing vessel tortuosity. In order to evaluate clinical significance of tortuosity changes with time, or to compare different levels of retinopathy, there is a strong need to develop a tortuosity measure that matches the clinical perception of ophthalmologists.

In this chapter, we start from the work done in [109] in order to define the main factors that influence the classification of a vascular structure as tortuous or non-tortuous. This is most peculiar in analyzing retinal images, in which not only straight vessels but also long vessels presenting a smooth semi-circular shape are considered as non-tortuous. Then we will focus on a formulation of *global tortuosity* that, starting from the measures of the single vessels, assesses the condition of the whole vessel network in a way that matches the clinician's grading.

The need to develop a numerical index incorporating these factors arose from the observation that previously proposed methods (see [110] for a review on the topic) failed in differentiating the tortuosity of structures that visually appeared to be very different in tortuosity, as will be shown in Sec. 9.2.

9.1 Tortuosity Properties

Vessel tortuosity measures do not have a formal clinical definition, but common practice has outlined an evaluation of the tortuosity with some well-defined properties. In order to obtain a clinically meaningful vessel tortuosity measure, i.e. a measure that is able to match the ophthalmologist's evaluation, it is necessary to make these properties explicit. Then, using a proper mathematical formulation of the tortuosity functional, the proposed measure must be shown to satisfy these properties.

9.1.1 Affine Transformations

A sound approach to extract properties of a non-formally defined index consists in performing a preliminary study on the invariance properties of such index with

respect to the most relevant transformation in the domain space. In particular, we will consider affine transformations of a vessel: translation, rotations and scaling. Translation and rotation transformations are not supposed to influence the perception of tortuosity. In fact, these transformation are related to the geographical position and orientation of the vessels in the retina, and do not alter in any way the clinical perception of tortuosity. Scaling of the single vessels does not seem to affect the clinical perception of tortuosity either. However, a warning flag must be raised in this context, since different clinicians may have different opinions about this issue. The scaling is particularly controversial when considering also the vessel caliber, but for the purpose of evaluating single vessel tortuosity, its perception can be safely considered invariant to scaling.

9.1.2 Composition

Composition properties deal with the behavior of tortuosity perception when two vessel curves are merged into a single curve, or when various segments of the same vessel, in general with different tortuosity measures, build up to give the total vessel tortuosity.

Given two adjacent continuous curves s_1 and s_2, we define the combination of the two as:

$$s_3 = s_1 \oplus s_2 \tag{9.1}$$

Since the two composing curves are supposed to belong to the same vessel, we can assume the continuity of s_3 without loss of generality. In [108], an intuitive empirical principle was proposed:

$$\tau(s_1) \leq \tau(s_2) \Rightarrow \tau(s_1) \leq \tau(s_1 \oplus s_2) \leq \tau(s_2) \tag{9.2}$$

which means that, when composing two curves, the resulting tortuosity is between those of the composing curves. The counterexample shown in Figure 9.1, top panel, clearly show that this statement cannot be accepted in con-junction with the principle of invariance with respect to rotation and scale: two curves (e.g., L_1 and L_2) perceived by themselves as almost non tortuous, when connected form an undoubtedly tortuous curve.

Therefore we propose a new composition property, such that a vessel s, combination of various segments s_i, will not have tortuosity measure less than any of its composing parts:

$$\tau(s_i) \leq \tau(s_1 \oplus s_2 \oplus \ldots \oplus s_n), \ \forall i = 1, \ldots, n \mid s_i \subseteq s \tag{9.3}$$

9.1.3 Modulation

It is useful now to express a monotonic relationship with respect to two other properties, which we will call 'frequency modulation' at constant amplitude and 'amplitude modulation' at constant frequency. It may be assumed that the greater the number of changes in the curvature sign (twist) is, the more tortuous the vessel can be considered. Similarly, the greater the amplitude (maximum distance of the curve from the underlying chord) of a twist is, the greater is the tortuosity associated with it. For two vessels having twists with the same amplitude, the difference in tortuosity varies with the number of twists φ:

$$\varphi(s_1) \leq \varphi(s_2) \Rightarrow \tau(s_1) \leq \tau(s_2) \tag{9.4}$$

and, conversely, for two vessels with the same number of twists (with the same frequency), the difference in tortuosity depends on the difference in amplitude α of the twists:

$$\alpha(s_1) \leq \alpha(s_2) \Rightarrow \tau(s_1) \leq \tau(s_2) \tag{9.5}$$

9.2 Available Tortuosity Measures

Various tortuosity measures have been proposed in the literature, but all fail in certain respects. In this section we will review the available methods for evaluating retinal vessel tortuosity, presenting some counterexamples in which these methods provide results that do not match with clinical perception.

9.2.1 Arc Length over Length Ratio

The simpler and most widely used measure of a vessel tortuosity is the ratio between its length and the length of the underlying chord [110][108], [88], [111]. The idea of using this ratio is that the greater the value of the ratio, the more distant the vessel is from a straight line, i.e., the more tortuous it is. Unfortunately, being the surface of the retina close to a semi-sphere, the non-tortuous paradigm should be the circle arc. In fact, every vessel that has a constant and small curvature, regardless of the amplitude of the arc it describes (as for the main retinal vessels), will be regarded by an ophthalmologist as characterized by negligible tortuosity. Moreover, it is shown in Figure 9.1 that two vessels with very different tortuosity have the same arc length over length ratio measure.

9.2.2 Measure Involving Curvature

Hart [108] presented a number of tortuosity measures that involve the use of the integral of the absolute curvature or of the squared curvature. For a curve $(l) = [x(l), y(l)] : D \subset \mathbb{R} \to \mathbb{R}^2, s \in C^1(\mathbb{R})$, with l the curvilinear coordinate on it, the curvature $C_s(l)$ is:

$$C_s(l) = \frac{\dot{x}(l)\ddot{y}(l) - \ddot{x}(l)\dot{y}(l)}{\sqrt{\left(\dot{x}^2(l) + \dot{y}^2(l)\right)^3}} \tag{9.6}$$

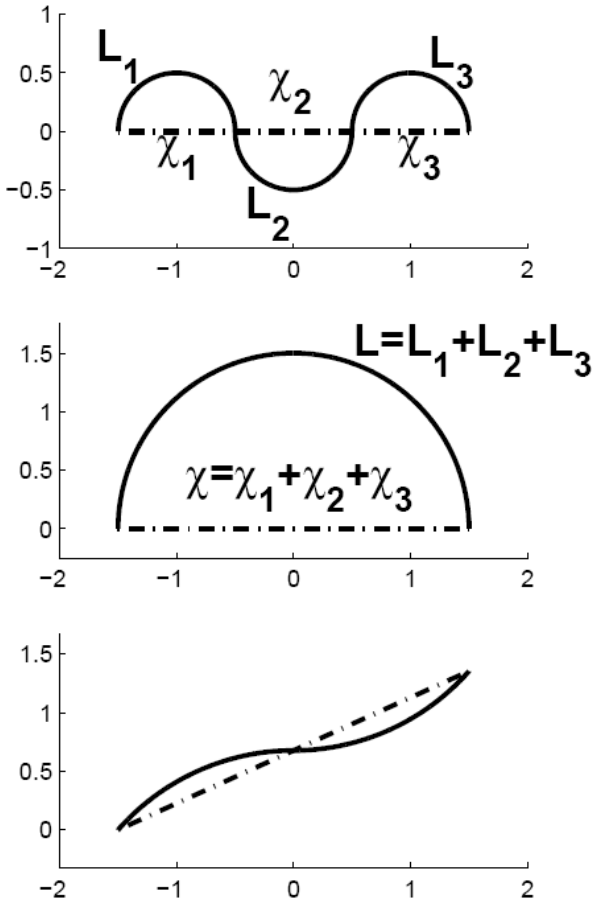


Figure 9.1 The first two curves (top and middle panel) have very different tortuosity but the same Length L and Chord Length χ. The second and last curves (middle and bottom panel) have the same average angular difference despite their different tortuosity. The curve in the bottom panel has a curvature integral of $\pi/2$ whereas the one in the middle panel has curvature integral π, even if that in the bottom panel is clearly perceived as more tortuous.

The idea behind this is that this integral should be a measure of the variability of vessel direction. However, the example presented in Figure 9.1 shows that a smaller

curvature integral may correspond to a greater perceived tortuosity. In our opinion, there are three main reasons for this result. The first is that curvature is non zero only along arcs, while it is negligible along straight or almost straight segments; but straight segments together with arcs dramatically change the tortuosity appearance. The second is that changes in convexity (curvature sign) of the curve are not taken into account, while these are instead the features predominantly taken into account by expert graders to assess tortuosity. Finally, integrating along domain, possibly different in dimension, yields to measures depending on the aforesaid dimension. The ratios between the absolute curvature integral (or the squared curvature integral) and chord length (or vessel length) have been proposed to circumvent the latter point, but still the other two problems remain open with this definition of tortuosity.

9.2.3 Mean Direction Angle Change

More recently, a measure of tortuosity based on local directional changes of the vessel has been proposed [76]. It computes the average of the angles between sample points describing the vessel. For each point i of the vessel, it computes the unit vectors from the previous *step* point d_{i-step} and to the subsequent point d_{i-step}:

$$ad_s = \frac{1}{L_c - 2\ step} \sum_{i=1}^{n} arccos\left(d_{i-step} \cdot d_{i-step}\right) \tag{9.7}$$

In addition to the high sensitivity to noise, deriving from both from the digital quantization and the vessel extraction technique, this suffers from the problems mentioned above. Even the simple example of Figure 9.1 shows that a vessel with constant curvature, such as a semi-circumference, and a vessel formed by the juxta-position of two arcs of circumference have the same average angle variation, despite their difference in tortuosity. Moreover, also herein this case vessel segments with no variation in direction do not affect the tortuosity.

9.3 Available Data

The theoretical mathematical description of the vessel is a curve in a two-dimension space:

$$s(l) : D \subset \mathbb{R} \rightarrow \mathbb{R}^2 \tag{9.8}$$

The available description of the vessel is a sampled, quantized and noise corrupted version of the theoretical curve:

$$s(k) : s(l_k) \tag{9.9}$$

where l_k is a sequence of curvilinear coordinates that represent the sampling on the original vessel.

From the DB60, 30 major arteries and 30 major veins were identified and manually sampled, in order to eliminate tracking artifacts and therefore confounding the real tortuosity measure performances.

The MEH dataset, composed by 19 images, whose tortuosity has been evaluated by an expert ophthalmologist, have been used to validate the capability of the method to discriminate different degrees of tortuosity on real application.

9.4 Vessel Representation

The sampling of a vessel may lead to a very sparse vessel description. Sparse description of the vessel further leads to a poor description of its dynamics, which may eventually fail to provide useful information on the vessel direction and on its derivatives. Sampling can be taken care of by means of an interpolation function, which describes the vessel between sampling points, where no data are present. Physiologically, vessels are structures continuous at least with their first derivative and this condition leads to the use of a cubic spline interpolation. Since the data are noisy, splines also offer the opportunity of filtering by using cubic smoothing splines.

The resulting spline curve is obtained from the available data by regularization:

$$\hat{s} = \operatorname{argmin}_{\hat{s}}\left[(1-\gamma)E_i(\hat{s}) + \gamma\left\|\hat{s} - s_q\right\|\right] \tag{9.10}$$

where $E_i(s)$ is what is called internal energy term, and represents the smoothness of the curve; γ is a weighting parameter, varying between 0 and 1, that sets the compromise between following the available data s_q and having a 'smooth' behavior. For $\gamma = 1$ $\hat{s}$ is the least square linear fit of the data, whereas for $\gamma = 0$ it is the variational cubic spline interpolant of the data. In this study we used $\gamma = 0.005$.

9.5 Tortuosity Calculation

When evaluating tortuosity, ophthalmologists integrate information about the number of vessel twists (changes in convexity, or curvature sign), and the size of the amplitude of each of the recognized twists. We would therefore decompose any curve into a set of consecutive segments of constant curvature sign. Having defined the curvature of a curve in (9.6), we define a subsegment s_i as a *turn curve* if:

$$\left[C_{s_i}(l) \geq 0,\ \forall l \in D\right] \vee \left[C_{s_i}(l) \leq 0,\ \forall l \in D\right] \tag{9.11}$$

In real images, it is common to find small oscillations (changes of convexity with very small amplitude) around the main vessel direction, due to the presence of noise. These oscillations might affect the correct decomposition of the vessel, since they would create a great number of artificial turn curves, which are not clinically significant.

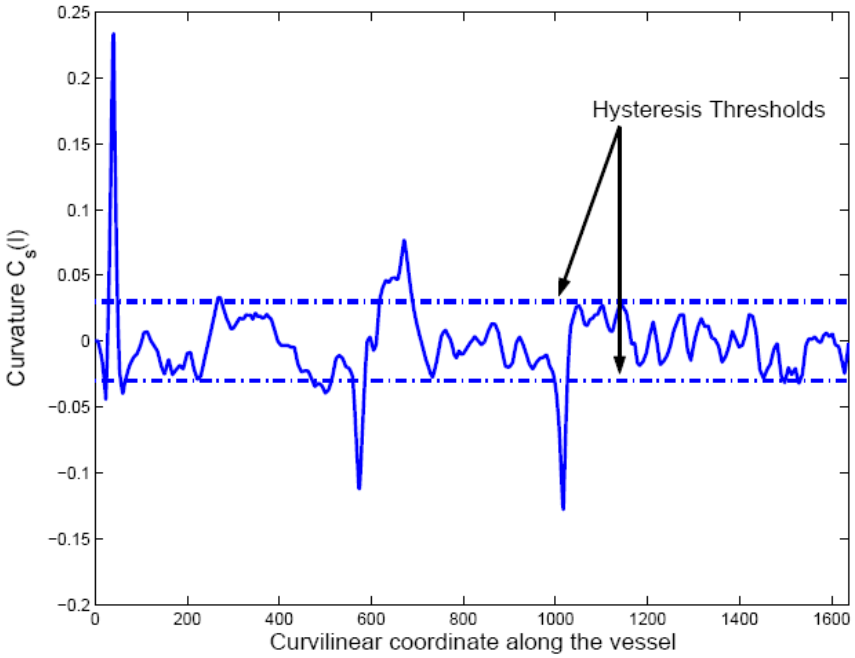


Figure 9.2 Curvature value along a vessel. The dashed lines indicate the hysteretic threshold for the convexity change.

An hysteretic threshold on curvature was thus used to deal with these small variations, as shown in Figure 9.2. To evaluate tortuosity, we also need the Chord Length L_χ of a curve, defined as the distance between the two extremes of the it:

$$L_s = \|s(\max(D)) - s(\min(D))\| \tag{9.12}$$

and the Curve Length L_c, defined as:

$$L_c = \int_{\min(D)}^{\max(D)} \left\|\frac{\partial s}{\partial l}\right\| dl \tag{9.13}$$

An hysteretic threshold of 0.03 has been set for arteries and one of 0.01 for veins. The two types of vessels have been kept separate, since ophthalmologists grade arteries and veins differently. Due to the possible presence of turn curves with zero curvature, the decomposition is not unique. Since the elimination of these turn curves

might lead to the situation in which an increase in amplitude with straight segments would not increase tortuosity, we chose to split the straight segments into two halves, assigning one to the preceding and one to the following turn curve.

9.5.1 Tortuosity: First Proposal

Once a curve $s(l)$ is divided into n turn curves

$$\mathrm{s_i} : \mathrm{s} = \mathrm{s_1} \oplus \mathrm{s_2} \oplus \ldots \oplus \mathrm{s_n} \tag{9.14}$$

a measure of vessel tortuosity can be proposed as:

$$\tau(s) = \frac{n-1}{n} \frac{1}{L_c} \sum_{i=1}^{n} \left[\frac{L_{C_{s_i}}}{L_{\chi_{s_i}}} - 1 \right] \tag{9.15}$$

This tortuosity measure has a dimension of $1/length$ and thus may be interpreted as a *tortuosity density*, allowing its comparison on vessels of different length. It is worth noting that when n is equal to 1 then τ is equal to 0 and thus vessels with a constant convexity have zero tortuosity. The proposed definition of tortuosity meets all the properties described in Sec. 9.1. In particular, the composition property is satisfied via the summation in (9.15), the amplitude modulation via the ratio of the length over the chord length for every turn curve, and the frequency modulation is taken care of both implicitly by means of the curve splitting and explicitly through the multiplicative term *n-1* in (9.15).

9.5.2 Tortuosity: Second Proposal

The tortuosity measure described in (9.15) is normalized in respect to the vessel length. This can be useful when the comparison of the tortuosity of two single vessels is needed. However, a non length-normalized formulation can be taken into consideration when an automatic tracking algorithm is employed. In this situation the vessel network could be tracked in a discontinue way and the tortuosity assessment of the short, high-tortuous vessels could be consequently underestimated. Thus, a slightly different measure of tortuosity can be employed:

$$\tau'(\mathrm{s}) = L_c\, \tau(s) = \frac{n-1}{n} \sum_{i=1}^{n} \left[\frac{L_{C_{s_i}}}{L_{\chi_{s_i}}} - 1 \right] \tag{9.16}$$

9.6 Results on Manually Tracked Vessels

The 30 arteries and 30 veins selected from the DB60 dataset have then been analyzed by an expert ophthalmologist, who ordered them on the basis of their increasing tortuosity. The vessels were manually tracked, in order to eliminate tracking artifacts and therefore confounding the real tortuosity measure performances.

The proposed method was then compared with those presented in Sec. 9.2.2, for which, calling κ the curvature of a curve, we define as in [108] the total curvature and the total squared curvature as the integral of $|\kappa|$ and $\cdot \kappa^2$, respectively. Computation of κ involves the evaluation of first and second derivatives along the curve, which was done both by numerical differentiation and by the same spline representation of the vessel used for the computation of the proposed measure τ.

$$tc = \int_{\min D}^{\max D} |\kappa(l)| dl \tag{9.17}$$

$$tsc = \int_{\min D}^{\max D} |\kappa(l)^2| dl \tag{9.18}$$

Table 9.1 shows the values of the correlation between clinician perception and all the tortuosity indexes mentioned in this chapter. The correlation is calculated on the order of vessels. In this way, possible non-uniformity in the distribution of vessel tortuosity does not influence the correlation value. These results show that the proposed measure has good correlation as regards both artery and vein tortuosity.

Tortuosity Measure	Arteries	Veins
L_c/L_χ	0.850	0.564
tc	0.889	0.741
tsc	0.863	0.707
tc/L_c	0.860	0.721
tsc/L_c	0.840	0.690
tc/L_χ	0.883	0.745
tsc/L_χ	0.863	0.707
ad	0.860	0.733
τ	0.922	0.818

Table 9.1 Correlation of the tortuosity measures ordered with the ophthalmologist tortuosity order.

9.7 Results on Automatically Tracked Vessels

The Moorfields Eye Hospital dataset consist of 26 images whose global tortuosity has been accurately estimated by an expert ophthalmologist. This evaluation envisages three degrees of tortuosity (called "1", "2", and "3") and, specifically for the level "2", three degrees of severity, namely "low", "medium", and "high".

The images have been automatically processed and the vessel network has been tracked, and the sole human intervention consisted in defining the optic disk, under which the vessels have not been taken into consideration.

Two global tortuosity values have been computed for each image: T and T'. T is the weighted mean tortuosity τ , where the tortuosity of each vessel is weighted by its caliber, while T' is the same measure obtained using τ' instead of τ.

$$T = \frac{\sum_{i=1}^{N} \tau_i c_i}{\sum_{i=1}^{N} c_i} \tag{9.19}$$

$$T' = \frac{\sum_{i=1}^{N} \tau'_i c_i}{\sum_{i=1}^{N} c_i} \tag{9.20}$$

where $N = N(I)$ is the number of vessel in the image I, and c_i the average caliber of the vessel $i \in \{1, 2, \ldots, N(I)\}$.

In order to allow the comparison of the class assigned by the expert to each image with the index of global tortuosity estimated by algorithm, we translated the class labels into number values by following the indications of the expert himself, so that the labels "1", "2-low", "2-mid", "2-high", and "3" corresponds respectively to the values 1, 1.5, 2, 2.5, and 3.

The Figure 9.3 shows the plot of the global tortuosity value computed by the algorithm by employing the T' formulation vs. the manually-assigned tortuosity degree. In the same plot, for a better interpretability of the results, a regression line is superimposed (r=0.861) together with the horizontal lines corresponding to margins that could provide a classification by using the estimated tortuosity. Ideally, only two examples would be not correctly classified. The problems seem to be related to the poor discriminability among the degrees of severity of the class "2".

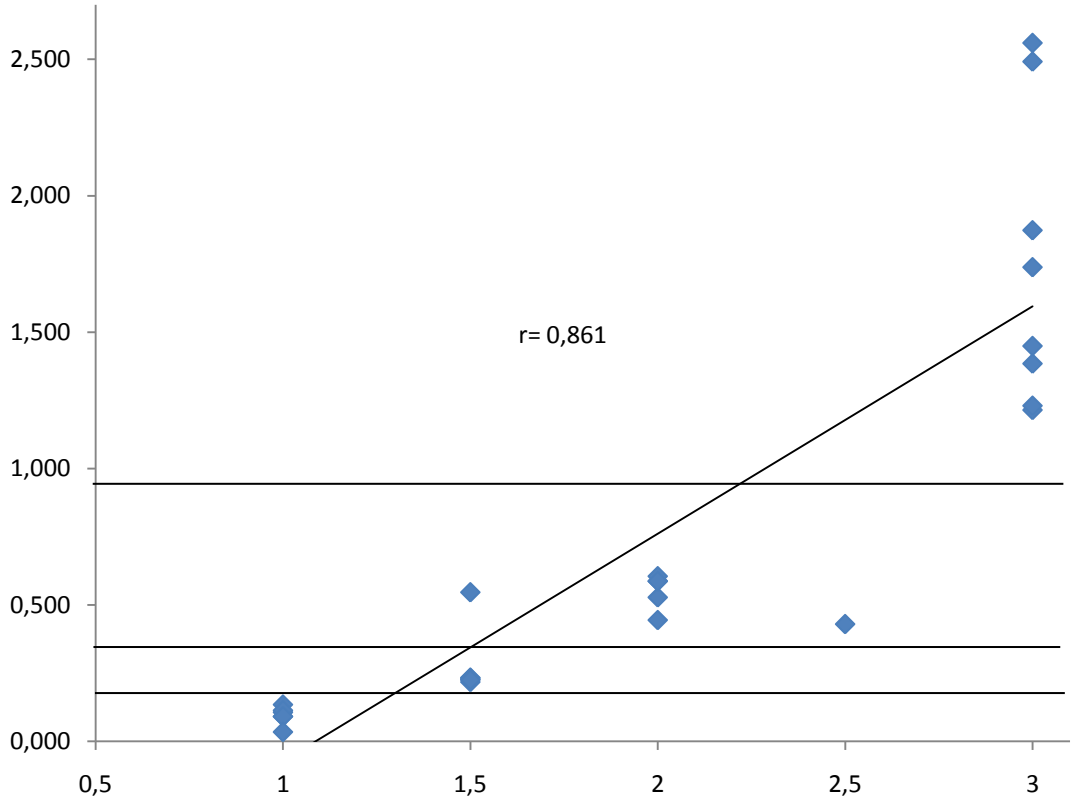


Figure 9.3 Global tortuosity value computed by the algorithm by employing the T' formulation vs. the human assigned tortuosity degree. For a better interpretability of the results, a regression line is superimposed (r=0.861) together with ideal horizontal lines corresponding to margins that could provide a classification by using the estimated tortuosity.

As the T formulation is concerned, results are similar to the ones obtained with the T' formulation. As can be seen in Figure 9.4, in this case seven examples would be not correctly classified, although the T formulation of the global tortuosity shows a correlation of 0.876 with the values assigned to the tortuosity classes (0.861 by employing T'). With a correlation that is slightly better than the one obtained with the T' formulation, the T formulation provides a poor discriminability between the classes "1" and "2-low" and the classes "2-low" and "2-mid" (Table 9.2).

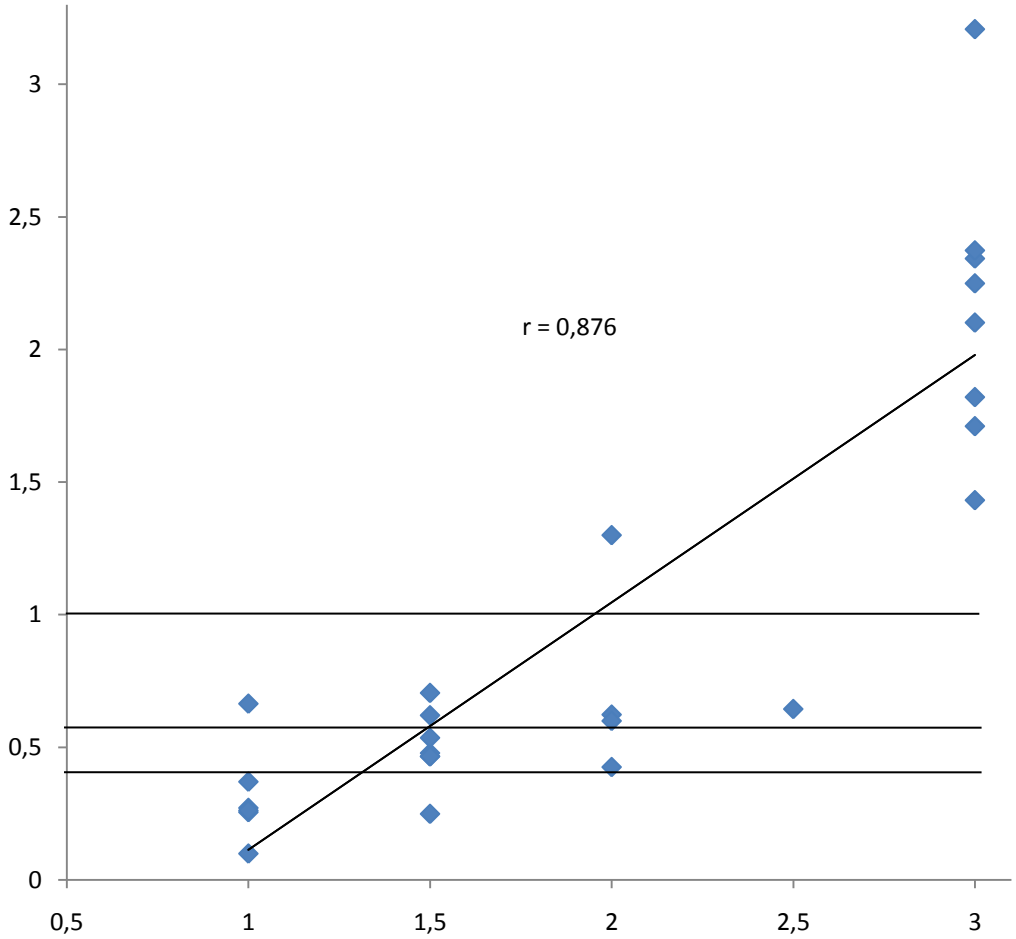


Figure 9.4 Global tortuosity value computed by the algorithm by employing the T formulation vs. the human assigned tortuosity degree. For a better interpretability of the results, a regression line is superimposed (r=0.876) together with the ideal horizontal lines corresponding to margins that could provide a classification by using the estimated tortuosity.

Image	Level of tortuosity	Degree of severity for the group "2"	Estimated Global Tortuosity (T formulation)	Estimated Global Tortuosity (T' formulation)
1	1		0.099	0.134
2	1		0.255	0.106
3	1		0.262	0.091
4	1		0.271	0.113
5	1		0.370	0.091
6	1		0.664	0.034
7	2	low	0.249	0.217
8	2	low	0.434	0.226
9	2	low	0.465	0.233
10	2	low	0.478	0.546
11	2	low	0.536	0.231
12	2	low	0.621	0.225
13	2	low	0.705	0.528
14	2	mid	0.425	0.587
15	2	mid	0.599	0.444
16	2	mid	0.623	0.605
17	2	mid	1.300	0.587
18	2	high	0.644	0.430
19	3		1.436	1.449
20	3		1.711	1.214
21	3		1.820	1.230
22	3		2.101	1.384
23	3		2.249	1.873
24	3		2.343	1.738
25	3		2.373	2.560
26	3		3.257	2.491

Table 9.2 To each image of the MEH dataset corresponds the tortuosity level assigned by the expert, accompanied with the severity degree as far as the class "2" is concerned). In the rightmost column, the global tortuosity computed by the algorithm.

Chapter 10

Clinical Usability of the Proposed Software for the AVR Estimation

The Arteriolar-to-Venular diameter Ratio (AVR), a parameter derived from vessel caliber measurements in a specific region of retinal images, is used as a descriptor of generalized arteriolar narrowing, an eye fundus sign often seen in patients affected by hypertensive or diabetic retinopathies.

The manual computation of the AVR is a tedious process, involving repeated measurements of the diameters of all arterioles and venules in the region by human graders. To facilitate large-scale clinical use, an accurate, a rapid and efficient system to compute AVR is required. Tramontan et al. [63] developed a procedure to achieve this goal: at first the vessel network has to be traced and their calibers estimated; then, in the region of interest for the estimation of the AVR, vessels are classified as either arteries or veins and the CRAE, CRVE, AVR parameters are computed.

In order to assess the capability of our vessel tracking algorithm to provide useful information for the estimation of the mentioned clinical parameters just mentioned, we integrate it with the procedure described in [63].

The system has shown good performances in the 38 images of the UoW dataset (DCCT and ETDRS). The provided results have been compared with the measures obtained by the trained and proved personnel who have worked on the subject, resulting in a good correlation.

10.1 Introduction

An early detection of serious cardiovascular diseases can be provided by the analysis of microvasculature health status. The capillary network in the retina, an important example of such microvasculature, can be readily imaged and assessed using a normal fundus camera.

In retinal images, a sign that has proved to be related to cardiovascular diseases is the generalized arteriolar narrowing, usually expressed by the Arteriolar-to-Venular diameter Ratio (AVR). The AVR is computed from the CRAE (Central Retinal Artery Equivalent) and CRVE (Central Retinal Venular Equivalent) values. These in

turn are derived from the individual arteriolar and venular calibers, which are measured in a standard area (ROI) centered on the optic disc (OD) and from half-disc to one disc diameter from the OD margin [64]. The manual procedure requires the long and cumbersome measurement of the required vessel calibers (more than 15 minutes per image on average). To overcome this problem, computer-assisted procedures have been proposed ([112], [113]) which require some degree of user assistance. The semiautomatic tool we chose to integrate the vessel tracking algorithm with [63], gives to the user the opportunity to edit tracking and artery/vein classification errors before the computation of the AVR.

10.2 Methods

The procedure to derive the AVR index requires several steps to be performed. The network of retinal vessel is traced using the method described in Chapter 7 and Chapter 8, while the OD position and diameter have been manually identified. With this information, the specific area in which caliber measurements have to be done is identified. Inside this area, vessels are labeled as either arteries or veins and their calibers are measured. In order to ensure the highest reproducibility of the assessment of the parameters of interest [114], the six arteries and the six veins with highest caliber among all the tracked vessels are selected and considered along their length until a bifurcation occurs. Finally, caliber measurements are used to compute AVR, according to the formula proposed in [114].

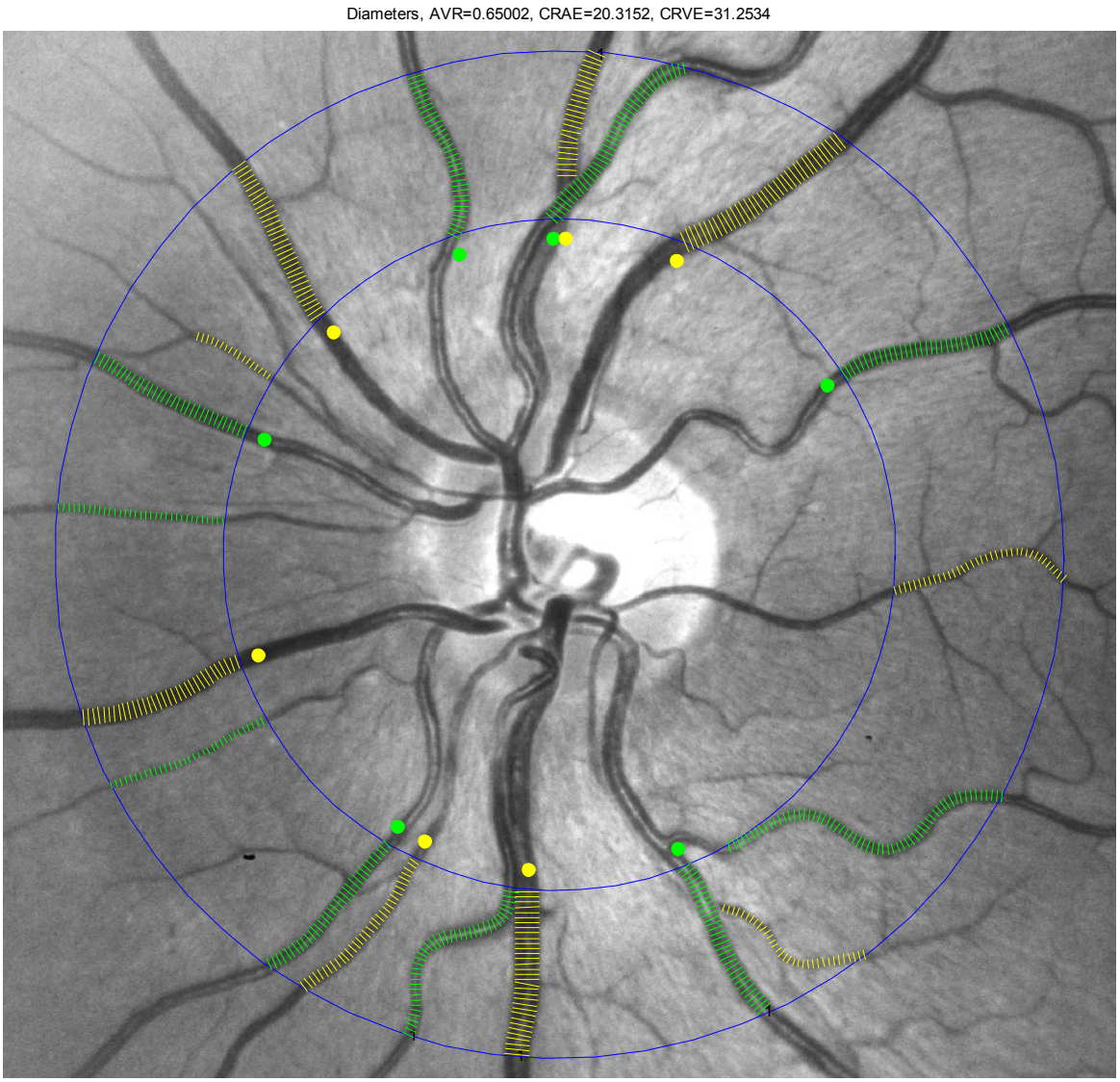


Figure 10.1 The image shows the estimated vessel diameters for all the tracked vessels in the area of interest. The 6+6 vessels used for the actual computation of parameters are labeled with small circles (green or yellow to identify arteries or veins). The underlying retinal image is the green component of the original color image.

10.2.1 Artery/Vein Discrimination

As arteriolar and venular calibers need to be separately measured to derive the AVR, each tracked vessel inside the ROI must be correctly labeled as being either an artery or a vein. For this classification the red contrast is used, a parameter related to the central reflex, which is more evident in arteries than in veins, and from it the probability of the vessel to belong to the "vein" class is derived (the probability of

belonging to the "artery" class is one minus the probability of belonging to the "vein" class).

All the vessels whose probability of belonging to one of the two classes is less than 0.8 (and then more than 0.2 for the opposite class), and that have a diameter greater than 45 μm, are considered "uncertain" and are consequently submitted to the user, who confirms or rejects the proposed classification.

10.2.2 AVR Estimation

From the caliber estimated by our algorithm (Chapter 8) and the classification provided by the method described above, the Central Retinal Artery Equivalent (CRAE) and the Central Retinal Vein Equivalent (CRVE) parameters can be computed, together with the AVR parameter

$$AVR = \frac{CRAE}{CRVE} \tag{10.1}$$

which provides a useful clinical measure as an indicator of generalized arteriolar narrowing [64], [114].

10.3 Results

The methodologies described in this Chapter have been tested in two stages: the first focused on the reliability of the tracking results while the second focused on the efficiency of the whole process to assess the AVR parameters.

In the first analysis (Sec. 10.3.1), in order to attain the best assessment as regards the usability of the tracking algorithm, the graders were asked to edit the tracking results only if major vessels were not identified. The user interaction session had to focus on speed and the tracking imperfections (such as diameter under- or over-estimations) were ignored. As far as artery/vein classification correction is concerned, no correction limitation was enforced. The results have been compared with the measures obtained by the well trained personnel from the University of Wisconsin (UoW).

In a second analysis (Sec. 10.3.2), the graders were allowed to edit the tracking results at their will: in this case the human interaction session focused on providing the best vessel segmentation, resulting in a more time-consuming process than the previous above mentioned. The correlations among UoW grading and the results obtained by three graders who used our proposed framework have been computed, in order to assess the measure repeatability of the whole system.

10.3.1 Limited Intervention Setup

The reference values against which the computer estimations have been compared were performed by the experts at the Department of Ophthalmology & Visual Sciences, University of Wisconsin-Madison. As regards the ETDRS images, they supplied us with the ARV parameters, while the DCCT set was accompanied with the AVR, CRAE, and CRVE evaluations.

Table 10.1 reports the reference and the estimated CRAE, CRVE and AVR values, for the 20 images composing the DCCT set. Their scatter plot with the corresponding correlation is shown in Figure 10.2, Figure 10.3, and Figure 10.4.

Table 10.2 reports the reference and the estimated AVR values, for the 18 images of the ETDRS set. Their scatter plot with the corresponding correlation is shown in Figure 10.5.

DCCT Image	ground truth CRAE	estimated CRAE	ground truth CRVE	estimated CRVE	ground truth AVR	estimated AVR
1	158.16	145.76	238.23	235.69	0.66	0.62
2	144.23	142.34	248.19	241.22	0.58	0.59
3	146.59	147.64	248.83	242.09	0.59	0.60
4	136.41	128.16	250.87	251.02	0.54	0.51
5	161.00	148.01	243.81	236.01	0.66	0.63
6	161.35	147.38	217.40	208.91	0.74	0.71
7	156.03	139.00	202.00	195.05	0.77	0.71
8	156.03	151.42	216.86	223.36	0.72	0.68
9	145.20	143.44	197.64	197.96	0.73	0.72
10	124.58	126.79	176.45	177.86	0.71	0.71
11	151.32	141.67	199.98	198.03	0.76	0.71
12	171.73	156.38	226.80	228.69	0.76	0.68
13	164.98	169.99	256.76	248.28	0.64	0.68
14	160.37	157.37	218.49	228.51	0.73	0.69
15	137.19	134.41	208.64	204.42	0.66	0.66
16	179.24	170.54	241.75	229.25	0.74	0.74
17	176.88	170.19	254.35	256.55	0.70	0.66
18	156.88	152.23	238.43	227.04	0.66	0.67
19	155.48	154.69	189.28	184.55	0.82	0.84
20	147.48	144.58	246.64	248.50	0.60	0.58

Table 10.1 For each of the 20 DCCT images, both the reference and the estimated CRAE, CRVE, and AVR values are listed.

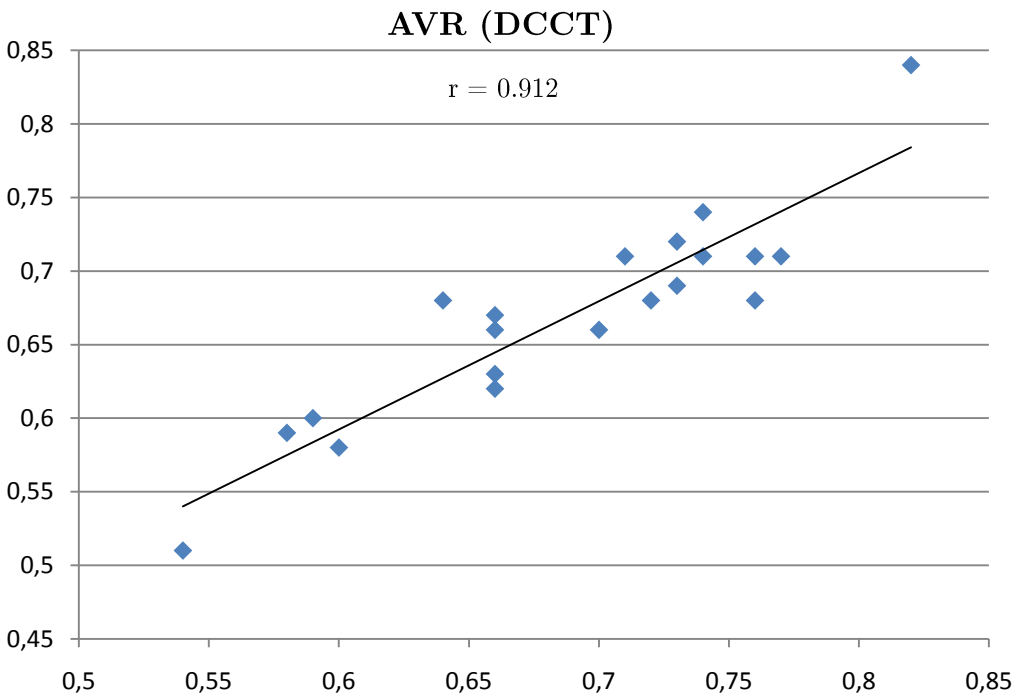


Figure 10.2 Scatter plot of the reference and estimated AVR values.

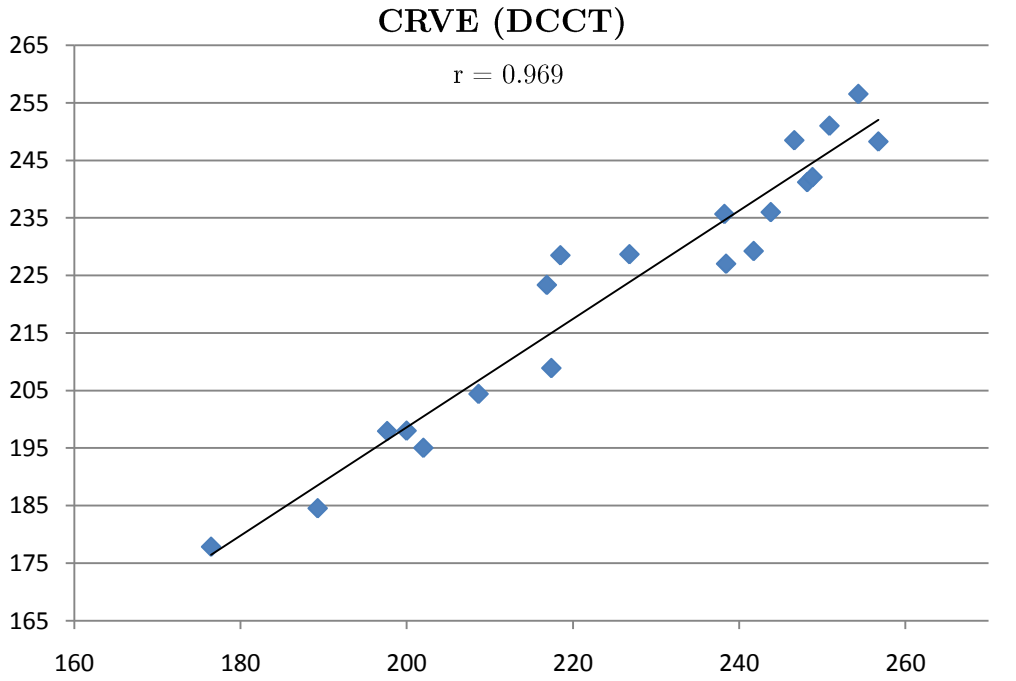


Figure 10.3 Scatter plot of the reference and estimated CRVE values.

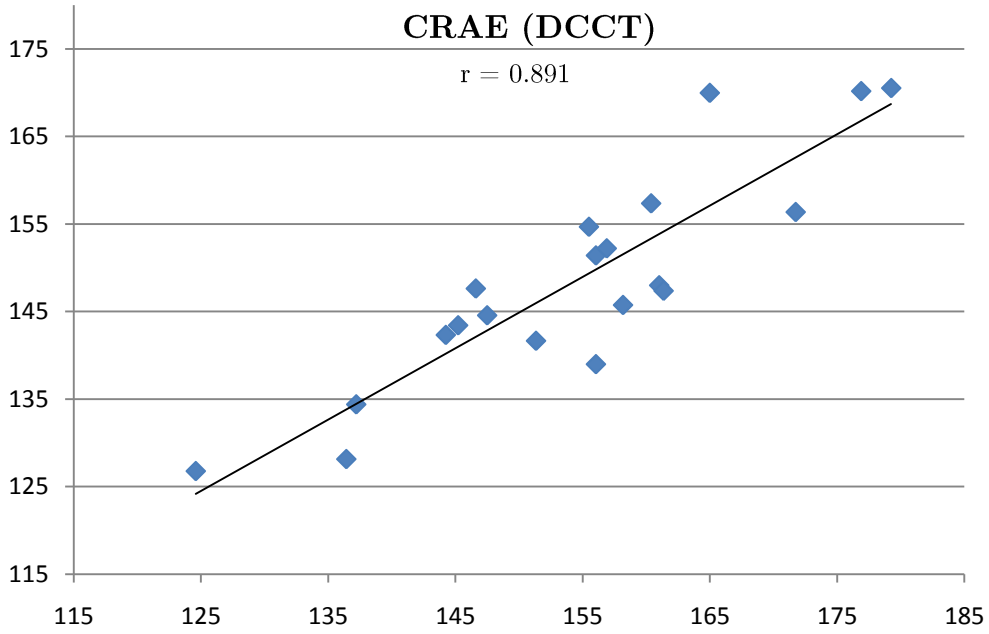


Figure 10.4 Scatter plot of the reference and estimated CRAE values.

Image	ground truth AVR	estimated AVR
1	0.64	0.67
2	0.51	0.55
3	0.68	0.65
4	0.71	0.72
5	0.82	0.85
6	0.71	0.71
7	0.69	0.71
8	0.53	0.52
9	0.60	0.62
10	0.66	0.64
11	0.71	0.72
12	0.55	0.58
13	0.74	0.67
14	0.45	0.52
15	0.60	0.61
16	0.64	0.65
17	0.54	0.53
18	0.75	0.76

Table 10.2 For each of the 18 ETDRS images, both the reference and the estimated AVR value are listed.

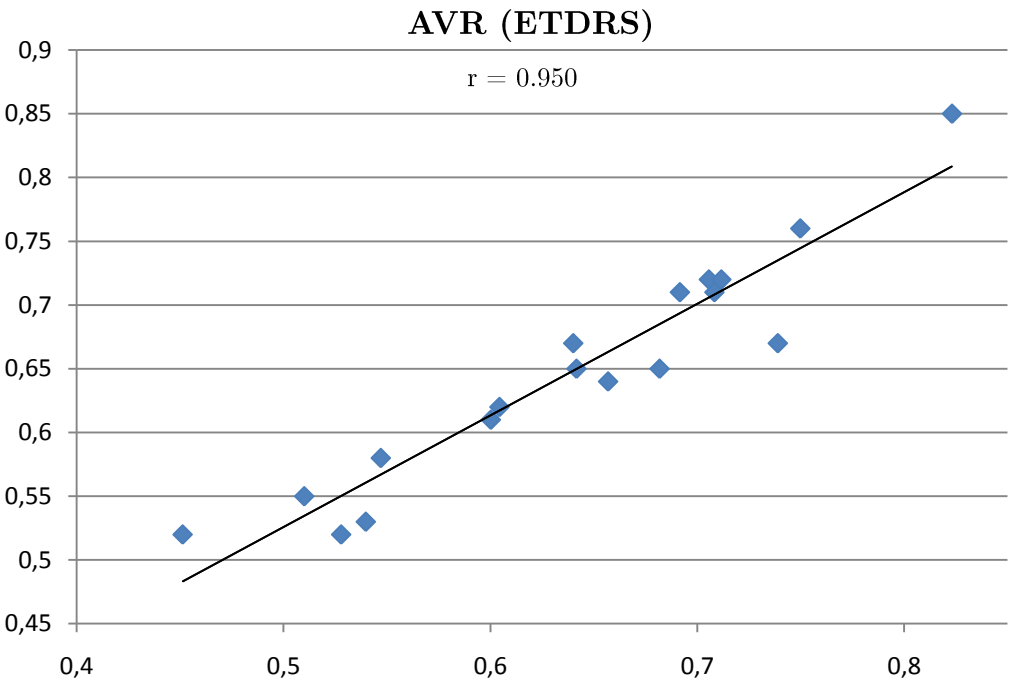


Figure 10.5 Scatter plot of the reference and estimated AVR values.

The AVR values estimated by the computer procedure are quite close to the ones provided by the manual one.

The average running time of the Matlab® prototype on a Pentium-M PC (1.8 GHz, 1 GB of RAM) was about 60 seconds for the vessel tracking procedure and 90 seconds for the whole procedure of ROI selection, tracking correction, artery/vein classification, and AVR estimation. The time is about six times shorter than the average time needed for a manual estimation of the AVR (roughly 15 minutes vs. 150 seconds).

This achievement, combined to good correlation attained, suggests the possible application of the system to the AVR parameter estimation for clinical diagnostic purposes.

10.3.2 Full Intervention Setup

In this second analysis, we have relaxed the tracking correction constraints, so that the three graders (A, B, and C) could freely edit the vessel tracking mistakes, with the aim of providing the best possible vessel segmentation. We compared the correlation among the UoW grading and the results obtained by the three graders on the DCCT dataset.

Table 10.3 reports the CRAE, CRVE and AVR values assessed by the UoW grader as well as the three graders A, B, and C, for the 20 images of the DCCT dataset. At the bottom of Table 10.3, the correlations among the four graders are provided.

DCCT image	CRAE				CRVE				AVR			
	UoW	**Grader A**	**Grader B**	**Grader C**	**UoW**	**Grader A**	**Grader B**	**Grader C**	**UoW**	**Grader A**	**Grader B**	**Grader C**
1	158.16	137.96	143.91	145.36	238.23	230.06	230.6	236.59	0.66	0.60	0.62	0.61
2	144.23	138.86	138.30	137.3	248.19	240.29	230.58	248.96	0.58	0.58	0.59	0.55
3	146.59	142.69	149.91	146.66	248.83	244.65	245.89	253.8	0.59	0.58	0.59	0.57
4	136.41	122.32	123.49	130.45	250.87	243.38	241.42	250.18	0.54	0.50	0.51	0.52
5	161.00	148.04	142.38	149.44	243.81	234.68	229.72	240.78	0.66	0.63	0.62	0.62
6	161.35	149.54	151.03	150.73	217.40	208.76	218.27	216.58	0.74	0.72	0.69	0.7
7	156.03	138.49	135.43	137.51	202.00	198.46	194.78	195.56	0.77	0.70	0.69	0.7
8	156.03	153.11	156.36	151.08	216.86	214.46	215.63	213.43	0.72	0.71	0.72	0.71
9	145.20	143.15	145.27	142.88	197.64	198.61	198.54	198.21	0.73	0.72	0.73	0.72
10	124.58	128.12	125.80	128.58	176.45	179.45	178.79	179.45	0.71	0.71	0.70	0.72
11	151.32	143.00	137.52	138.25	199.98	200.91	198.68	201.32	0.76	0.71	0.69	0.69
12	171.73	144.26	149.34	158.18	226.80	221.63	221.52	236.57	0.76	0.65	0.67	0.67
13	164.98	158.06	161.84	165.14	256.76	242.82	254.76	258.79	0.64	0.65	0.64	0.64
14	160.37	156.09	154.70	153.90	218.49	218.63	226.60	219.50	0.73	0.71	0.68	0.70
15	137.19	133.70	128.13	127.47	207.00	205.22	206.31	206.89	0.66	0.65	0.62	0.62
16	179.24	162.87	163.43	163.95	241.75	241.29	239.54	243.10	0.74	0.67	0.68	0.67
17	176.88	167.63	169.68	171.64	254.35	250.61	256.04	254.90	0.70	0.67	0.66	0.67
18	156.88	148.37	152.27	148.37	238.43	234.84	233.65	224.61	0.66	0.63	0.65	0.66
19	155.48	149.85	150.27	150.24	189.28	186.64	183.53	181.64	0.82	0.80	0.82	0.83
20	147.48	137.78	136.75	137.16	246.64	244.63	240.93	249.19	0.60	0.56	0.57	0.55

CORRELATIONS

	Grader A	**Grader B**	**Grader C**		**Grader A**	**Grader B**	**Grader C**		**Grader A**	**Grader B**	**Grader C**
UoW	0.85	0.84	0.91	**UoW**	0.99	0.97	0.98	**UoW**	0.92	0.91	0.92

	Grader A	**Grader B**	**Grader C**		**Grader A**	**Grader B**	**Grader C**		**Grader A**	**Grader B**	**Grader C**
Grader A	1.00	0.96	0.92	**Grader A**	1.00	0.97	0.98	**Grader A**	1.00	0.97	0.97
Grader B	0.96	1.00	0.96	**Grader B**	0.97	1.00	0.96	**Grader B**	0.97	1.00	0.98
Grader C	0.92	0.96	1.00	**Grader C**	0.98	0.96	1.00	**Grader C**	0.97	0.98	1.00

Table 10.3 CRAE, CRVE and AVR values assessed by the UoW, A, B, and C, graders for the DCCT dataset. At the bottom, the correlations among the four graders are provided.

The overall repeatability between users and with respect to the UoW grading were assessed by the correlation coefficients. The correlation ranges between UoW grading and the non-qualified users are 0.85-0.91 for CRAE, 0.97-0.99 for CRVE, and 0.91-0.92 for AVR. The correlation ranges between the three users are 0.92-0.96 for

CRAE, 0.96-0.98 for CRVE, and 0.97-0.98 for AVR. The total time required to analyze one image was on average 5 min (range 2-8 minutes).

10.4 Conclusion

The results shown in Sec. 10.3.1 and 10.3.2 allow concluding that the proposed computerized system can be reliably used to quantitatively assess the vascular parameters in retinal images from normal, hypertensive or diabetic subjects. It will allow clinicians to recover the quantitative estimation of these parameters in an objective, fast and user-friendly way.

The first, totally automated phase performs image luminosity equalization and contrast enhancement, tracing of the vascular network with vessel caliber estimation, vessel classification as either arteries or veins. In the second phase, the user evaluates the results provided and confirms them or applies the necessary corrections via a user-friendly editing interface, which is capable of detecting the problems to be presented to the user for expert assistance. The vascular parameters are eventually computed. Accuracy and repeatability of the complete system were assessed by analyze the images kindly provided by the Dept. of Ophthalmology and Visual Sciences, University of Wisconsin, USA.

Chapter 11

Conclusions

11.1 Achievement of the Objectives

The aims of the work presented in this thesis were to develop an experimental prototype of adaptive optics (AO) fundus camera and a set of tools for the automatic analysis of the retinal vessel network.

As the AO fundus camera is concerned, our goal was to realize an instrument in which the w-f first order aberrations are estimated by a software code that analyzes the image produced by an *ad hoc* point-like source. The information obtained by this software then was given as an input to a deformable mirror that can change its shape in order to reduce the aberrations. The advantage of such an instrument if compared to a classical AO system is that the w-f sensor is no longer be necessary; this can reduce the cost of the instrument, and would avoid the many problems related to the maintenance of the performance of such a device once installed and aligned.

While the first part of this thesis concentrated on the abovementioned hardware issues, the second part dealt with the identification of the retinal vessel network, and with its description in terms of position, diameters, tortuosity, and indexes of clinical interest. The approach proposed in this thesis consisted in a sequence of independent modules, each of them with a different purpose. This approach may lack the global perspective that a human grader has in evaluating the state of a retina, but it is useful in breaking down a very hard problem into simpler ones that are computationally tractable. Although the extracted morphology of the vessel network would be a preliminary point to be considered for the recognition of the optic disc and for the elimination of the vascular structures in search of possible non-vascular lesions, in this thesis we had not address these subjects. Instead, we concentrated on the exploitation of the geometric characterization of the vascular network in order to estimate tortuosity, CRAE, CRVE, and AVR indexes as parameters of clinical relevance for the diagnosis of retinal pathologies.

The achievements obtained will be summarized in the following sections.

11.1.1 AO Fundus Camera Prototyping

The concept at the basis of the acquisition instrument developed in our laboratories consists in introducing, along the optical path of a fundus camera, a Deformable Mirror (DM) adaptive optics. The main problem of the conventional fundus camera is that the information through which the DM shape is adapted is provided by a complex and expensive wave-front (w-f) analyzer. The proposed solution consisted in projecting a known pattern on the retinal fundus, acquiring the resulting image with a dedicated sensor. Through a real-time analysis of the obtained image with the custom algorithms described in Chapter 4, it has been possible to obtain information about how the DM has to be appropriately deformed in order to reduce the aberration introduced by the eye.

In Chapter 4, it has been demonstrated, although in a simulated system, the feasibility of estimating and correcting an aberrated w-f shape by means of an iterative gradient-descent-like software procedure, acting on the point source image, without expensive w-f sensor. A hierarchy in the aberrations has been introduced, in order to reduce the dimensionality of the state space to be searched. The proposed algorithm was tested on a simple optical system that has been simulated with ray-tracing software, with randomly generated aberrations.

In Chapter 5 we described how we built in our laboratories the prototype of AO fundus camera, composed by the integration of the illumination system, the imaging system, and the system of projection of the reference pattern for the aberration estimation. The framework of the system was inspired by the commercial fundus camera MP-1 Nidek Technologies®, which we regarded as main reference model. Although the tests carried out with the sole deformable mirror (DM) have shown that the system reaches an optimal focusing condition in a few seconds, the acquisition of artificial retinal fundi has shown poor performance. In order to overcome the problem of the poor S/N ratio of the acquired target image, a variety of modifications have been introduced in the optical path, none of which, however, has led to comforting results. The incapability of the system to deal with the low physiologic reflectance of the human retina (4%), together with the intrinsic loss of intensity due to its peculiar optical path, discourage the usability of the system for clinical purposes. The most promising improvement to be taken into consideration will consist in redesigning the optical path for the near infrared spectrum.

11.1.2 Retinal Vessel Network Extraction

Most of the early symptoms indicating the onset of retinopathies are related to morphological features of the retinal vascular tree. In order to detect and quantita-

tively describe these diagnostic signs, the layout and the dimension of all the relevant vessels contained in the image has to be extracted.

The rationale of our method was to consider the image as a weighted un-oriented sparse graph where each node represents a pixel. The graph edges describe the 8-adjacency among pixels in the image. Under the assumption that vessels are minimum cost paths connecting remote nodes, we employed a graph search approach in order to identify their axes (Chapter 7). Then the vessel diameters are extracted by means of an efficient mono-dimensional matched filtering approach. The orientation of the filter kernel is chosen according to the information provided by the axis and the appropriate scale is computed by means of an initial diameter estimation performed on the vessels cross section profiles before the filtering process (Chapter 8).

Many automatic techniques for vessel identification have been proposed in the literature, with various degrees of complexity and accuracy (Sec. 7.1). The motivations that lead to the development of a new method can be summarized in three points: computational speed, robustness against non-connected vessels, flexibility to accommodate different magnification and resolution of retinal images.

These points were solved by using a tracking technique, which analyzes portion of images only in the surrounding of already identified vessel points. This approach allowed the evaluation of a small fraction of all image pixels. The tracking of non-connected vessels, due to presence of retinal lesions or to focal decrease in image contrast, requires the tracking procedure to start from different points along a vessel. This is achieved by using a sparse approach, in which a set of widespread starting points (seeds) within an image is identified. These seeds provide the mean to track every vessel even if not connected from the vessel tree, with reasonable chance. The vessel caliber extraction provided by the matched filters and fuzzy c-means clustering approach solves the problem of identifying contrast variation along a vessel, and of tuning the algorithm parameters for different image sources. Appropriate kernel orientation and scale are preventively evaluated, in order to improve the filter precision and efficiency. Then, an adaptive correction step allows managing critical situations (presence of noise, lack of contrast, *etc...*) in which the algorithm would fail to detect the correct diameters.

11.1.3 Tools for Clinical Use

With sustained hypertension, vessel walls are damaged and the morphology of the vascular tree changes as a consequence of the increased hydrostatic pressure. This damage and changes, lead to the appearance of specific signs as generalized narrowing and vessel tortuosity. These signs usually appear long before any malignant hypertensive retinopathy, and therefore all these vascular changes have to be identified and evaluated, in order to provide a sensible and robust diagnostic and prognostic tool to evaluate the retinopathy.

In Chapter 9, we defined the main factors that influence the classification of a vascular structure as tortuous or non-tortuous. This is most peculiar in analyzing retinal images, in which not only straight vessels but also long vessels presenting a smooth semi-circular shape are considered as non-tortuous. Then we focused on a formulation of *global tortuosity* that, starting from the measures of the single vessels, assesses the condition of the whole vessel network in a way that matches the clinician's grading.

In Chapter 10, we described a computerized system to quantitatively assess the CRAE, CRVE and AVR parameters in retinal images from normal, hypertensive or diabetic subjects. Its purpose is to allow clinicians to recover the quantitative estimation of these parameters in an objective, fast and user-friendly way. The first phase performs the vascular network segmentation by means of the algorithm proposed in Chapters 7 and 8, coupled with an artery/vein classifier. In the second phase, the user evaluates the results provided and confirms them or applies the needed corrections via a user-friendly editing interface, which is capable of detecting the troubled situations to be presented to the user for expert assistance. The vascular parameters are finally computed. Repeatability and accuracy of the complete system were assessed by having three users independently analyze retinal images from the database provided by the University of Wisconsin, whose analysis results were used as reference for accuracy. The overall repeatability between users and accuracy with respect to reference results were assessed by the correlation coefficients.

11.2 Final Summary

Although the simulation tests on the optic bench have provided encouraging preliminary results, the development of an AO fundus camera suitable for a clinic/diagnostic employment has encountered technical limitations, mostly regarding the prototyping of the instrument in an unproofed environment. Indeed, the spurious reflexes introduced in the optical system by the environment excessively reduce the signal-to-noise ratio – a problem which will have to be further investigated in the future.

A number of retinal fundus images, collected by gathering datasets built by us and datasets already used by other teams for research purposes, have been analyzed with custom algorithms able to extract important clinical parameters for the diagnosis of retinopathies. This thesis concentrated on the extraction and the analysis of the features of the vascular apparatus: the vessel network identification (veins and arteries) will allow the assessment of its main geometrical characteristics (length, direction, caliber, bifurcation, etc.). From these findings, specific indexes of diagnostic relevance have been computed, providing the clinicians with information regarding the patient's retinopathy degree, whose significance is crucial for the diagnosis of retinal pathologies.

The proposed software for the identification of retinal vascular structures is currently the object of clinical evaluation at the Department of Ophthalmology and Visual Sciences, University of Wisconsin, USA, whose Fundus Photograph Reading Center has declared its will to adopt the proposed system as the standard for the determination of diagnostic features.

The recent collaboration with the Department of Twin Research & Genetic Epidemiology, of the King's College London Division of Genetics and Molecular Medicine, St Thomas' Hospital, UK, has brought to the agreement that more than 3,500 retinal fundus images (plus 10 new images per week) will be provided by the Department, being consequently processed and analyzed with our software for the estimation of the clinical indexes.

The results achieved both in the experimentations and thanks to the fruitful international collaboration established with relevant clinical and research groups make us quite confident as regards the quality of the developed methodologies and the potential success of their employment, with the auspice that future improvements can broaden their usability.

References

[1] J. A. Pugh, J. M. Jacobson, W. A. J. Van Heuven, J. A. Watters, M. R. Tuley, D. R. Lairson, R. J. Lorimor, A. S. Kapadia, and R. Velez, Screening for diabetic retinopathy. the wide angle retinal camera, Diabetes Care 16 (1993), no. 6, 889-895.

[2] D. J. Taylor, J. Fisher, J. Jacob, and J. E. Tooke, The use of digital cameras in a mobile retinal screening environment., Diabetic Medicine 16 (1999), 680-686.

[3] H. M. Herbert, K. Jordan, and D. W. Flanagan, Is screening with digital imaging using one retinal view adquate?, Eye 17 (2003), no. 3, 497-500.

[4] L. Varma, G. Prakash, and H. K. Tewari, Diabetic retinopathy: time for action. no complacency, please!, Bullettin of the World Health Organization 80 (2002), 419.

[5] C. D. Murray, The physiological principle of minimum work. i. the vascular system and the cost of blood volume., Proceedings of the National Academy of Science 12 (1926), 207-214.

[6] A. V. Stanton, B. Wasan, A. Cerutti, S. Ford, R. Marsh, P. P. Sever, S. A. Thom, and A. D. Hughes, Vascular network changes in the retina with age and hypertension, Journal of Hypertension 13 (1995), 1724-1728.

[7] Early Treatement Diabetic Retinopathy Study Research Group, Grading diabetic retinopathy from stereoscopic fundus photographs - am extension of the modified airlie house classification. Ophthalmology 98 (1991), 786-806.

[8] N. M Keith, H. P. Wegener, and N. W. Barker, Some different types of essential hypertension: their course and prognosis, American Journal of Medicine Science 197 (1939), 336-354.

[9] H. G. Scheie, Evaluation of ophthalmoscopic changes of hypertension and arterial sclerosis, Archives of Ophthalmology 49 (1953), no. 2, 117-138.

[10] S. Chatterjee, S. Chattopahya, M. Hope-Ross, and P. L. Lip, Hypertensionand the eye: changing perspectives, Journal of Human Hypertension 16 (2002), 667-675.

[11] The Diabetic Retinopathy Study Research Group, A modification of the airlie house classification of diabetic retinopathy, Investigative Ophthalmology and Visual Science 21 (1981), 210-226.

[12] Early Treatment Diabetic Retinopathy Study Research Group, Early treatment diabetic retinopathy study design and baseline patient characteristics, Ophthalmology 98 (1991), 741-756.

[13] C. P. Wilkinosn, F. L. Ferries, R. E. Klein, P. P. Lee, C. D. Agardh, M. Davies, D. Dills, A. Kampik, R. Pararajasegaram, and J. T. Vardaguer representing the global Diabetic Retinopathy Project Group, Proposed international clinical diabetic retinopathy and diabetic macular edema disease severity scale, Ophthalmolgy 110 (2003), 1677-1612.

[14] S. J. Aldington, E. M. Kohner, S. Meuer, R. Klein, A. K. Sjolie, and Complication Study Group EURODIAB IDDM, Methodology for retinal photography of diabetic retinopathy: the EURODIAB IDDM Study Group, Diabetologia 38 (1995), no. 4, 437-444.

[15] S. Bursell, J. D. Cavallerano, A. A. Cavallerano, A. C. Clermont, D. Birkmire-Peters, L. P. Aiello, L. M. Aiello, and the Joslin Vision Network Research Team, Stereo nonmydriatic digital-video color retinal imaging compared with early treatement diabetic retinopathy study seven standard field 35-mm stereo color for determining level of diabetic retinopathy, Ophthalmology 108 (2001), no. 3, 572-585.

[16] D. Y. Lin, M. S. Blumenkranz, R. J. Brothers, D. M. Grosvenor, and for the digital diabetic screening group, The sensitivity and specificity of single-field nonmydriatic monochromatic digital fundus photography with remote image interpretation dor diabetic retinopathy screening: a comparison with ophthalmoscopy and standardized mydriatic color photography, American Journal of Ophthalmology (2002), 204-213.

[17] P. Massin, A. Erginay, A. Ben Mehdi, E. Vicaut, G. Quentel, Z. Victor, M. Marret, P. J. Guillausseau, and A. Gaudric, Evaluation of a new non-mydriatic digital camera for detection of diabetic retinopathy, Diabetic Medicine 20 (2003), 635-641.

[18] ARIC, ARIC protocol 14A retinal photography, ARIC Coordinating Center, Department of Biostatistics (CSCC), University of North Carolina, August 1995.

[19] ARIC, ARIC protocol 14B retinal reading protocol, ARIC Coordinating Center, Department of Biostatistics (CSCC), University of North Carolina, May 1996.

[20] G. A. Williams, I. U. Scott, J. A. Haller, A. M. Maguire, D. Marcus, and H.R. McDonald, Single-field fundus photography for diabetic retinopathy screening, Ophthalmology 111 (2004), no. 5, 1055-1012.

[21] M. Glanc, E. Gendron, F. Lacombe, D. Lafaille, J. F. Le Gargasson, and P. Léna, "Towards wide-field retinal imaging with adaptive optics," Opt. Commun. 230, 225–238 (2004).

[22] N. Doble and D. R. Williams, "The application of MEMS technology for adaptive optics in vision science," IEEE J. Sel. Top. Quantum Electron. 10, 629–635 (2004).

[23] W. Quan, Z.-Q. Wang, G.-G. Mu, and L. Ning, "Correction of the aberrations in the human eyes with svag1 thin-film transistor liquid-crystal display," Optik 114, 467–471 (2003).

[24] J.-F. Le Gargasson, M. Glanc, and P. Léna, "Retinal imaging with adaptive optics," C. R. Acad. Sci., Ser IV Phys. Astrophys. 2, 1131–1138 (2001).

[25] F. Fankhauser, P. F. Niederer, S. Kwasniewska, and F. van der Zypen, "Supernormal vision, high-resolution retinal imaging, multiphoton imaging and nanosurgery of the cornea-a review," Technol. Health Care 12, 443–453 (2004).

[26] E. J. Fernández and L. Vabre, "Adaptive optics with a magnetic deformable mirror: application in the human eye," Opt. Express 14, 8900–8917 (2006).

[27] J. Liang, B. Grimm, S. Goelz, and J. F. Bille, "Objective measurement of wave aberrations of the human eye with the use of a Hartmann–Shack wave-front sensor," J. Opt. Soc. Am. A 11, 1949–1957 (1994).

[28] J. C. He, S. Marcos, R. H. Webb, and S. A. Burns, "Measurement of the wavefont aberration of the eye by a fast psychophysical procedure," J. Opt. Soc. Am. A 15, 1–8 (1998).

[29] M. A. Losada and R. Navarro, "Point spread function of the human eye obtained by a dual double-pass method," Pure Appl. Opt. 7, L7–L13 (1998).

[30] M. J. Booth, "Wavefront sensorless adaptive optics: a model based approach using sphere packings," Opt. Express 14, 1339–1352 (2006).

[31] M. J. Booth, "Wavefront sensorless adaptive optics for large aberrations," Opt. Lett. 32, 5–7 (2007).

[32] S. Zommer, E. N. Ribak, S. G. Lipson, and J. Adler, "Simulated annealing in ocular adaptive optics," Opt. Lett. 31, 1–3 (2006).

[33] L. Murray, J. C. Dainty, and E. Daly, "Wavefront correction through image sharpness maximisation," Proc. SPIE 5823, 40–47 (2005).

[34] J. R. Fienup and J. J. Miller, "Aberration correction by maximizing generalized sharpness metrics," J. Opt. Soc. Am. A 20, 609–620 (2003).

[35] R. A. Muller and A. Buffington, "Real-time correction of atmospherically degraded telescope images through image sharpening," J. Opt. Soc. Am. 64, 1200–1210 (1974).

[36] M. A. Vorontsov, G. W. Carhart, D. V. Pruidze, J. C. Ricklin, and D. G. Voelz, "Image quality criteria for an adaptive imaging system based on statistical analysis of the speckle field," J. Opt. Soc. Am. A 13, 1456–1466 (1996).

[37] J. Wang and D. Silva, "Wave-front interpretation with Zernike polynomials," Appl. Opt. 19, 1510–1518 (1980).

[38] J. Hardy, Adaptive Optics for Astronomical Telescopes (Oxford University Press, 1998).

[39] R. Irwan and R. Lane, "Analysis of optimal centroid estimation applied to Shack–Hartmann sensing," Appl. Opt. 38, 6737– 6743 (1999).

[40] R. K. Tyson, D. E. Canning, and J. S. Tharp, "Measurement of the bit-error rate of an adaptive optics, free-space laser communications system, part 1: tip-tilt configuration, diagnostics, and closed-loop results," Opt. Eng. 44, 096002 (2005).

[41] R. K. Tyson, J. S. Tharp, and D. E. Canning, "Measurement of the bit-error rate of an adaptive optics, free-space laser communications system, part 2: multichannel configuration, aberration characterization, and closed-loop results," Opt. Eng. 44, 096003 (2005).

[42] O. Albert, L. Sherman, G. Mourou, and T. Norris, "Smart microscope: an adaptive optics learning system for aberration correction in multiphoton confocal microscopy," Opt. Lett. 25, 52–54 (2000).

[43] B. Potsaid, Y. Bellouard, and J. Wen, "Adaptive scanning optical microscope (ASOM): A multidisciplinary optical microscope design for large field of view and high resolution imaging," Opt. Express 13, 6504–6518 (2005).

[44] J. Liang and D. Williams, "Aberrations and retinal image quality of the normal human eye," J. Opt. Soc. Am. A 14, 2873–2883 (1997).

[45] D. Iskander, M. Collins, M. Morelande, and M. Zhu, "Analyzing the dynamic wavefront aberrations in the human eye," IEEE Trans. Biomed. Eng. 51, 1969–1980 (2004).

[46] L. Zhu, M. Collins, and D. Iskander, "Microfluctuations of wavefront aberrations of the eye," Ophthalmic Physiol. Opt. 24, 562–671 (2004).

[47] T. Okada, K. Ebata, M. Shiozaki, T. Kyotani, A. Tsuboi, M. Sawada, and H. Fukushima, "Development of adaptive mirror for CO_2 laser," in High-Power Lasers in Manufacturing, X. Chen, T. Fujioka, and A. Matsunawa, eds., Proc. SPIE 3888, 509–520 (2000).

[48] S. Jackel and I. Moshe, "Adaptive compensation of lower order thermal aberrations in concave-convex power oscillators under variable pump conditions," Opt. Eng. 39, 2330–2337 (2000).

[49] P. Villoresi, S. Bonora, M. Pascolini, L. Poletto, G. Tondello, C. Vozzi, M. Nisoli, G. Sansone, S. Stagira, and S. D. Silvestri, "Optimization of high-order harmonic generation by adaptive control of a sub-10-fs pulse wave front," Opt. Lett. 29, 207–209 (2004).

[50] R. Zacharias, N. Beer, E. Bliss, S. Burkhart, S. Cohen, S. Sutton, R. V. Atta, S. Winters, J. T. Salmon, M. L. C. Stolz, D. Pigg, and T. Arnold, "Alignment and wavefront control systems of the National Ignition Facility," Opt. Eng. 43, 2873–2884 (2004).

[51] W. Shakespeare, R. Pearson, J. Grenestedt, P. Hutapea, and V. Gupta, "MEMS integrated submount alignment for optoelectronics," J. Lightwave Technol. 23, 504 (2005).

[52] F. Gonté, A. Courteville, and R. Dändliker, "Optimization of single-mode fiber coupling efficiency with an adaptive membrane mirror," Opt. Eng. 41, 10731076 (2002).

[53] S. Bonora, I. Capraro, L. Poletto, M. Romanin, C. Trestino, and P. Villoresi, "Fast wavefront active control by a DSP-driven deformable membrane mirror," Rev. Sci. Instrum. 77, 093,102 (2006).

[54] S. Bonora and L. Poletto, "Push-pull membrane mirrors for adaptive optics," Opt. Express 14, 11,935–11,944 (2006). 28. R. Noll, "Zernike polynomials and atmospheric turbulence," J. Opt. Soc. Am. 66, 207–211 (1976).

[55] E. Clafin and N. Bareket, "Configuring an electrostatic membrane mirror by least-squares fitting with analytically derived influence functions," J. Opt. Soc. Am. 3, 1833–1839 (1986).

[56] G. Vdovin, "Spatial light modulator based on the control of the wavefront curvature," Opt. Commun. 115, 170–178 (1995).

[57] L. Zhu, P. Sun, D. Bartsch, W. Freeman, and Y. Fainman, "Wave-front generation of Zernike polynomial modes with a micromachined membrane deformable mirror," Appl. Opt. 38, 6019–6026 (1999).

[58] J.J. Staal, M.D. Abramoff, M. Niemeijer, M.A. Viergever, B. van Ginneken, "Ridge based vessel segmentation in color images of the retina", IEEE Transactions on Medical Imaging, 2004, vol. 23, pp. 501-509.

[59] M. Niemeijer, J.J. Staal, B. van Ginneken, M. Loog, M.D. Abramoff, "Comparative study of retinal vessel segmentation methods on a new publicly available database", in: SPIE Medical Imaging, Editor(s): J. Michael Fitzpatrick, M. Sonka, SPIE, 2004, vol. 5370, pp. 648-656.

[60] Hoover A, Kouznetsova V, Goldbaum MH, Locating Blood Vessels in Retinal Images by Piece-wise Threhsold Probing of a Matched Filter Response, IEEE Transactions on Medical Imaging, vol. 19 no. 3, pp. 203-210, March 2000

[61] The DCCT Group (1987), Color photography vs. fluorescein angiography in the detection of diabetic retinopathy in the Diabetes Control and Complications Trial, Arch Ophthalmol. 105: 1344-51.

[62] Early Treatment Diabetic Retinopathy Study Research Group (1991), Grading diabetic retinopathy from stereoscopic fundus photographs- an extension of the modified Airlie House classification, Ophthalmology 98: 786-806.

[63] L. Tramontan, A. Ruggeri, “Computer Estimation of the AVR Parameter in Diabetic Retinopathy” IFMBE Proceedings WC 2009 “World Congress on Medical Physics and Biomedical Engineering”, Vol. 25, 2009, Munich, Germany

[64] L. D. Hubbard, R. J. Brothers, W. N. King, L. X. Clegg, R. Klein, L. S. Cooper, A. R. Sharrett, M. D. Davis, and J. Cai, Methods for evaluation of retinal microvascular abnormalities associated with hypertension/sclerosis in the atherosclerosis risk in communities study, Ophthalmology 106 (1999), no. 12, 2269-2280.

[65] M. Sonka, M. D. Winniford, and S. M. Collins, Robust simultaneous detection of coronary borders in complex images, IEEE Transactions on Medical Imaging 14 (1995), no. 1, 151-161.

[66] P. H. Eichel, E. J. Delp, K. Koral, and A. J. Buda, A method for a fully automatic definition of coronary arterial edges from cineangiograms, IEEE Transactions on Medical Imaging 7 (1998), no. 4, 313-320.

[67] E. Grisan, M. Foracchia, and A. Ruggeri, (2003) Normalization of luminance and contrast in fundus images. Medical Image Analysis 2: 179-190

[68] T. N. Pappas and J. S. Lim, A new method for estimation of coronary artery dimensions in angiograms, IEEE Transactions on Acoustics, Speech, and Signal Processing 36 (1988), no. 9, 1501-1513.

[69] I. Liu and Y. Sun, Recursive tracking of vascular networks in angiograms based on the detection-deletion scheme, IEEE Transactions on Medical Imaging 12 (1993), no. 2, 334-341.

[70] F. P. Miles and A. L. Nuttall, Matched filter estimation of serial blood vessel diameters from video images, IEEE Transactions on Medical Imaging 12 (1993), no. 2, 147-152.

[71] M. A. T. Figueiredo and J. M. N. Leitao, A non smoothing approach to the estimation of vessel contours in angiograms, IEEE Transactions on Medical Imaging 14 (1995), no. 1, 162-172.

[72] Y. Sun, Automated identification of vessel contours in coronary arteriograms by an adaptive tracking algorithm, IEEE Transactions on Medical Imaging 8 (1989), no. 1, 78-88.

[73] S. R. Fleagle, M. R. Johnson, C. J. Wilbricht, D. J. Skorton, R. F. Wilson, C. W. White, M. L. Marcus, and S. M. Collins, Automated analysis of coronary arterial morphology in cineangiograms: Geometric and physiologic validation in humans, IEEE Transactions on Medical Imaging 8 (1989), no. 4, 387-400.

[74] M. Sonka, C. J. Wilbricht, S. R. Fleagle, S. K. Tadikonda, M. Winniford, and S. M. Collins, Simultaneous detection of both coronary borders, IEEE Transactions on Medical Imaging 12 (1993), no. 3, 588-599.

[75] Y. Sun, R. J. Lucariello, and S. A. Chiaramida, Directional low-pass filtering for improved accuracy and reproducibility of stenosis quantification in coronary arteriograms, IEEE Transactions on Medical Imaging 14 (1995), no. 2, 242-248.

[76] K. V. Chandrinos, M. Pilu, R. B. Fisher, and P.E. Trahanias, Image processing techniques for the quantification of atherosclerotic changes, Proceedings MEDICO98 (Limassol, Cyprus), June 1998.

[77] A. Sen, L. Lan, K. Doi, and K. R. Hoffmann, Quantitative evaluation of vessel tracking techniques on coronary angiograms, Medical Physics 26 (1999), no. 5, 698-706.

[78] S. Chaudhuri, S. Chatterjee, N. Katz, M. Nelson, and M. Goldbaum, Detection of blood vessels in retinal images using two-dimensional matched filters, IEEE Transactions on Medical Imaging 8 (1989), no. 3, 263-269.

[79] L. Zhou, S. Rzeszotarski, L. J. Singermann, and J. Chokreff, The detection and quantification of retinopathy using digital angiograms, IEEE Transactions on Medical Imaging 13 (1994), no. 4, 619-626.

[80] Y. A. Tolias and S. M. Panas, A fuzzy vessel tracking algorithm for retinal images based on fuzzy clustering, IEEE Transactions on Medical Imaging 17 (1998), no. 2, 263-273.

[81] A. Can, H. Shen, J. N. Turner, H. L. Tanenbaum, and B. Roysam, Rapid automated tracing and feature extraction from retinal fundus images using direct exploratory algorithms, IEEE Transactions on Information Technology in Biomedicine 3 (1999), no. 2, 125-138.

[82] J.-H. Yu, B.-N. Hung, and H.-C. Sun, Automatic recognition of retiopathy from retinal images, Proceedings of the annual international conference IEEE/EMBS 1990, IEEE, 1990, pp. 171-173.

[83] Y. Wang and S. C. Lee, A fast method for automated detection of blood vessels in retinal images, Proceedings of the 31st Asilomar Conference on Signal, System, and Computers, 1997.

[84] M. E. Martinez-Perez, A. D. Hughes, A. V. Stanton, S. A. Thom, A. A. Bharath, and K. H. Parker, Scale-space analysis for the characterization of retinal blood vessels, MIUA99 On-line proceedings (http://www-ipg.umds.ac.uk/miua/proceedings/IE index.html), Medical Image Understanding and Analysis, July 1999.

[85] M. Goldbaum, N. Katz, S. Chatterjee, and M. Nelson, "Image understanding for automated retinal diagnoses", IEEE Symposium for computer applications in clinical medicine, 1989, pp. 756-760.

[86] T. Chanwimaluang and G. Fan, "An efficient algorithm for extraction of anatomical structures in retinal images", Proceedings of the IEEE International Conference on Image Processing (Barcelona, (ES)), September 2003.

[87] Patton N, Aslam TM, Macgillivray T, Deary IJ, Dhillon B, Eikelboom RH, et al. "Retinal image analysis: concepts, applications and potential". Prog Retin Eye Res 2006; 25:99–127.

[88] C. Heneghan, J. Flynn, M. O'Keefe, and M. Cahill, Characterization of changes in blood vessel width and tortuosity in retinopathy of prematurity using image analysis, Medical image analysis 6 (2002), 407-429.

[89] Kochner B, Schuhmann D, Michaelis M, Mann G, Englmeier K-H. "Course tracking and contour extraction of retinal vessels from color fundus photographs: most efficient use of steerable filters for model based image analysis". In: SPIE conference image processing, vol. 3338. 1998. p. 755–61.

[90] Lowell J, Hunter A, Steel D, Basu A, Ryder R, Kennedy RL. Measurement of retinal vessel widths from fundus images based on 2-D Modeling. IEEE Trans Med Imaging 2004;23:1196–204.

[91] Yang C-W, Ma D-J, Chao S-C, Wang C-M, Wen CH, Lo SC, et al. A compute-raided diagnostic detection system of venous beading in retinal images. Opt Eng 2000;39:1293–303.

[92] Zana F, Klein J. A multimodal registration algorithm of eye fundus images using vessels detection and Hough transform. IEEE Trans Med Imaging 1999;18:419–28.

[93] Gregson P, Shen Z, Scott R, Kozousek V. Automated grading of venous beading. Comput Biomed Res 1995;28:291–304.

[94] Mendonca, A.M. and Campilho, A.: Segmentation of retinal blood vessels by combining the detection of centerlines and morphological reconstruction. IEEE Trans. Med. Imaging 25(9): 1200-1213 (2006)

[95] Akita K, Kuga H. A computer method of understanding ocular fundus images. Pattern Recognit 1982;15:431–43.

[96] G. Gardner, D. Keating, T. Williamson, and A. Elliot, "Automatic detection of diabetic retinopathy using an artificial neural network: a screening tool", British Journal of Ophthalmology 80 (1996), 940-944.

[97] C. Sinthanayothin, Sinthanayothin C, Boyce JF, Cook HL, Williamson TH. Automated localization of the optic disc, fovea, and retinal blood vessels from digital color fundus images. Br J Ophthalmol 1999; 83:902–10.

[98] J. V. B. Soares, J. J. G. Leandro, R. M. Cesar Jr., H. F. Jelinek and M. J. Cree "Retinal vessel segmentation using the 2D Gabor wavelet and supervised classification", *IEEE Trans. Med. Imag.*, vol. 25, pp. 1214-1222, Sep. 2006.

[99] Ricci, E. and Perfetti, R., Retinal blood vessel segmentation using line operators and support vector classification. IEEE Trans. Med. Imag. v26. 1357-1365.

[100] E.W. Dijkstra. A note on two problems in connection with graphs. Numerische Mathematik, 1:269--271, 1959.

[101] L. Sint and D. de Champeaux. An Improved Bidirectional Heuristic Search Algorithm. J. ACM 24, 2 (Apr. 1977), pp 177-191.

[102] C. Sun and S. Pallottino. "Circular shortest path in images" Pattern Recognition, vol. 36, no. 3, pp. 711--721, March 2003.

[103] S. M. Kay, (1998) Fundamentals of Statistical Signal Processing. New Jersey: Prentice-Hall

[104] M. Sofka and C. V. Stewart, (2006) Retinal vessel centerline extraction using multiscale matched filters, confidence and edge measures. IEEE TMI 25: 1531-1546

[105] M. Jacob and M. Unser, (2004) Design of steerable filters for feature detection using canny-like criteria. IEEE Trans. on Pattern Analysis and Machine Intelligence 26(8):1007-1019

[106] A. Frangi et al., (1995) Multiscale vessel enhacement filtering. Medical Image Computing and Computer-Assisted Intervention 1496: 130-137

[107] C. Tomasi and R. Manduchi, (1998) Bilateral Filtering for Gray and Color Images. Proceedings of the Sixth International Conference on Computer Vision 839-846

[108] J. C. Dunn (1973): "A Fuzzy Relative of the ISODATA Process and Its Use in Detecting Compact Well-Separated Clusters", Journal of Cybernetics 3(3): 32-57

[109] E. Grisan, M. Foracchia, A. Ruggeri, "A novel method for the automatic grading of retinal vessel tortuosity", IEEE Transactions on Medical Imaging, 2008, 27(3), 310-319

[110] W. E. Hart, M. Goldbaum, B. Côté, P. Kube, and M. R. Nelson, Measurement and classification of retinal vascular tortuosity, International Journal of Medical Informatics 53 (1999), no. 2-3, 239-252.

[111] M. E. Martinez-Perez, A. D. Hughes, A. V. Stanton, S. A. Thom, A. A. Bharath, and K. H. Parker, Retinal vascular tree morphology: a semi automatic quantification, IEEE Transactions on Biomedical Engineering 49 (2002), no. 8, 912-917.

[112] Wong T.Y., Knudtson M., Klein R., Klein B.E.K., Meuer S.M., Hubbard L.D. (2004), Computer-assisted measurement of retinal vessel diameters in the Beaver Dam eye study, Ophthalmology, vol. 111: 1183–90.

[113] Li H., Hsu W., Lee M.L., Wong T.Y. (2005), Automatic grading of retinal vessel caliber, IEEE Trans Biomed Eng, vol. 52: 1352-5

[114] Knudtson M.D., Lee K.E., Hubbard L.H., Wong T.Y., Klein R., Klein B.E.K. (2003), Revised formulas for summarizing retinal vessel diameters, Current Eye Research, vol. 27, no. 3: 143-149.